Photonic modes of organic light emitting structures

Submitted by

Peter Allen Hobson

to the University of Exeter
as a thesis for the degree
of Doctor of Philosophy
in Physics

July 2002

Abstract

Organic light emitting diodes (OLEDs) consist of an optical microcavity containing an organic semiconductor in which one bounding layer is a metallic cathode. To achieve high efficiency OLEDs a primary issue to address is how the light resulting from the decay of excitons within the device may be extracted as useful radiation. More than 50% of the light produced by exciton decay never leaves the device, being trapped in the form of waveguide modes and ultimately lost to absorption. Less understood is the loss of efficiency that arises due to quenching of excitons by excitation surface plasmon polariton (SPP) modes associated with the metallic cathode. We comprehensively evaluate the extent to which the generation of SPPs limit device efficiency in small molecule based OLEDs. We show experimentally that through the use of appropriate periodic nanostructure, power lost to surface plasmon polariton modes can be recovered. Excellent agreement between experimental measurements and theoretical modelling allow us to estimate that out-coupling the SPP has doubled the efficiency of the device.

The optical microcavity also provides a convenient environment in which to investigate new physics in interactions between light and matter. We report the first experimental observation of strong exciton-photon coupling in a planar microcavity composed of an organic semiconductor positioned between two metallic (silver) mirrors. Via transmission and reflectivity measurements, we observe a very large, room temperature Rabi-splitting in excess of 300 meV between upper and lower cavity polariton branches. We show that the Rabi-splitting is enhanced in all-metal microcavities by a factor of more than 2 when compared to microcavities composed of an organic film having the same oscillator strength positioned between a silver mirror and a dielectric mirror.

List of Figures

plasmons.

Contents

Acknowledgements

As is the custom I would like to thank all those people without whose help, kindness, support, cajoling and threats I would not have finished my PhD. Firstly I'd like to thank my supervisor, Bill Barnes whose cheerfulness, insight and limitless enthusiasm has kept me on track. Secondly I'd like to thank Roy Sambles, again for limitless enthusiasm this time with insight delivered in his own direct Cornish style.

Thanks should be expressed to Ian Sage who helped fund this work (in association with the EPSRC) through a CASE award from QinetiQ, who also deposited countless films in my quest for a working OLED device. Further thanks should be expressed to David Lidzey from the University of Sheffield for all the work done on the strong coupling collaboration. Also, to Colin Cole of Avimo Thin Films, for ITO deposition.

I would like to thank my colleagues present and past from the basement and surrounding suburbs who have made Exeter such an entertaining and singular environment to work. Those who deserve special mention include Jon Wasey, who provided much of the theoretical modelling on OLEDs in chapter 5 seemingly without the need to get out of bed and come into work. Piers Andrew whose misfortune it was to share his office with me and to explain much of what I don't understand. Yes mate all the mess is mine. Other members of the old guard include MJ for the occasional nugget of physics and the far more regular film reviews. The V, for those encouraging pats during badminton. Al (on on stick) with his sense of humour straight out of a carry on film. Nobu, who has cheered up, now he can see the light at the end of the tunnel. Also, thanks to those fellow sufferers in my year, namely Ian (theory-boy) and Hazel (the best cook of a roast dinner in the Southwest). Sharon deserves a

mention just because she believes Henman can win the Wimbledon this year.

I should mention the now ex-TFP boys, Nate-Dog my fellow car mechanic. 'Slippy' Phil an entertaining travelling companion with the cross-stitch. Mart, for many crafty Jedi tricks. Also Benny, ditto the crafty tricks and funny quips.

Of the current crop, Steve deserves a mention for not being impressed by absolutely anything except dogs that is (no whiners). And the latest talent, Simon for being too earnest, "itsh da Carling mate". Andy, well he's got some balls. Jim for sardonic attacks on everyone and Matt who wants his cake and eat it……in Singapore. As for Simion, 5 min max at groups meetings please.

Of the non-TFP guys, I should thank some of med-phys, after all they did MRI scan my brain proving I have got one. A medal/ cross should go to Karen for being my longest suffering flat mate. Its alright for me…. Jules also needs a mention and probably a pint of wife beater. To ex-TFP scary Al, big brother is indeed watching you. Others worth a mention are Tony (enough of the old Rosie) and my old practical partner and drinking bud Norman.

Many thanks to Pete Cann, for cheesecake and making all those excellent sample mounts mirrors holders etc, I've used in last 4 years. For many excellent aluminium and gold films I thank Dave "Campari Kid" Jarvis. I would also like to thank the rest of the workshop crew for help down the years and also for being such amusing and civilised drinking companions. The real power in the department also needs to be thanked and acknowledged namely the ladies on the 6th floor.

Finally and most importantly I'd like to thank Mum and Dad for their constant support and encouragement, and my brother Mike for his cheek. It's finally finished.

Chapter 1

Introduction

This thesis brings together recent experiments concerning the interaction of light with organic photonic materials. Typically this interaction falls within two regimes known as weak and strong coupling. In weak coupling an excited species looses a quanta of energy to one of the photonic modes of the device. The presence of the emitter does not alter the photonic modes of the structure. By contrast, in strong coupling the presence of the emitter does alter the photonic modes. The signature of strong coupling is an anti-crossing of the exciton and photon modes resulting in new, hybrid excitonic-photonic modes. Both interactions are experimentally investigated in chapters of this thesis. The other chapters introduce the salient points of the underlying physics through discussion of the optical physics of multilayer structures (waveguides), the optical and dielectric properties of photonic materials and excitonic effects with reference to recent experimental research and current applications.

The light emitting diode (LED) structure represents a convenient system for the investigation of both forms of light-matter interaction and in this respect the organic LED (OLED) was a more accessible structure to fabricate in our laboratory than the inorganic LED. It is only recently that organic devices have been seen as viable candidates for display and communication applications. Electroluminescence from single organic crystals was first observed from anthracene in 1963 [*Helfrich and Schneider* (1965)]. However as the efficiency of organic devices was less than that of inorganic devices, research activities were focused on inorganic systems. In the 1980s the field of organic electroluminescence underwent a revival when *Tang and VanSlyke* (1987) began developing a new generation of OLEDs based on amorphous films of small molecules. Another watershed in the evolution of the OLED was the work by *Burroughes*

et al. (1990), achieving major technological advances by developing an easily processable single layer OLED based upon light emitting conjugated polymers.

In an attempt to improve the optical output of LEDs, resonant cavities were introduced, including metal clad microcavities. As opposed to the OLED, which normally has one semitransparent dielectric anode and one metallic cathode, this structure has two metal mirrors bounding the active material. The higher reflectivity of this structure means that the photon-material interaction is stronger. It is in such microcavity structures that strong coupling is investigated in this thesis.

The structure of this thesis is as follows. Chapter 2 introduces the photonic modes associated with planar waveguide structures. The conditions for coupling to leaky (radiative) and bound (non-radiative) modes including surface modes are identified. Methods for coupling light to and from guided modes (i.e. using texturing of the waveguide) are outlined, as is a theoretical model for calculating the reflectivity from a corrugated multilayer structure.

In chapter 3 we look at the fundamentals of weak and strong coupling. We begin initially with the weak regime by reviewing spontaneous emission (SpE) near interfaces. We lay out the basic concepts and outline an appropriate theoretical model. We finish by examining the decay routes open to an emitter located in a waveguide structure. Following this, a practical application of the planar cavity in the weak coupling regime is examined by considering OLED devices. We finish by examining strong coupling in atomic and semiconductor physics and the impact of organic photonic materials on this field.

In Chapter 4 we describe the experimental methods used for the fabrication of nano-textured OLEDs measured in chapter 5. Also discussed are the experimental techniques for making the planar metal-clad microcavities used to investigate strong coupling as detailed in chapter 6. Chapter 4 also contains descriptions of surface

profile analysis by atomic force microscopy and details of the operation and degradation routes of the OLED.

The work presented in chapter 5, reports on the first experimental demonstration of an OLED device that couples out light that would otherwise be lost to the surface plasmon polariton (SPP) mode as well as other guided modes. Also observed are enhancements to device emission and polarisation changes and spectral changes in the emission spectra. For electroluminescent emission in the forward direction we have a doubling of efficiency compared to the planar device and conclude that out coupled SPP modes are responsible for ~50% emission from the textured device. Through modelling of the planar OLEDs we are able calculate the extent to which radiative excitons couple to SPPs and other guided modes. Through modelling of the textured OLED we are also able to accurately map the dispersion of the modes in the corrugated system.

In chapter 6 we present the results of a study on strong coupling between organic aggregate excitons and a waveguide mode in a metal-mirrored microcavity. The key signature of strong coupling is an anti-crossing of the exciton and photon modes. Our measurements demonstrate the first observation of strong coupling in a metal-clad microcavity. Finally we examine possible future directions for work involving exciton-SPP interactions.

Chapter 7 summarises the work presented in the thesis and indicates possible directions for future research.

Chapter 2
Optical Modes of Waveguide Structures

2.1 Introduction

In the process of spontaneous emission (SpE) an excited species (atom or molecule) relaxes to a lower energy state via the emission of a photon. If emission takes place within free space there are no limitations on the nature of the emission. If emission takes place within some optical environment the emission is no longer unconstrained and is limited by the boundary conditions imposed by the structure. Hence, emission will couple to an optical mode of the structure. Further, if emission takes place close to a metal surface then the excitation of surface modes directly competes with the emission of photons. Before we consider the behaviour of emissive structures in the next chapter we need to look at the types of optical mode that are typically present in optical waveguide devices.

In this chapter we discuss a number of related topics, to establish the required conceptual framework. This principally involves the propagation of optical modes in metal/dielectric waveguide structures with dielectric thickness comparable to the wavelength of light. We will consider the waveguide and surface modes of three different structures in turn; single interface, metal/dielectric; double interface asymmetric, metal/high index dielectric/ low index dielectric and double interface symmetric consisting of metal /dielectric/ metal.

The dispersion relations for TE, TM and surface modes will be derived for the asymmetric and symmetric waveguide using appropriate boundary conditions and Maxwell's curl equations. The form of the electric field through the waveguide structures will be ascertained, as will mode cut-off conditions.

Mechanisms for coupling radiative light to and from the optical modes are discussed, along with theoretical treatment of multilayer periodic structures.

2.2 Surface-plasmon polaritons

All of the work in this thesis is concerned with the examination of optical modes in one form of microcavity or another, be they planar or corrugated, whether they contain metal mirrors or dielectric ones. For this reason it is necessary to develop an accurate physical model to explain the observed optical physics of such structures.

The surface plasmon polariton (SPP) is a bound, non-radiative, electromagnetic mode, which propagates along the interface of a metal and a dielectric. In short, the SPP arises due to coupling between electromagnetic radiation and surface charge oscillations. Such a circumstance occurs only when the electric field has a component perpendicular to the interface i.e. with transverse magnetic (TM) radiation (transverse electric radiation (TE) has its electric field component aligned parallel to an interface and consequently may not couple to the SPP mode). The resulting SPP has fields that are strongly localised at the interface of the media, with evanescent 'tails' decaying exponentially into the boundary media. Therefore, SPPs are strongly influenced by the properties of the interface region and have numerous applications in the study of dielectric over-layers [*Raether* (1998)], surface texture etc. The most prevalent use of SPPs is that of sensor applications. Examples include gases [*Nylander* et al. (1982)]. Also SPPs have been used to monitor electrochemical reactions, e.g. *Jory* et al. (1996).

The dispersion relation, $\omega(k)$, of the SPP modes will now be derived, and the conditions for coupling incident light to this mode will be discussed.

19

2.21 SPP dispersion

Consider as a general case, the interface between two isotropic, semi-infinite media (see figure 2.1). For reflection and refraction of plane waves (TM polarisation) at oblique incidence three fundamental optical laws may be derived: Snell's law, the law of reflection, and Brewster's law. The SPP dispersion may be considered a special case of Brewster's law. As linear dielectrics obey the constitutive equations and the electric displacement **D** will be continuous across the interface we have that:

$$\mathbf{D} = \varepsilon\varepsilon_0\mathbf{E} \qquad (2.1)$$

where ε_0 is the permittivity of free space and ε is the dielectric constant of the medium (this is usually a complex number for real, absorbing media).
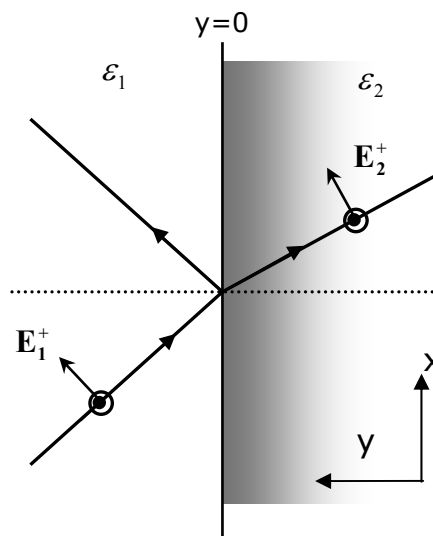
Figure 2.1. Reflection and refraction at a metal-dielectric boundary. The x-y plane is the plane of incidence. The chosen example with a non-propagating reflected wave illustrates coupling to the SPP mode. The **B** fields associated with each ray are directed out of the page along the z-axis.

If the left media is a dielectric with the real part of the dielectric constant a positive number and the medium on the right is a metal

with a negative real part of its dielectric constant, then it is clear from equation (2.1) that the component of **E** normal to the interface will change direction as it crosses the interface. This discontinuity in normal **E** components gives rise to a sheet of polarisation charge trapped at the interface. In the case of time varying, incident waves, the static fields of the above argument need to be replaced with time varying ones. The dispersion relation of the resultant resonant fluctuations can be derived as shown in *Reather* (1988).

Figure (2.1) shows the TM electromagnetic wave incident at the interface between two non-magnetic, semi-infinite media. The medium on the left is a dielectric with dielectric constant ε_1 while the medium on the right is a metal with dielectric constant ε_2. The propagation vectors of the waves are all co-planar and lie in the x-y plane. There is no z-dependence, and the electric field vectors also lie in the x-y plane.

For a non-radiative surface wave solution only one electromagnetic wave need exist in each medium. We can therefore arbitrarily set the reflected ray in the left medium to be zero.

The electric fields of the incident and transmitted beam can be expressed as

$$\mathbf{E_1} = \left[\mathrm{E}_{x1}, \mathrm{E}_{y1}, 0 \right] \exp i\left(k_{x1}\mathbf{x} + k_{y1}\mathbf{y} - \omega t \right) \tag{2.2}$$

$$\mathbf{H_1} = \left[0, 0, \mathrm{H}_{z1} \right] \exp i\left(k_{x1}\mathbf{x} + k_{y1}\mathbf{y} - \omega \mathbf{t} \right)$$

and

$$\mathbf{E_2} = \left[\mathrm{E}_{x2}, \mathrm{E}_{y2}, 0 \right] \exp i\left(k_{x2}\mathbf{x} - k_{y2}\mathbf{y} - \omega t \right) \tag{2.3}$$

$$\mathbf{H_2} = \left[0, 0, \mathrm{H}_{z2} \right] \exp i\left(k_{x2}\mathbf{x} - k_{y2}\mathbf{y} - \omega \mathbf{t} \right)$$

Where k_x and k_y are the respective x and y components the of co-planar propagation vectors. The fields in Eqs. 2.2 and 2.3 obey Maxwell's equations and for systems with no prescribed charge or current distributions we can substitute them into the following curl equation

$$\nabla \times \mathbf{H} = \varepsilon_0 \varepsilon \frac{\partial \mathbf{E}}{\partial t} \qquad (2.4)$$

Substitution of the operators and considering only the tangential field components allows the following expressions to be obtained

$$k_{y1} \mathbf{H}_{z1} = -\omega \varepsilon_0 \varepsilon_1 \mathbf{E}_{x1} \qquad (2.5)$$

and

$$k_{y2} \mathbf{H}_{z2} = \omega \varepsilon_0 \varepsilon_2 \mathbf{E}_{x2} \qquad (2.6)$$

The boundary conditions at the interface require that the tangential E-fields and H-fields be continuous, so from Eq. (2.2) and Eq. (2.3) at y=0,

$$\mathbf{E}_{x1} = \mathbf{E}_{x2} \qquad (2.7)$$

$$\mathbf{H}_{z1} = \mathbf{H}_{z2}$$

Using Eq. (2.5), (2.6) and Eq. (2.7) we obtain

$$\frac{k_{y1}}{\varepsilon_1} + \frac{k_{y2}}{\varepsilon_2} = 0 \qquad (2.8)$$

it can be shown that all of the propagation vectors are coplanar and in accordance with the law of conservation of momentum parallel to the plane of incidence (a consequence of this statement being Snell's law):

$$k_{x1} = k_{x2} = k_x \qquad (2.9)$$

the magnitude of k is determined, for a given frequency ω, by the permittivity of the material ε

$$k = \sqrt{\varepsilon} \frac{\omega}{c} \qquad (2.10)$$

$$k = \frac{2\pi}{\lambda}$$

where λ is the wavelength of light in the medium. Expressing Eq. (2.10) in terms of normal and tangential components of the wavevector we have

$$k_x^2 + k_{yi}^2 = \varepsilon_i \left(\frac{\omega}{c} \right)^2 \qquad i = 1,2 \qquad (2.11)$$

Eq. (2.8) and Eq. (2.11) can be rearranged to give the tangential component of the wavevector

$$k_x = \frac{\omega}{c}\sqrt{\frac{\varepsilon_2 \varepsilon_1}{\varepsilon_2 + \varepsilon_1}}$$

(2.12)

The SPP is a charge oscillation at the interface. The oscillation is longitudinal and has both longitudinal and transverse electromagnetic fields which decay exponentially into the bounding media from the surface where they are at a maximum (y=0). It is this exponential decay into the surrounding medium, which make SPPs so sensitive to surface properties. The charge distribution is shown schematically in figure (2.2) and clearly illustrates the TM nature of the mode. TE radiation has no normal component at the interface and is therefore unable to excite the necessary surface charge distribution that constitutes an SPP.
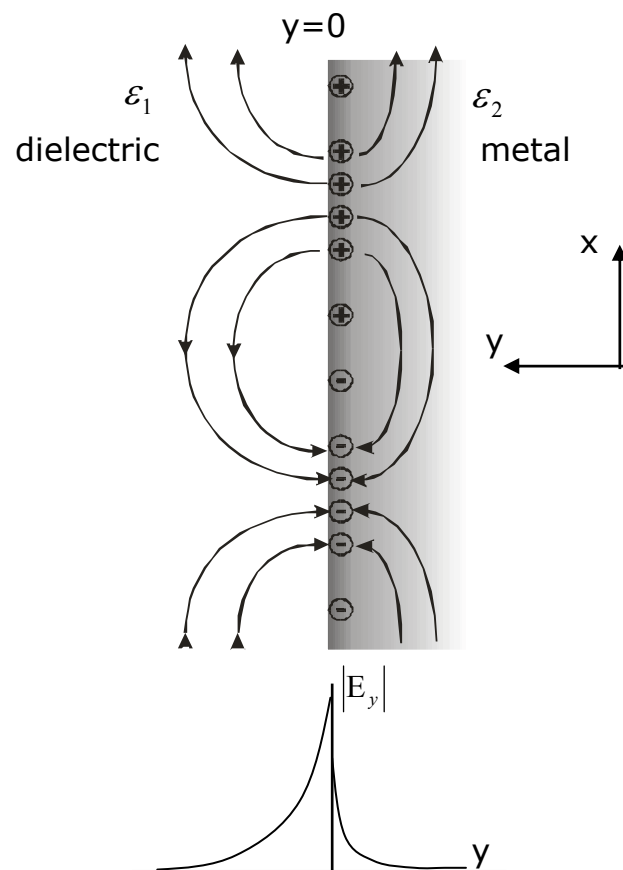
Figure 2.2. The field and charge distributions of the Surface Plasmon Polariton (SPP) mode.

If we introduce a complex number for the metal permittivity we have permittivities described in the following manner:

23

$$\varepsilon_{metal} = \varepsilon_2 = \varepsilon_2' + i\varepsilon_2'' \qquad \varepsilon_2' < 0 \qquad\qquad (2.13)$$

$$\varepsilon_{dielectric} = \varepsilon_1 > 1$$

The imaginary component of the metal permittivity quantifies the losses in real metals. These losses are associated with scattering of electrons from defects, phonons and the surface. Conversely the dielectric permittivity is a real number and describes a loss-less dielectric. This results in the SPP wavevector having both real and imaginary parts. As the SPP propagates the same processes described by the imaginary component of the metal permittivity will damp the SPP. For 'good' metals $|\varepsilon_2'| \gg \varepsilon_2''$ the dispersion relation Eq. (2.12) may be rewritten as

$$k_x' = \frac{\omega}{c}\left(\frac{\varepsilon_2'\varepsilon_1}{\varepsilon_2' + \varepsilon_1}\right)^{\frac{1}{2}} \qquad (2.14)$$

and

$$k_x'' = \frac{\omega}{c}\left(\frac{\varepsilon_2'\varepsilon_1}{\varepsilon_2' + \varepsilon_1}\right)^{\frac{3}{2}} \frac{\varepsilon_2''}{2(\varepsilon_2')^2} \qquad (2.15)$$

For the SPP to be a propagating mode k_x' must be a real number. In Eq. (2.14) (for a metal with $\varepsilon_2' < 0$) this condition is met only if $|\varepsilon_2'| > \varepsilon_1$. The result of these two conditions is the inequality, $k_x' > \sqrt{\varepsilon_2}\,\omega/c$ which has important implications for the SPP dispersion.

The wavevector of a photon propagating in the dielectric will always be smaller than that of the SPP mode. In other words no coupling between the photon and SPP mode is possible and the SPP is non-radiative. In order to excite SPPs on a planar interface some momentum matching method is required. Methods with which to achieve the momentum matching are discussed later in this chapter.

Another consequence of $k_x' > \sqrt{\varepsilon_2}\,\omega/c$ resulting from Eq. (2.11) is that k_{iy} is always imaginary. This means that fields extending out on either side of the boundary are damped and decay exponentially. In the following sections the spatial extent of the SPP fields normal to and along the interface are discussed.

2.22 Propagation length of the SPP.

As already mentioned an SPP propagating along an interface experiences damping associated with phonon scattering etc. The intensity of the SPP dies exponentially as $\exp(-2k_x''x)$ with k_x'' defined in Eq. (2.15). The distance the SPP propagates until its intensity drops to $1/e$ of its initial amount is given by

$$L = (2k_x'')^{-1} \tag{2.16}$$

$$L = \frac{\lambda_0}{2\pi} \left(\frac{\varepsilon_2' + \varepsilon_1}{\varepsilon_2' \varepsilon_1} \right)^{\frac{3}{2}} \frac{(\varepsilon_2')^2}{\varepsilon_2''}$$

It is useful to get a feel for the SPP propagation distance in real systems. For instance, we can consider the interface between semi-infinite aluminium and the emissive semi-conducting material 8-hydroxyquinoline Aluminium (Alq$_3$). Using the fact that the dielectric constant of Aluminium at $\lambda_0 = 527.6 nm$ is $\varepsilon_{Al} \approx (-40.46 + 11.13i)$ and the permittivity of Alq$_3$ at this wavelength is $\varepsilon_{Alq_3} \approx 3.10$ (*Hobson* (a) et al. 2002) we can calculate the propagation distance from Eq.(2.16) to be L~20 μm. As was discussed in the proceeding section SPP modes penetrate into the surrounding media. In the next section the extent of the field penetration is quantified.

2.23 Spatial extension of SPPs.

Substitution of Eq. (2.12) into Eq. (2.11) yields an expression for k_{iy}.

$$k_{iy} = \frac{\omega}{c} \left(\frac{\varepsilon_i'^2}{\varepsilon_2' + \varepsilon_1} \right)^{\frac{1}{2}} \qquad i = 1,2 \tag{2.17}$$

As mentioned above and as a consequence of $k_x' > \sqrt{\varepsilon_2}\,\omega/c$ the wavevector k_{iy} is always imaginary, and so decays exponentially as $\exp(-|k_{iy}||y|)$. The penetration depth is given by $\hat{y}_i = |k_{yi}|^{-1}$. Expressions for the field penetration into each medium are found to be

$$\hat{y}_1 = \frac{\lambda_0}{2\pi} \left| \frac{\varepsilon_2' + \varepsilon_1}{\varepsilon_1^2} \right|^{\frac{1}{2}}$$

(2.18)

and

$$\hat{y}_2 = \frac{\lambda_0}{2\pi} \left| \frac{\varepsilon_2' + \varepsilon_1}{\varepsilon_2'^2} \right|^{\frac{1}{2}}$$

(2.19)

For the same Aluminium/ Alq$_3$ interface considered previously and using the same dielectric constants at 527.6 nm it is found that $\hat{y}_1 \approx 166nm$ and $\hat{y}_2 \approx 13nm$. It is evident that the fields penetrate further into the dielectric layer than into the metal and also that the field penetration into the metal is independent of metal absorption. The relatively long tail off of the SPP fields into the dielectric means that radiative recombination of excitons in the emissive Alq$_3$ close to the metal may couple directly to the SPP. The details of near-field coupling to SPPs and other bound modes and the important consequences of this on OLED operation are discussed in detail in chapters 3 and 5.

2.24 SPP dispersion for a free-electron metal.

Thus far general equations describing the dispersion of an SPP at a metal-dielectric interface have been described. The physical and optical properties of the metal have not been given any detailed consideration. For instance a perfect metal would be described by the permittivity $\varepsilon_m = -\infty + 0i$. In such a case Eq. (2.16) also becomes infinite as the E field is totally excluded from the metal but is also infinite in extent in the dielectric medium. For a perfect metal the dispersion relation Eq. (2.12) reduces to the form $k_x' = \sqrt{\varepsilon_1}(\omega/c)$, which is the equation describing a photon propagating in the dielectric parallel to the interface and hence is called *light-like* behaviour.

Real metals however have greatly varying dielectric constants that alter markedly across the visible part of the spectrum. One simple method of deriving the dielectric response of the metal is to

use the free electron model. The free electron model assumes conduction electrons in a metal are free to move in a constant electrostatic potential. This potential is associated with the positive ion cores spread uniformly throughout the metal. The free electron model also ignores repulsive interaction between conduction electrons. The free electron model describes an ideal gas of electrons and so describes an ideal metal. There are no losses in the metal so the imaginary part of the dielectric constant is zero. The real part of the dielectric constant is given by

$$\varepsilon(\omega) = 1 - \frac{\omega_p^2}{\omega^2}$$

(2.20)

where ω is the angular frequency of the radiation and ω_p is the "*plasma frequency*" of the metal. The plasma frequency of electron oscillations moving in a potential formed by a uniform density of positive ions is given by

$$\omega_p = \left(\frac{Ne^2}{m_e \varepsilon_0} \right)^{\frac{1}{2}}$$

(2.21)

where m_e is the electron mass, e the electronic charge, N the particle density and ε_0 the permittivity of free space. The free electron response of the metal given by Eq. 2.20 considerably modifies the dispersion relation at large values of k_x, the in-plane wavevector. At low k_x the dispersion relation approaches the light line but remains larger than $\sqrt{\varepsilon_1}(\omega/c)$ so preventing the SPP from coupling to light. In this regime $\varepsilon(\omega)$ from Eq. 2.20 is negative and the response is metallic in nature and for very low frequencies approaches the response for a perfect metal i.e. $\varepsilon_m = -\infty + 0i$. As the frequency approaches that of the plasma frequency, $\varepsilon(\omega)$ tends towards zero. The change between negative and positive indicates the transition of the metal's behaviour to that of a dielectric. Effectively the frequency is to too high for the electrons in the metal to respond to. Thus the plasma frequency dictates a metal-dielectric transition for the metal in response to applied optical fields.

We are now in a position to modify the SPP dispersion relation (given in Eq. 2.14) to that for a free electron metal/ dielectric interface by substituting Eq. 2.20 in-to Eq. 2.14. The resulting dispersion diagram is given in figure 2.3 where it is plotted together with the light line, which is the dispersion of a photon propagating at grazing incidence to the interface in the dielectric medium. The light line represents the boundary between "leaky" or accessible modes, which may couple to radiation, and "bound" modes such as the SPP and guided modes (discussed below), all of which are non-radiative. The practical implications of bound electromagnetic modes are further discussed in chapter 5 in respect to organic LED devices.
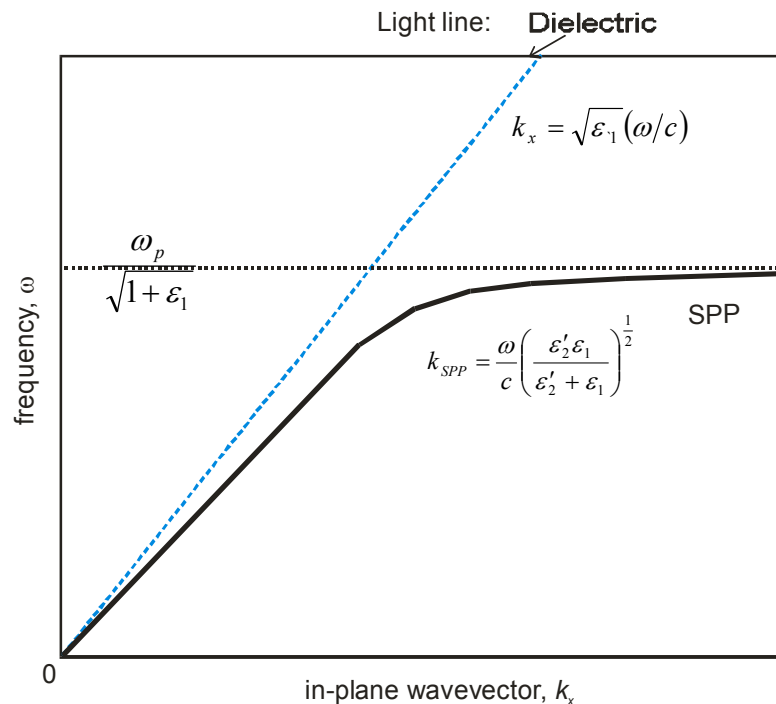
Figure 2.3. The SPP dispersion curve for a free-electron metal surface. The region to the left of the dielectric light line contains the frequencies and wavevectors accessible to photons propagating in the dielectric.

Note that in the limit of large wave vectors the SPP frequency approaches $\omega_p/\sqrt{1+\varepsilon_1}$ known as the *asymptotic surface plasmon frequency* and for a silver-air interface corresponds to an energy of 3.6 eV (345 nm) [*Andrew* (1998)], which is in the UV part of the

electromagnetic spectrum. The approach of this 'flat band' limit results in both the phase velocity (ω/k) and group velocity ($\partial\omega/\partial k$) tending to zero. The flat band indicates that the surface plasmon has a large density of states (DOS) per unit frequency interval of k-space, compared to lower frequencies. If the asymptotic energy level could be reduced to lie in the visible region of the spectrum the enhanced DOS could lead to an increased molecule-SPP interaction. This can in fact be done and, in chapter 6, flat band behaviour of surface plasmons is observed in interactions with aggregate molecular systems.

2.25 Effect of a thin dielectric overlayer on the SPP dispersion

In the work described in chapters 5 and 6 of this thesis the interactions between light-emitting molecules and metals are investigated in various waveguide systems. In these experiments different emissive materials are spun down or deposited by thermal evaporation, both techniques offering a high degree of control over the thickness of the dielectric layer.

The consequences of a thin dielectric over layer on the plasmon dispersion are interesting. For instance, we recall from above that the 1/e spatial extent of SPP fields at an Al/ Alq_3 interface is ~166 nm. If the Alq_3 layer is not semi-infinite in extent, with maybe a 100 nm layer of Alq_3 which has been thermally deposited onto aluminium, the decaying tail of the SPP field will sample air resulting in a metal/ dielectric/ air structure. A schematic of a similar generic structure is given in figure 2.4.

air ε_1
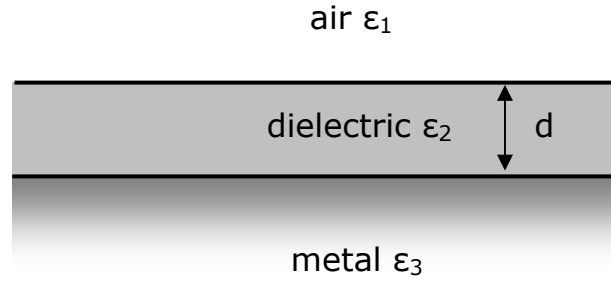
Figure 2.4. Schematic of a metal substrate coated with a dielectric overlayer of thickness d.

Consider the above structure, in which the dielectric thickness d is variable, $\varepsilon_1=1$, $\varepsilon_2>1$. In the limit of d=0 the structure reduces to that of a metal/ air interface and the dispersion relation reduces to that of a single interface problem as outlined in Eq. 2.14 i.e. $(\omega/c)\sqrt{\varepsilon_1/(\varepsilon_1+1)}$. For 0<d<λ, the SPP electromagnetic fields exist in both media (dielectric and air) and the new double interface solution is given by *Kaminow et al.* (1974). It is clear the SPP wavevector will now be greater than in the metal-air case, due to the higher permittivity of the dielectric overlayer. When d>λ the decaying fields associated with the plasmon will lie almost completely within the dielectric, giving once again a single interface solution but with the dielectric constant of air being replaced by that of the dielectric. In conclusion we can say that as the overlayer is increased in thickness from d=0 to d>λ the wavevector of the SPP increases to a new asymptotic value given by

$$\frac{\omega}{c}\sqrt{\frac{\varepsilon_m\varepsilon_d}{\varepsilon_m+\varepsilon_d}} \tag{2.22}$$

where ε_d, is the dielectric permittivity and ε_m is the real part of the metal permittivity. This effect is known as *thickness dispersion* of the SPP mode. Increasing the thickness of the dielectric still further, allows the structure to support waveguides modes as well as the SPP. These modes are the subject of the next section of this chapter.

2.3 Waveguide modes

Waveguides are related to SPP modes in that they too are confined electromagnetic waves. The simplest waveguide structure is shown in figure 2.5. From consideration of this geometry we will show expressions describing electromagnetic waves which allow us to derive the dispersion relation of any waveguide modes which may be present. As can be seen below a typical waveguide consists of a guiding region in which the mode propagates bounded by other regions into which the modes decay exponentially.

Region 2, ε_2 y=d

Region 1, ε_1

                                                      y=0

Region 3, ε_3

Figure 2.5 an asymmetric planar slab waveguide structure.

The analysis of the modes of such structures can be found in various sources e.g. *Kaminow* (1974) and *Wasey* (2001). Assuming a simple harmonic time dependence, guided modes of the system will be solutions of the wave equation with the form

$$\nabla^2 \mathbf{F}(\mathbf{r}) + \omega^2 \varepsilon\mu \mathbf{F}(\mathbf{r}) = 0 \qquad (2.23)$$

where the variable $\mathbf{F} = (F_x, F_y, F_z)$ represents both **E** and **H** since they both satisfy the same equation for a source free region (the z dependency is zero in this case, the waveguide being assumed to extend to infinity in the z-direction). Solutions are chosen which correspond to waves propagating in the x-direction,

$$\mathbf{F}(\mathbf{r},t) = \mathbf{F}(y)\exp i(\beta x - \omega t) \qquad (2.24)$$

where β is the tangential component of the wavevector also called the *propagation constant*. Substitution into Eq. 2.23 and using the

relation $\omega^2\varepsilon\mu=n_i^2k_0^2$ means Eq. 2.23 may be re-expressed in each region as

$$\frac{\partial^2}{\partial y^2}\mathbf{F}_i(z)+\left(n_i^2k_0^2-\beta^2\right)\mathbf{F}_i(z)=0 \qquad i=1,2,3 \qquad (2.25)$$

Before solving these equations explicitly and finding the exact solution of the waveguide dispersion, we can investigate the general form of Eq. 2.25 by examining the nature of the solutions for a given frequency ω as function of tangential wavevector β. For the structure in figure 2.5 to behave as a slab waveguide it needs to be a dielectric bound on either side by lower index dielectric media or metals. In either case the fields of the guided mode are bound in the vicinity of the centre of the guide where the mode will propagate. A good metal will exclude the fields from its interior and a bounding dielectric of much lower index also provide strong confinement via total internal reflection. A convenient choice of structure would be consistent with that already considered in figure 2.4, namely a dielectric slab bounded on one side by a metal and on the other side by a low index medium (e.g. air). This structure is also somewhat similar to the organic LED structures considered in chapter 5, with a planar waveguide formed from an emissive organic dielectric fabricated on a low index glass substrate and capped on top by a metal cathode. Solutions for Eq. 2.25 fall into three distinct regimes, though in each case the fields always decay exponentially into the metal. Figure 2.6 illustrates the three regimes under consideration.

a) Radiative (leaky) modes: $0<\beta<n_2k_0$

The optical fields in both dielectric regions are sinusoidal in nature, the modes not being confined to either dielectric layer because $(1/\mathbf{E})(\partial^2\mathbf{E}/\partial y^2)$ is negative in both dielectric regions. Modes in this regime have in-plane wavevectors below cut-off for total internal reflection at the top interface and therefore may escape as radiation, hence they are known as 'leaky' modes

b) Fully guided (bound) modes: $n_2k_0<\beta<n_1k_0$

Here $(1/\mathbf{E})(\partial^2\mathbf{E}/\partial y^2)$ is negative in the guiding slab and positive in the top dielectric, the fields therefore will be sinusoidal in the guiding layer and exponential in the top dielectric. This regime is above the cut off for total internal reflection into the top layer and light is fully guided in the dielectric slab. The necessary condition for this to occur is $n_1 > n_2$, that is to say the core refractive index is higher than that of the top dielectric.

c) Surface modes: $n_1 k_0 < \beta$

With $(1/\mathbf{E})(\partial^2\mathbf{E}/\partial y^2)$ now being positive in both the guiding slab and the top dielectric layer, the fields will therefore be exponential throughout the structure, since the propagation constant or in-plane wavevector is greater than the value for a propagating wave in all regions. The only modes possible are surface modes such as the SPP, as indicated in figure 2.6 (c).
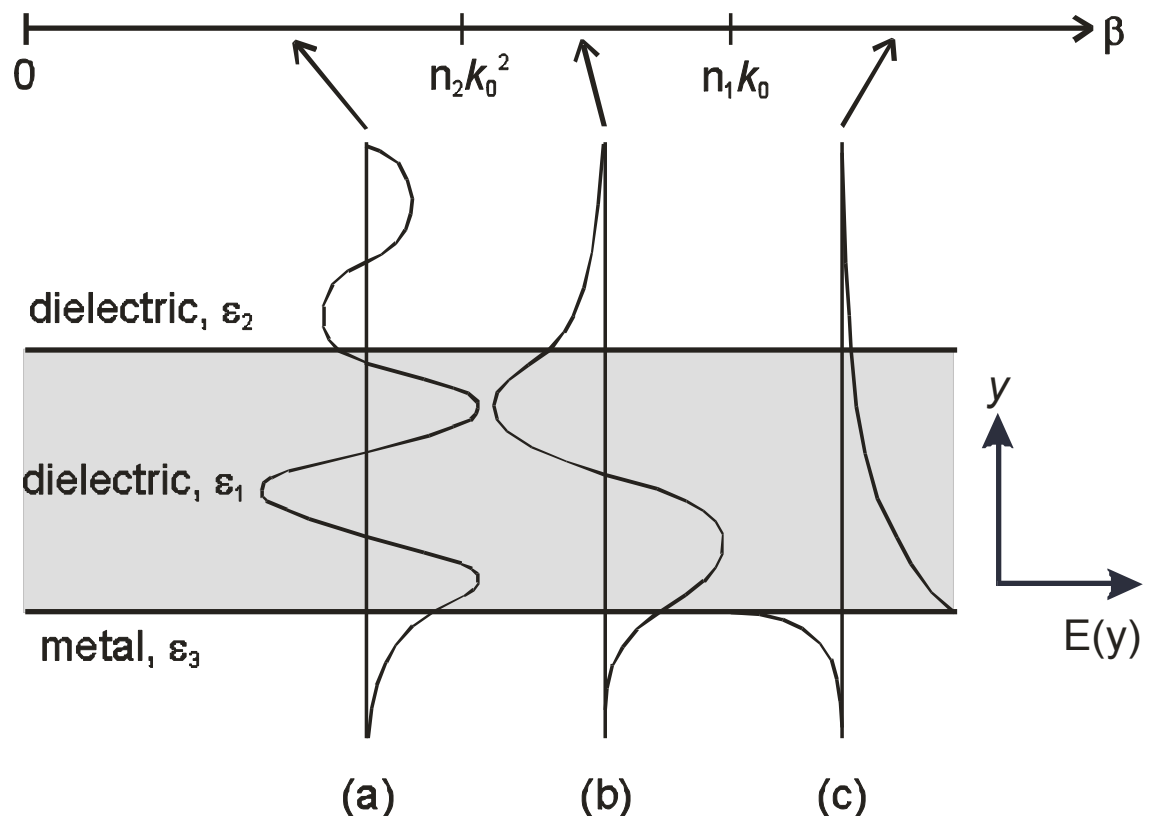
Figure 2.6 Schematic of mode field profiles E(y) of the planar slab waveguide shown in *figure 2.5* the three regimes of guided modes are indicated (a) radiative, leaky or partially guided, (b) fully guided or bound and (c) surface modes.

We have classified the optical modes of a waveguide by their value of in-plane momentum or wavevector. However, we have yet to say anything about the field profiles or the numbers of modes. In the radiative regime there exist a continuum of modes that extend into both layers and β is a continuous variable. In the guided or bound mode regime the dimensions (in this 1D case, thickness) of the guide limit the number of modes together with the frequency ω. The discrete values of numbers of modes arise from total internal reflection at the top and bottom surfaces of the guide, resulting in confinement of the optical field to the guiding layer. An optical mode only occurs when the reflected fields are in-phase. We can now derive the dispersion relation for the fully guided modes. The derivation starts with Maxwell's curl equations.

$$\nabla \times \mathbf{E}(\mathbf{r}) = -i\omega\mu\mathbf{H}(\mathbf{r}) \qquad \nabla \times \mathbf{H}(\mathbf{r}) = i\omega\varepsilon\mathbf{E}(\mathbf{r}) \tag{2.26}$$

Assuming fields and time dependence of the form shown in Eq. 2.24 we obtain

$$\frac{\partial}{\partial y}E_z = -i\omega\mu H_x \qquad \frac{\partial}{\partial y}H_z = i\omega\mu\varepsilon E_x \tag{2.27}$$

$$\beta E_z = -\omega\mu H_y \qquad \beta H_z = \omega\varepsilon E_y$$

$$i\beta E_y + \frac{\partial}{\partial y}E_x = i\omega\mu H_z \qquad i\beta H_y + \frac{\partial}{\partial y}H_x = -i\omega\varepsilon E_z$$

These equations can be split into two self-consistent sets one containing H_z, E_x and E_y and the second containing E_z, H_x and H_y. The magnetic field in the first set is confined to the transverse plane and so corresponds to transverse magnetic (TM or p-polarisation) radiation. The second set has the electric field confined to the transverse plane and so is named transverse electric or (TE or s-polarisation) radiation. Each polarisation can therefore be defined by a single field component namely H_y and E_y. So describing TE radiation by the E_y field component we have

$$\frac{i}{\omega\mu}\frac{\partial}{\partial y}E_z = H_x \qquad -\frac{\beta}{\omega\mu}E_z = H_y \tag{2.28}$$

and describing TM solutions similarly with the single H_y field component we obtain

$$-\frac{i}{\omega\varepsilon}\frac{\partial}{\partial y}H_z = E_x \qquad \frac{\beta}{\omega\varepsilon}H_z = E_y \qquad\qquad (2.29)$$

Each of these types of mode will be considered in turn. The permittivities are complex quantities of the form $\varepsilon_j = \varepsilon_j^r + i\varepsilon_j^i$ where $j=1,2,3$

2.31 TE waveguide modes

Using a standard solution to Eq 2.25 we find that the electric field through the structure will take the following form in each region of the waveguide.

$$E_{z2}(y) = E_{z2}^- \exp(ik_{y2}(y-d)) \qquad\qquad d<y \quad (2.30)$$

$$E_{z1}(y) = E_{z1}^e \cos k_{y1}y + E_{z1}^o \sin k_{y1}y \qquad\qquad 0<y<d$$

$$E_{z3}(y) = E_{z3}^+ \exp(-ik_{y3}y) \qquad\qquad y<0$$

In the guiding layer (0<y<d) a standing wave solution is required and will be of the general form shown in Eq. 2.30 where $k_{yi}^2 = n_i^2 k_0^2 - \beta^2$ (i=1,2,3). Since the condition for surface waves is that they are bound to the surface, this implies that k_{y2} and k_{y3} are imaginary and the normal component of the electric fields will decay away into the bounding media of the guide. Consequently the fields in the dielectric layer are given by

$$E_{z1}(y) = E_{z1}^e \cos k_{y1}y + E_{z1}^o \sin k_{y1}y \qquad\qquad (2.31)$$

$$H_{x1}(y) = \frac{i}{\omega\mu_0}k_{y1}\left[E_{z1}^o \cos k_{y1}y - E_{z1}^e \sin k_{y1}y\right]$$

$$H_{y1}(y) = -\frac{\beta}{\omega\mu_0}\left[E_{z1}^e \cos k_{y1}y + E_{z1}^o \sin k_{y1}y\right]$$

with the last two results arising from Eq. 2.28.

The complementary fields in region 2, the dielectric half space are given as

$$E_{z2}(y) = E_{z2}^- \exp(ik_{y2}(y-d))$$ (2.32)

$$H_{x2}(y) = -\frac{k_{y2}}{\omega\mu_0} E_{z2}^- \exp(ik_{y2}(y-d))$$

$$H_{y2}(y) = -\frac{\beta}{\omega\mu_0} E_{z2}^- \exp(ik_{y2}(y-d))$$

Similarly, electric fields in the metal half space are given by

$$E_{z3}(y) = E_{z3}^+ \exp(-ik_{y3}y)$$ (2.33)

$$H_{x3}(y) = \frac{k_{y3}}{\omega\mu_0} E_{z3}^+ \exp(-ik_{y3}y)$$

$$H_{y3}(y) = -\frac{\beta}{\omega\mu_0} E_{z3}^+ \exp(-ik_{y3}y)$$

Boundary conditions at each interface (y=0 and y=d) require that both E_z and H_x be continuous across the metal-dielectric and dielectric-dielectric interfaces. This condition creates a series of simultaneous equations allowing the dispersion relation to be found. At y=d, the boundary between the dielectric half space and the waveguide, we have

$$E_{z2}^- = E_{z1}^e \cos k_{y1}d + E_{z1}^o \sin k_{y1}d$$ (2.34)

$$-\frac{k_{y2}}{\omega\mu_0} E_{z2}^- = \frac{i}{\omega\mu_0} k_{y1}\left[E_{z1}^o \cos k_{y1}d - E_{z1}^e \sin k_{y1}d\right]$$

similarly at the metal-waveguide boundary (y=0) we have

$$E_{z3}^+ = E_{z1}^e$$ (2.35)

$$\frac{k_{y3}}{\omega\mu_0} E_{z3}^+ = \frac{i}{\omega\mu_0} k_{y1}E_{z1}^o$$

By making the necessary substitutions in Eq. 2.34 and 2.35 we obtain the dispersion relation for the TE waveguide modes.

$$\tan k_{y1}d = -ik_{y1}\left(\frac{k_{y2}+k_{y3}}{k_{y1}^2+k_{y2}k_{y3}}\right)$$ (2.36)

In general this expression cannot be solved explicitly. However we may consider some specific cases where it is possible to solve Eq.

2.36 explicitly. For instance in the regime of a perfect metal $\varepsilon_3 \to -\infty$ and at the metal-dielectric interface $E_{z1}(0)=0$ thus considerably simplifying the expressions for the field in the waveguide. In such a limit the dispersion relation reduces to

$$\tan k_{y1}d = -i\frac{k_{y1}}{k_{y2}} \qquad (2.37)$$

In this case exact solutions can be obtained explicitly. The condition for radiative and guided modes is seen from studying the top solution in Eq. 2.23. The condition for a radiative mode is when k_{y2}^2 is positive, whilst guided modes occur when k_{y2}^2 is negative. The condition $k_{y2}^2 = 0$ is called *cut-off* and corresponds to the transition between the evanescent and propagating regimes. Note that from Eq. 2.37 $\tan k_{y1}d \to -\infty$ at cut-off, which is satisfied when

$$k_{ym1} = (2m+1)\frac{\pi}{2d} \qquad \text{m=1,2,3......} \qquad (2.38)$$

where m is a positive integer which defines the *order* of the mode and denotes the number of zero field crossings in the transverse electric field. At cut-off the tangential wavevector is at a maximum ($\beta = n_2 k_0$) a mode propagating in the dielectric half space may sustain. At this point the electric fields correspond to a plane wave propagating along the interface. If the tangential wavevector increases further then the guided mode regime is reached and from Eq. 2.23, k_{y2}^2 is negative thus requiring k_{y2} to be imaginary, resulting in exponentially decaying fields into the dielectric half-space. With increasing tangential wavevector k_{y2} increases in magnitude although remains imaginary. This results in a reduction in field penetration into the dielectric half space and means that the mode is more completely confined to the slab waveguide.

Recalling the inequality $n_2 k_0 < \beta < n_1 k_0$ that determines whether a mode is guided or radiative, and re-expressing in terms of the normal wavevector yields

$$k_{y2}^2 \leq \left(n_1^2 - n_2^2\right)k_0^2 \qquad (2.39)$$

At cut-off a mode may have attained the maximum possible normal wavevector (k_{y1}) since the tangential wavevector will be at a minimum, substituting this into equation 2.38, we can write.

$$d \geq \frac{2m+1}{\sqrt{n_1^2 - n_2^2}}\frac{\lambda_0}{4} \qquad (2.40)$$

For a thickness d the number of guided modes supported by the structure is limited. Modes can be supported up to an order m given by the inequality in equation 2.40. What is also clear is that m may be so small that no modes for a given wavelength may be supported at all. This has significant implications for practical waveguide structures such as LEDs where guided modes constitute a significant loss to radiative efficiency. Building an LED that operates at below cut-off may help recoup the loss associated with guided modes and is discussed further in chapter 6.

The field profiles of the bound TE modes are given in Eq. 2.31-2.33, with the normal wavevector at cut off obtained from Eq. 2.38. The following section details the treatment of TM guided modes in a similar manner to that described above. Schematics of the field profiles for both TE and TM guided modes are shown in figure 2.7.

2.32 TM waveguide modes

As one would expect, the method for obtaining the dispersion relation for TM guided modes is very similar to that of TE modes. The magnetic field in each region takes the form

$$H_{z2}(y) = H_{z2}^- \exp\left(ik_{y2}(y-d)\right) \qquad \text{d<y} \qquad (2.41)$$

$$H_{z1}(y) = H_{z1}^e \cos k_{y1}y + H_{z1}^o \sin k_{y1}y \qquad \text{0<y<d}$$

$$H_{z3}(y) = H_{z3}^+ \exp\left(-ik_{y3}y\right) \qquad \text{y<0}$$

The tangential components of the electric field in the z and x directions are obtained from Eq. 2.29, derived from Maxwell's curl

equations. As before simultaneous equations are obtained by applying the boundary conditions that H_{z2} and H_{z1} are continuous across the dielectric/ metal and dielectric/ dielectric interfaces allowing the following dispersion relation to be obtained;

$$\tan k_{y1}d = -i\varepsilon_1 k_{y1}\left[\frac{\varepsilon_3 k_{y2} + \varepsilon_2 k_{y3}}{\varepsilon_2\varepsilon_3 k_{y1}^2 + \varepsilon_1^2 k_{y2}k_{y3}}\right] \qquad (2.42)$$

In common with equation 2.36 this equation requires numerical methods to solve. As before a simplified case will be considered namely that of a perfect conducting metal ($\varepsilon_3 \to -\infty$, $k_{y3} \to n_3 k_0$ where n is the complex refractive index) which yields a new dispersion relation of the form

$$\tan k_{y1}d = -i\frac{\varepsilon_1 k_{y2}}{\varepsilon_2 k_{y1}}. \qquad (2.43)$$

This is the dispersion relation for TM modes in an asymmetric waveguide bounded on one side by a perfect metal. At cut-off, as before $k_{y2}=0$, which requires $\tan k_{y1}d = 0$. Thus the normal wavevector of the mode is restricted to the values

$$k_{ym1} = \frac{m\pi}{d} \qquad\qquad \text{m=0,1,2,......} \qquad (2.44)$$

and using Eq. 2.39 the cut-off condition for TM modes is obtained

$$d \geq \frac{m\pi}{\sqrt{n_1^2 - n_2^2}}\frac{\lambda_0}{2} \qquad (2.45)$$

As in the case of TE cut-off, the above expression limits the number of modes supported by a given structure. However, in contrast to the TE case there is no minimum thickness beneath which no modes may propagate. It can be seen for the asymmetric waveguide that there will always exist the lowest order TM waveguide mode, m=0. This mode is identical to the SPP discussed in the previous section which, as we recall, propagates at the metal dielectric interface. Specifically it is clear that the SPP is simply the lowest order TM mode.

The derivation of cut-off equations for non-perfect metals is more complicated than the ideal case presented here. The

expressions for the non-ideal case may be found in work by *Kaminow et al.* (1974) or in *Owyang* (1981).

Schematics of field profiles for the first three TE and TM guided modes for air/dielectric/metal structure are shown in figure 2.7 following the treatment in *Andrew* (1998) for an ideal metal. Here a realistic metal is considered; field penetration into the metal is shown.
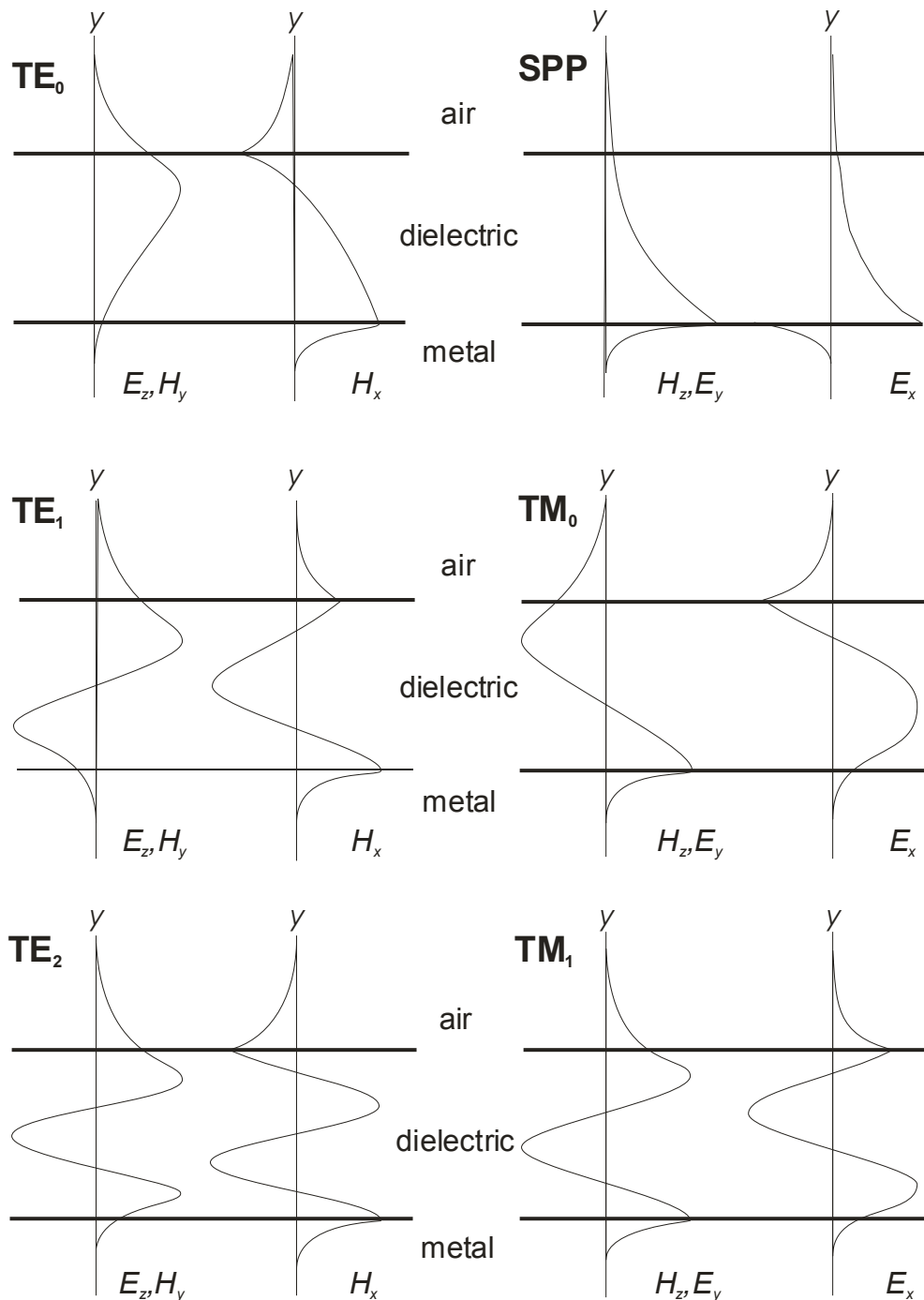
Figure 2.7. Schematic of field profiles of the first three TE and TM guided modes for an air/dielectric/metal waveguide.

2.33 Metal-clad microcavity

The surface and bound modes of an asymmetric waveguide have been described in the preceding section. Now let us consider a different system, namely that of a metal clad microcavity. This structure is the focus of the work discussed in chapter 6 and has other applications in cavity quantum electrodynamics (CQED) discussed in chapter 3.

The metal clad waveguide will follow the form of that shown in figure 2.5 but now consists of a planar dielectric slab bounded on both *top* and bottom by semi-infinite metal mirrors. In such an approximation radiative modes are not present, all fields decaying into the metal. This is of course not a practical system; it would be impossible to perform measurements to probe the optics of the microcavity.

The dispersion relations derived for TE and TM modes in Eqs. 2.36 and 2.42 respectively are equally valid here, but now apply for all values of the tangential wavevector corresponding to propagation in the guiding layer $0 < \beta < n_1 k_0$. Again considering perfect metals ($\varepsilon_2, \varepsilon_3 \to -\infty$) the expressions for TE and TM radiation reduce to the same expression

$$\tan k_{y1} d = 0 \qquad\qquad (2.46)$$

The lowest thickness, d for which the *m*th waveguide mode is supported will occur when $\beta = 0$. Recalling $k_{y1}^2 = n_1^2 k_0^2 - \beta^2$ and substituting into Eq. 2.46 the following result is obtained.

$$d = \frac{m}{n_1} \frac{\lambda_0}{2} \qquad\qquad (2.47)$$

For a given guide wavelength, there is a guide thickness below which no modes can be supported, and again this is known as the cut-off condition.

In the previous case of the asymmetric waveguide the dispersion relation for an SPP mode bound at the metal dielectric was

introduced. As expected the metal clad microcavity also supports SPP modes. In fact it supports two, top and bottom one on each metal/ dielectric interface. In the limit of the dielectric space being very thick, $d > \lambda_0$, the fields associated with each plasmon decay into the cavity without overlapping and each plasmon may be considered a discrete entity. In this case the fields at each interface are identical to those shown in figure 2.2. If the dielectric is thinner than $\sim \lambda_0$ plasmon fields overlap and interact, this means that the modes are now coupled [*Welford and Sambles* (1988)].

There are two fundamental solutions that result form the coupled SPP system. The resulting charge distributions on the metal/ dielectric interface are quite distinct and are shown in figure 2.8.
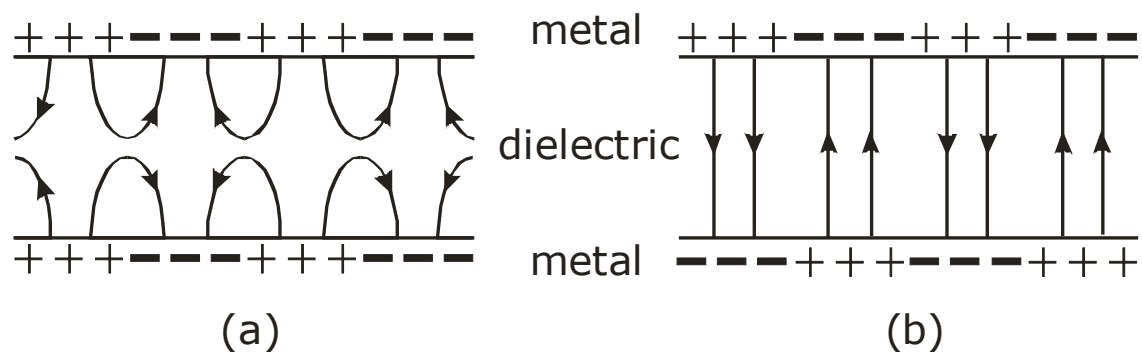
Figure 2.8. Schematic of the charge distribution and electric field lines for the coupled SPP modes of a metal-clad microcavity. The symmetric solution (SRSP) (a) and asymmetric solution (LRSP) (b) are shown.

The symmetric solution (figure 2.8 (a)) has identical charge distributions on both top and bottom metal surfaces. This solution has a greater proportion of its fields located in the metal compared to the asymmetric solution shown in (b). Since metals have greater loss than dielectrics the symmetric SPP will loose energy as heat to the metal more readily than the asymmetric SPP. Consequently the symmetric SPP with its relatively large fields in the metal is called the short range surface plasmon (SRSP). The asymmetric solution suffers lower losses because larger proportions of its fields are within the

dielectric, it is therefore known as the long-range surface plasmon (LRSP) as referred to by *Sarid D* (1981).

From inspection of figure 2.8 it seems that with decreasing guide thickness there is a minimum thickness below which the SRSP charge distribution ceases to become viable. At very close separations the like charges on opposing metal surfaces will repel pushing each other away from the interface. The result of this is that there is a cut-off thickness for the SRSP. These fields at cut-off are identical to those of the lowest order TE guided mode. Unlike the SRSP the LRSP does not have a cut-off thickness.

Above we have discussed the coupling between two similar electromagnetic modes, the result of which is the evolution of two distinct solutions, low energy (LRSP) and high energy (SRSP). Several interactions between similar and dissimilar electromagnetic modes are noted in this thesis. In chapter 5 coupling between a TM waveguide mode and SPP mode is evident, whilst in chapter 6 discussions focus on excitons and TE waveguide modes, which interact to form new quasi-particles. What these diverse interactions have in common is the evolution of two fundamental solutions to describe the interaction and the evolution of a band gap between these modes.

The case illustrated above is ideal, consequently there are no radiative modes associated with the system. In the next section the coupling of radiation to and from bound modes including the SPP mode is examined.

2.4 Coupling to bound modes

In sections 2.2 and 2.3 it was demonstrated that there exists a momentum mismatch between radiative light and waveguide modes and there is a further momentum deficit between the waveguide modes and SPPs. This is to say, guided modes and SPPs are non-radiative i.e. they are bound to the dielectric and the metal surface

respectively. The converse of this situation is also true, namely that light cannot be directly radiatively coupled to these modes without some mechanism to overcome the momentum mismatch. This can be achieved by modifying the surface environment or by modifying the source of light. A number of methods exist to modify the surface environment. The first method briefly discussed in the next section employs a technique known as attenuated total reflection (ATR) to increase the momentum of incident photons, and is also known as *prism coupling*. The second technique to be discussed in this chapter uses a physical texturing of the surface to excite modes and if achieved via a regular periodicity is called *grating coupling*.

In relation to the work on organic LEDs presented in this thesis there is another method by which coupling to the SPP mode may be achieved without altering the surface geometry. An excited molecule, in the vicinity of a metal interface, may directly excite the SPP mode through its near-field radiation thereby de-exciting in a non-radiative manner. This is possible because emission from an excited molecule often closely resembles that of an electric dipole source. In the near-field limit ($d<<\lambda$) the dipole field contains evanescent, high wavevector terms, some of which will match the wavevector of the available SPP mode and if the surface is close enough these will allow excitation of the SPP. In the far field these evanescent waves have decayed away leaving only the propagating plane-wave components of the dipole emission. As we will see, direct coupling between the molecule and bound modes of an asymmetric waveguide are serious limiting factors to the radiative efficiency of LED devices. The experimental work detailed in chapter 5 addresses this problem. The background physics of the coupling between light emitting molecules and cavity modes is further discussed in chapter 3.

2.41 Prism coupling

At the interface between high and low refractive index dielectric media, a beam of light passing from the high to low index region will for incident angles greater than the critical angle ($\theta > \theta_c$) suffer total internal reflection rather than be transmitted. From Snell's law the critical angle for total internal reflection is the arcsine of the ratio of the refractive indices. Specifically, total internal reflection arises because the tangential momentum of the incident light to too high to allow the light to propagate in the low index region. This is not to say that no electric field penetrates the low index medium. An evanescent field is generated at the interface and tails off in the low index medium, its tangential momentum is equal to that of the incident light in the optically dense region. This high momentum, evanescent field provides a suitable mechanism for coupling to SPPs. Methods that employ this coupling are known as attenuated total reflection (ATR) techniques.

A practical system for ATR is to use a glass prism of index n as the optically dense medium and air (index ~ 1) as the low index medium. Light incident at an angle θ normal to the base of the prism will excite an SPP on a metal/ air interface at an angle given by

$$nk_0 \sin\theta_{SPP} = k_{SPP} = k_0 \sqrt{\frac{\varepsilon_{metal}}{\varepsilon_{metal} + 1}} \qquad (2.48)$$

 It should be noted that θ$_{SPP}$ is greater than the critical angle. Coupling to the SPP will be detected in the angle dependent reflectivity measured from the prism-air interface. Reflectivity will rise as the critical angle is approached because the power of the transmitted beam is falling. At and beyond the critical angle the transmitted beam becomes evanescent and the reflectivity rises to 1. Past this point coupling to the SPP may occur at an angle given by Eq 2.48.

Excitation of the SPP manifests itself as a dip in the angle dependent reflectivity. In the event of perfect coupling to the SPP this

dip will drop to zero. The first demonstration of intentional coupling to an SPP using ATR geometry was by *Otto* (1968) (figure 2.9 (a)). In the Otto configuration a metal substrate is introduced into the evanescent field of a high index prism in air. Coupling occurs across the air gap and the SPP is excited on the metal/air interface. The coupling strength of the SPP is determined by the size of the air gap and in optimum condition is the order of the wavelength of the light used. Consequently this geometry is very hard to achieve in the visible regime, particles of dust are often greater than a micron in diameter and so the coupling is better done in the near infrared. The main application of this geometry is the study of surfaces that must not be damaged or touched by the prism, for instance the study of surface acoustic waves on crystals.

| (a) | (b) |
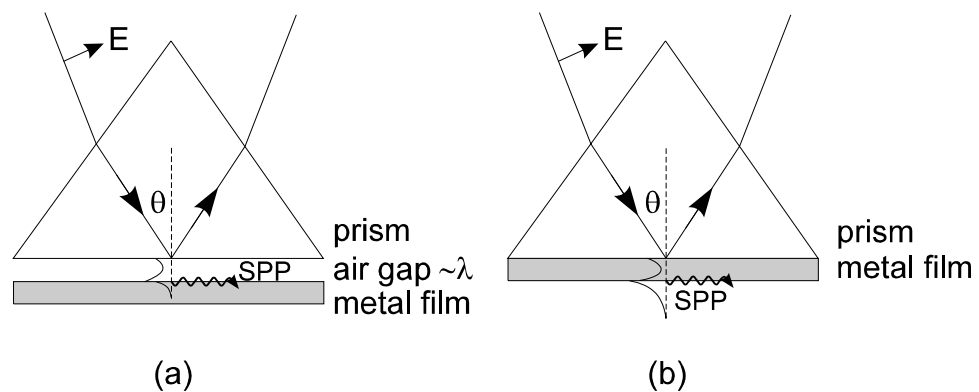
Figure 2.9 a) Otto ATR configuration and b) the Kretschmann ATR configuration for exciting plasmons (diagram taken from Andrew 1998).

An alternative and in many ways more practical geometry was demonstrated by *Kretschmann and Raether* (1968) (figure 2.9 (b)) and entails the metal layer being deposited directly onto the base of the prism. Here the evanescent light field penetrates the metal film and excites the SPP on the air/metal interface, the coupling strength to the SPP may be varied by changing the thickness of the film. The great advantage of this method over the Otto configuration is the ease with which a sample may be made. Thermal evaporation allows the direct deposition of metal films onto the base of the prism with nanometer precision. Figure 2.10 shows theoretically constructed

reflectivity for a bare prism and for a prism with 40 nm of silver deposited on its base.
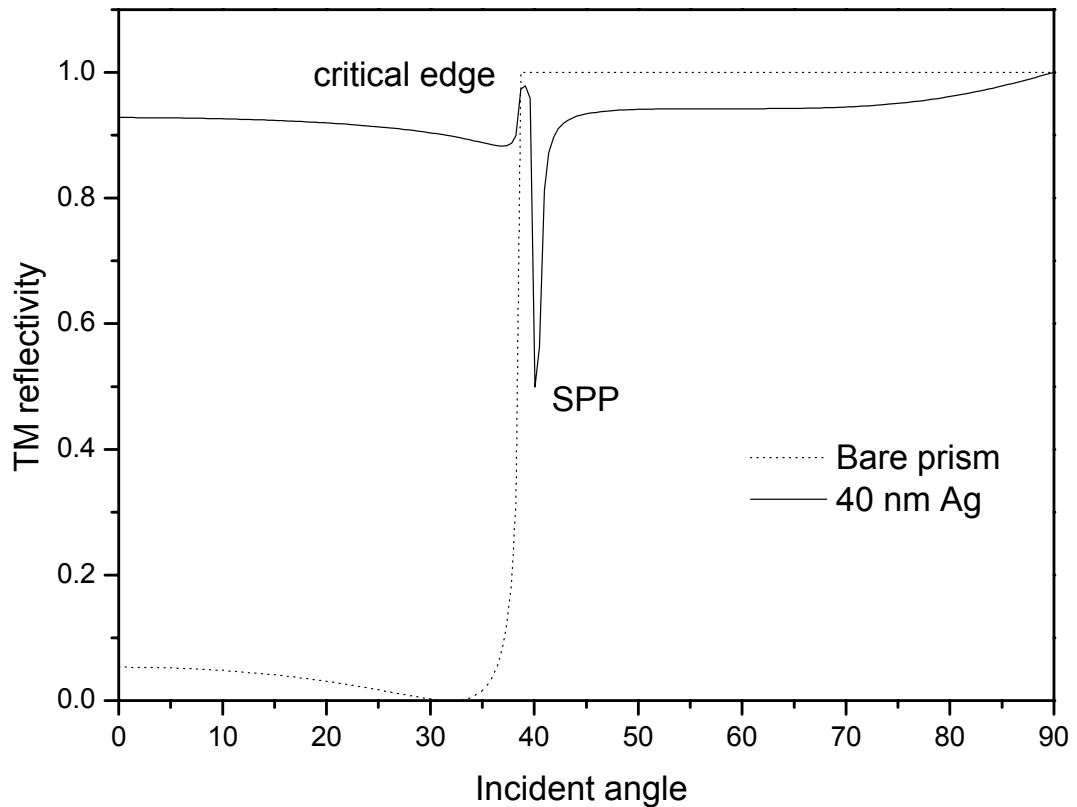
Figure 2.10. Theoretically calculated reflectivity (TM) for a bare prism and one coated with 40 nm of silver ($\varepsilon_{Ag} \approx -17 + 0.7i$) λ= 600 nm.

The surface plasmon mode is clearly evident after the critical edge. The silver thickness of 40 nm is roughly the optimum thickness for coupling to SPP mode. For a layer that is much thicker than this the SPP narrows down to a barely perceptible spike while a thinner layer of silver generates very broad plasmon resonances.

2.42 Grating coupling

One hundred years ago, *Wood* (1902) made a study in which light from fluorescent lamps was reflected from ruled metal diffraction gratings. He found that instead of creating continuous spectra there were a series of unexplained discontinuities that he was unable to explain. *Rayleigh* (1907) demonstrated that some of the spectral anomalies were created by diffracted orders becoming evanescent as they passed beneath the grating horizon. This in turn led to an increase in intensity of the propagating orders. A second set of anomalies remained unexplained until *Fano* (1941) proposed that they corresponded to the excitation of TM polarised surface modes i.e. SPPs.

The periodic or random texturing of the interface between media has the effect of destroying the translational symmetry at the interface, meaning that the momentum of incident light onto the structure need no longer be conserved. Introducing a periodic corrugation allows control of the diffraction process. Light is scattered by an integer number of grating vectors $\mathbf{k}_g$ in a direction normal to the grating grooves. In effect the grooves act like an array of scatterers. Random texturing leaves no control over the magnitude or direction of the grating vector, leaving no control over the direction or frequency of the scattered orders. Fourier analysis of a rough surface shows different frequency components with a range of amplitudes some of which fulfil the requirements for grating coupling. Consequently we will restrict our consideration of textured interfaces to that of periodic corrugations. The grating vector associated with a perfect sinusoidal surface is given by

$$\mathbf{k_g} = \frac{2\pi}{\lambda_g}\hat{\mathbf{n}}$$

(2.49)

where λ_g is the wavelength of the grating or the grating pitch and $\hat{\mathbf{n}}$ is a unit vector pointing in a direction normal to the grating grooves. Light incident on the grating and tangential to the grating vector (the

classical mount) will be split into reflected and transmitted diffracted orders. When a diffracted mode passes over the grating horizon it becomes evanescent and may no longer propagate. The enhanced wave vector associated with the evanescent wave has sufficient tangential momentum to couple to bound modes such as the SPP. For instance the coupling condition for the SPP is given by

$$\mathbf{k}_0 \sin\theta \pm N\mathbf{k_g} = \pm\mathbf{k_{SPP}}$$ (2.50)

where $\mathbf{k}_0 \sin\theta$ is the in-plane momentum of the incident light and $\mathbf{k_{SPP}}$ is the SPP wavevector. It can be seen that if $|\mathbf{k_0}| \gg |\mathbf{k_g}|$, the SPP may be excited at more than one angle of incidence, depending on the number of scattering events that occur. In fact, incident light is able to excite an SPP that propagates in the opposite direction to the incident light. For incident light that is not propagating in the plane of the grating vector, the generated SPP will propagate at some azimuthal angle φ, which is why Eq. 2.50 is a vector relationship. The grating breaks the translational symmetry of the interface.

The corrugation also perturbs the SPP dispersion by decreasing the planar SPP phase velocity at a given frequency [*Pockrand* (1974)], but for shallow gratings this perturbation is small and Eq. 2.12 for planar cases still holds. The strength of coupling to the SPP mode is governed by the amplitude of the corrugation since it is this which determines the intensity of the diffracted orders and hence how much power is coupled to the evanescent fields.

Eq. 2.50 is also applicable for other types of guided mode. More generally we can write

$$\mathbf{k}_0 \sin\theta \pm N\mathbf{k_g} = \pm\mathbf{k_{mode}}$$ (2.51)

where $\mathbf{k_{mode}}$ is the in plane wavevector of a bound mode. For an asymmetric waveguide consisting of metal/dielectric/air the addition of a grating will increase the in-plane momentum of incident radiation, hence allowing coupling to both the SPP and any guided modes that the structure supports. The mechanism for grating

coupling to guided modes and SPP in a waveguide structure is represented in the dispersion diagram in figure 2.11.

Light lines: Air   Dielectric

frequency, ω

TE_0/TM_0

SPP

$- k_g$ $- k_g/2$ $+ k_g/2$ $+k_g$

0   in-plane wavevector, k_x
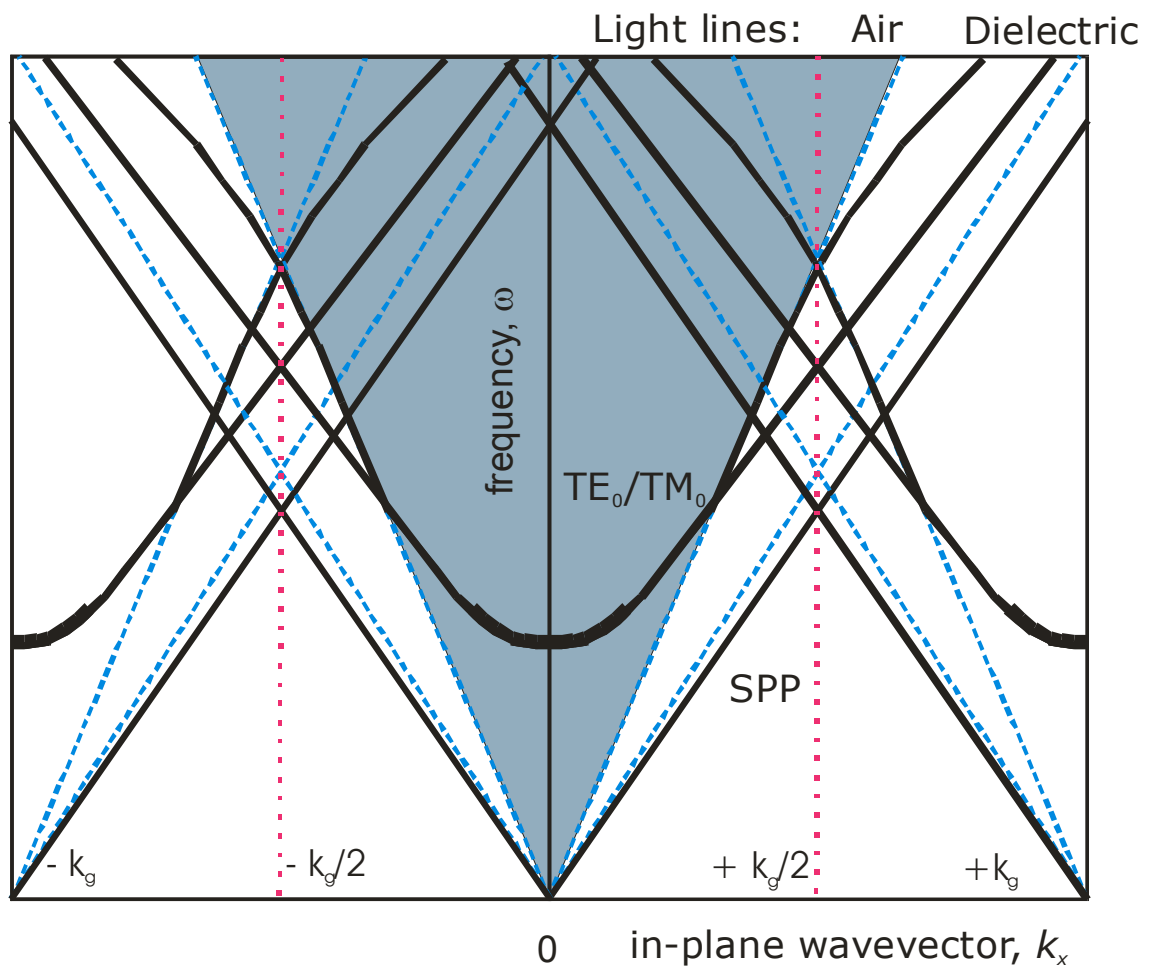
Figure 2.11. Schematic of the photonic band structure for a corrugated asymmetric wave-guide consisting of metal/ dielectric/ air layers. The corrugation has a single harmonic component of pitch λ_g. The shaded region between the dashed lines represents the region accessible to incident photons and hence shows that branches of the SPP and guided mode dispersion curves scattered into this region can be radiatively excited.

Whilst discussing photon-mode coupling it is important to acknowledge that the inverse process, mode-photon coupling may occur. SPPs and guided modes that are normally trapped in a waveguide structure may, due to a grating, suffer a reduction in their momentum such that their momentum is less than that of a photon propagating in air. This allows previously trapped modes to couple to radiation. This is an especially important consideration in LEDs where

emitters may decay, not only radiatively but also into bound modes of the structure and the surface plasmon mode. This phenomenon is discussed in detail in chapter 5.

2.5 EM theory of gratings

To model the photonic band structure of a corrugated multilayer structure, the most important optical properties to calculate are those of reflectivity and transmission at the interfaces. For instance, dips in the measured angle dependant reflectivity indicate coupling to the various optical modes of a system. Furthermore the size of the features indicates the strength of the coupling. Consequently the development of a theoretical framework to model the reflectivity/ and or transmission of a given multilayer structure is of great importance.

Such modelling for a planar multilayer structure is comparatively straightforward. Solutions to Maxwell's equations are sought for each medium and the relevant boundary conditions are applied. This results in the derivation of the Fresnel coefficients [*Pedrotti and Pedrotti* (1993)] for each interface of the waveguide. To obtain the reflection coefficients for the multilayer structure a transfer matrix method may be applied to allow the response of the multi layer system to be calculated. This allows the generation of theoretical reflectivity curves that may be fitted to data taken from a multilayer structure to determine the optical constants and thickness' of the layers.

This technique can also be applied to textured waveguides but is not so easy to implement as the electromagnetic boundary condition at the interfaces are more complicated. The theoretical method to overcome this problem is called the Chandezon formulation and is outlined in the next section.

2.51 The Chandezon technique

In this section we will briefly outline the differential method of *Chandezon et al.* (1982) that accounts for the diffraction of planar electromagnetic waves from gratings. The geometry of the structure in indicated in figure 2.12.
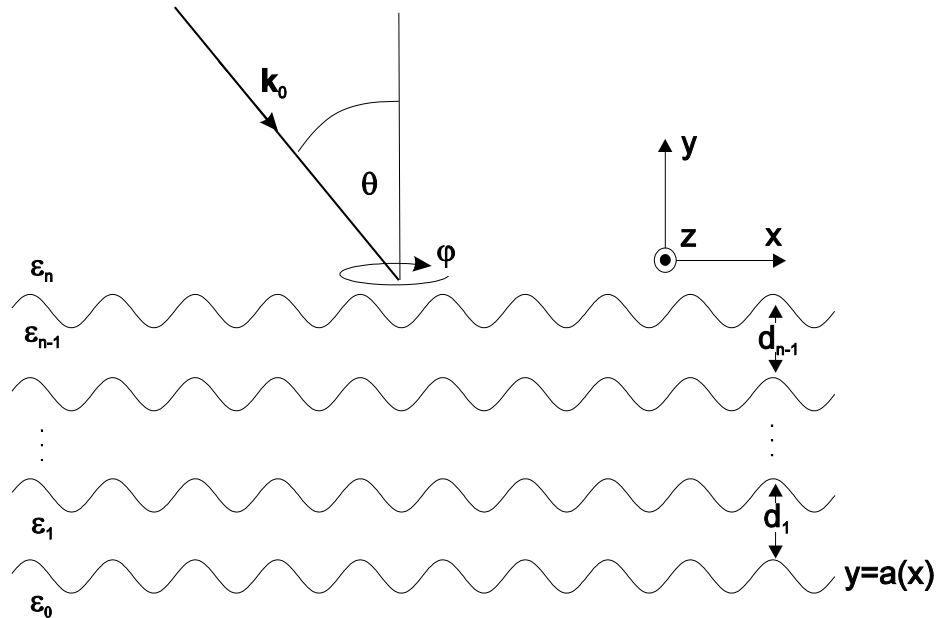
Figure 2.12. Schematic of the multilayer grating geometry and associated co-ordinate system (diagram from *Andrew* (1998)).

The structure consists of a series of corrugated layers, each with the same corrugation and orientated so that the grating vector lies along the x direction. The *i*th layer has a thickness of d_i, a top interface profile of the form $y = a(x)$ and a complex permittivity given by ε_i. Incident light is assumed to consist of monochromatic plane waves, which are incident on the structure from the top medium. The direction of propagation of light is defined by two angles θ and φ. The polar angle θ defines the angle between the normal to the substrate plane and the incident wavevector. The azimuthal angle φ defines rotation of the wavevector from the positive x-direction.

Fundamentally the Chandezon technique involves using a co-ordinate transformation to map the corrugated surfaces onto planes. Given the equation at the interface in Cartesian co-ordinates (x,y,z) is

$$y = a(x) \tag{2.52}$$

a transformation is used to transform to a new co-ordinate system (u,v,w) where

$$u = x \tag{2.53}$$

$$v = y - a(x)$$

$$w = z$$

In this new basis, the interface is a plane and this considerably simplifies the boundary conditions, that the tangential components of **E** and **H** must be continuous across the interface. If the boundary conditions are simplified by the transformation, the form of Maxwell's equations becomes more complex. The solution involves making an appropriate Fourier expansion of these equations in the u-direction to produce an infinite set of differential equations that need to be truncated at some point. The truncation of the differential equations leads to a limit on the number of scattered orders N that may be considered in the calculation. The choice of N is always a balance between realistic computational time spent on the calculation and the accuracy achieved for a given number of modes. The resulting truncated differential equations are solved as an eigenvalue problem [*Chandezon et al.* (1982), *Priest et al.* (1995), *Harris et al.* (1996)].

The computer codes that perform the calculations based upon the Chandezon technique are programmed in FORTRAN and have been expanded by co-workers at Exeter allowing calculations of the entire photonic band structure and the optical fields inside corrugated multilayer waveguides to be carried out.

Current limitations of this code prevent the addition of dipole emitters into the structure, so effectively examining the different routes by which the decaying emitter may lose power, even though an emitter within layered grating structure can be treated in a manner similar to that of a source within a flat layered structure (see chapter 3). The simple optical response of a flat surface needs to be replaced by a scattering matrix to account for the diffracted orders arising from the grating structure. This increases the complexity of

the problem for a source in a corrugated structure. In particular the calculation of decay rate (see chapter 3), for an emitter in a corrugated cavity, would require evaluating the response of this complex system for a detailed portion of 2-dimensional k-space (not reduced to a 1-dimensional problem as in the planar case). Furthermore, for a layer of emitters in the planar structure each emitter will possess the same environment, this will not generally be the case in a corrugated structure. Thus, the computational demands are significantly increased. The development of an appropriate code is underway at Exeter.

2.6 Summary

Many optical devices such as the OLED take the form of an asymmetric metal-clad waveguide and therefore a detailed knowledge of the photonic modes they support is vital if such devices are to be optimised.

In this chapter we have investigated the photonic mode structure of different practical waveguide geometries. We have shown that a SPP mode may propagate at the interface between a metal and a dielectric. Other modes, which may exist in a dielectric waveguide, are a series of TM and TE polarised waveguide modes. The number of waveguide modes in a given structure is dependent on the thickness of the guide. Below a certain thickness called *cut-off* the guide may not support any waveguide modes. It should be noted that there is no cut off condition for the SPP mode, which is also simply the lowest order TM mode of the system. All of these guided modes are non-radiative, that is to say they are bound to the structure by virtue of their high momentum which is greater than that of a photon propagating in air.

Different techniques for coupling radiative light to guided modes have been introduced, among these were grating coupling which employs a periodic corrugation to add or subtract an integer

number of the grating vector to/ from that of the incident light. It was pointed out that as well as coupling incident light into guided modes the coupling mechanism could be usefully employed to couple previously trapped light out of a waveguide structure. Finally the fundamentals of the Chandezon technique for modelling the optical response of corrugated multilayer systems was introduced.

In the next chapter we continue to investigate the interaction between light and matter by introducing various emissive photonic materials to waveguide structures.

Chapter 3
Light-matter interactions

3.1 Introduction

The future of many display and optical communications technologies are dependent upon the development of efficient light emitters and light controlling devices. Already in the field of organic light emitting diodes (OLEDs), wavelength scale waveguides and microcavities play a pivotal role in single and multimode cavity OLED devices [*Dodabalapur et al.* (1996)].

Other wavelength scale structures such as photonic band gap materials are already impacting on optical communications, for instance new photonic crystal fibres known as "holey fibres" have been developed [*Knight and Russell,* (2002)] which can transmit a wide range of wavelengths without suffering from dispersion. The fibre is formed from a regular lattice of air cores running along its length. This chapter introduces two of the underlying interactions between light and matter that are behind some of the current technological advances.

Fundamentally, the interaction between light and matter falls into two regimes, weak and strong coupling. When a molecule in an excited state is placed in some wavelength scale structure, such as a waveguide or microcavity, the presence of the interfaces may alter the emission from the molecule. This occurs because the interfaces modify the boundary conditions of the electromagnetic field within the structure. In the weak coupling regime the interaction between light and matter simply causes a perturbation of the material system. For example, excited molecules in a layer of the waveguide structure will directly couple to the photonic modes of the structure (described in chapter 2; sections 2.2-2.4). In this process there is an irreversible decay of an excited molecule through spontaneous emission (SpE).

In strong coupling, the circumstances are very different. Here the light-matter interaction alters the photonic modes of a material system. When a photonic mode of a microcavity is in resonance with an excitonic energy level a pair of coupled modes may be formed. This is known as strong coupling. These systems undergo Rabi oscillations where energy is swapped between the photonic mode and the oscillator. In real systems the Rabi oscillations are damped and the coupled system rapidly decays into a photon, which may escape the system and an oscillator in the unexcited state.

By altering the lifetime of the photon the decay of the excited state may be controlled. This engineering of the SpE process is attractive in optical applications and in the weak regime has involved the development of the resonant-cavity light-emitting diode (RCLED) with brighter, more efficient and spectrally narrower emission [*Hunt et al.* (1992), *Schubert et al.* (1992)] than a conventional LED.

In this chapter we look at the fundamentals of weak and strong coupling in turn. We begin initially with the weak regime (sections 3.2 and 3.3) by reviewing SpE near interfaces. We lay out the basic concepts and outline an appropriate theoretical model and finish by examining the decay routes open to an emitter located in a waveguide structure. Following this, a practical application of the planar cavity in the weak coupling regime is examined by considering OLED devices. We finish by examining strong coupling (section 3.4) in atomic and semiconductor physics and the further impact of organic photonic materials on this field.

3.2 Spontaneous emission

Spontaneous emission is the process by which an excited atom or molecule (generically termed an emitter) de-excites by emitting a photon. The probability of SpE is given by Fermi's golden rule [*Fermi* (1932)]

$$\Gamma(\omega) = \frac{\pi}{2\hbar^2} \left| \left\langle \varphi_f \middle| H \middle| \varphi_i \right\rangle \right|^2 \rho(\omega),$$ (3.1)

where $\Gamma(\omega)$ is the rate of transition between the excited state $\left| \varphi_i \right\rangle$ of the emitter (in the absence of a photon) and $\left| \varphi_f \right\rangle$ the final state of the emitter (with a single free photon). The Hamiltonian for the emitter-field interaction is $\left| H \right|$, while $\rho(\omega)$ is the density of photon states at the transition frequency, hereafter referred to as the photonic mode density (PMD). The PMD can be described as the number of photonic modes per unit frequency.

Our starting point is a proposal made by *Purcell* (1946) regarding the possibility of controlling spontaneous emission in the microwave regime through the relaxation of nuclear spins. He observed that the rate of SpE for a two level system is increased if the atom is surrounded by a cavity tuned to the transition frequency ω. Approximately, the rate of SpE in the cavity $\Gamma_c(\omega)$ is

$$\Gamma_c(\omega) \approx Q\Gamma(\omega)$$ (3.2)

where Q is the quality factor of the cavity, given by

$$Q = \frac{\omega}{\Delta\omega}.$$ (3.3)

Here, $\Delta\omega$ is the resonance width of the cavity. It can be shown [*Kleppner* (1981)] that $Q \propto \rho(\omega)$ the PMD at the transition frequency. Further work by *Kleppner* (1981) indicated that the rate of SpE can be modified by the boundary conditions imposed by a cavity in the optical regime. The importance of the PMD on the rate of SpE is partly due to the separation of the emitter from an interface and the wavelength of emission.

Consider the idealised case of an excited emitter inside a perfect loss-less microcavity. When the emitter decays the modes of the cavity will be excited. This energy is trapped within the perfect cavity and may not radiate into free space. The photon energy may therefore cause re-excitation of the emitter and thus re-initiate the entire process again. We cannot disassociate the cavity photon from the

emitter and need to consider the composite system as a separate entity.

3.21 Spontaneous emission near planar interfaces

We recall from chapter 2 that beneath a critical cavity dimension (thickness) known as *cut-off,* a planar cavity may not support guided modes. For an emitter placed in such a cavity, owing to the destructive interference of the fields reflected by the cavity boundaries with those of the emitter, the emitter is unable to de-excite and SpE is inhibited.

Though the case described above is idealised, similar effects may be observed in the non-ideal systems such as metal-clad microcavities and asymmetric waveguide structures previously considered in chapter 2 (section 2.3). If we consider an emitter close to a metallic interface, the field reflected by the interface will interact with the emitter, creating a feedback situation. If the reflected field is in phase with the oscillating emitter then the PMD will be high at the emitter site. The SpE rate will be enhanced and emission will be enhanced. Conversely, if the reflected field at the site of the emitter is out of phase with the emitter then SpE is inhibited.

Drexhage (1974) undertook the first experiments that proved that the SpE rate could be modified by changing the local PMD. The results of *Drexhage* were recently reproduced by *Andrew* (1998) and are shown in figure 3.1. Here the modified SpE lifetime $[=1/\Gamma(\omega)]$ as a function of emitter-mirror separation is shown for a monolayer of Eu^{3+} ions above a silver mirror. Eu^{3+} ions have an emission dominated by a single feature at 614 nm. Furthermore the ions are free to rotate rapidly within the spontaneous emission lifetime (~1 ms) resulting in an effectively random dipole emitter distribution. Control of the spacing between the ions and the mirror was achieved using multilayer Langmuir-Blodgett films. These data directly follow the results of *Drexhage*. There are three important features to note.
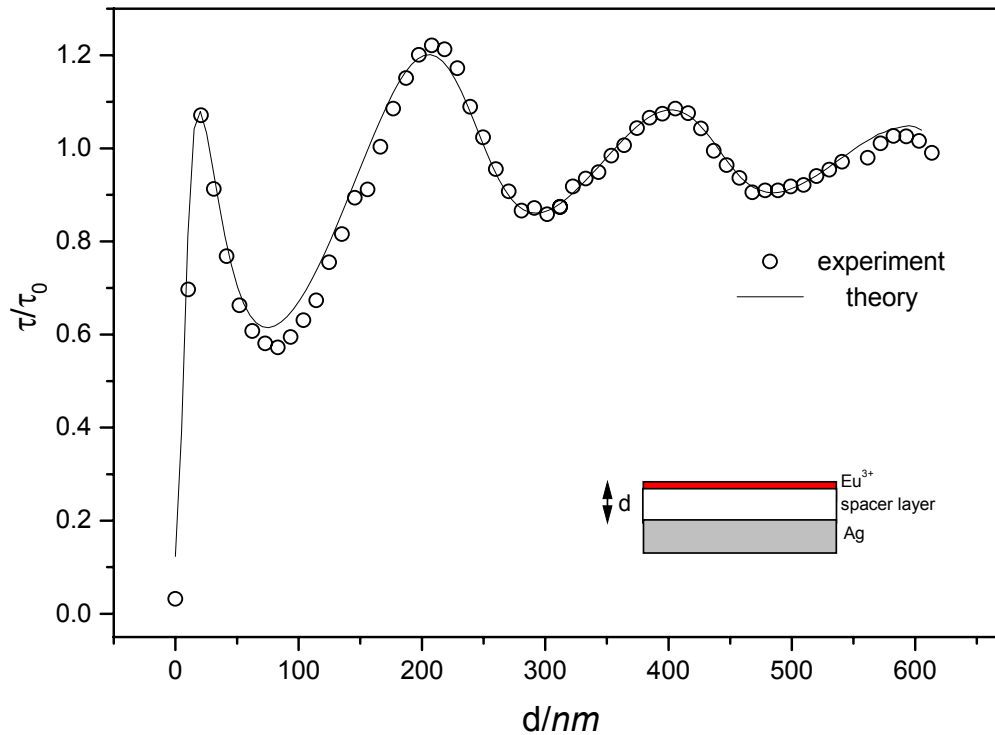
Figure 3.1. The distance dependence of the lifetime τ of Eu^{3+} ions located in front of a silver mirror. The open circles are experimental data, whilst the line is from a theoretical model described in the following section. The inset shows the sample geometry. τ_0 is the lifetime in free space. From *Andrew* (1998).

a)   There is a clear oscillation in the lifetime for dipole mirror separations d > 50 nm.

b)   The oscillations are damped with increasing distance d.

c)   SpE is strongly quenched at low emitter mirror separations (d < 50 nm).

Feature a) arises due to the phase of the reflected field changing with distance, SpE is in turn inhibited then enhanced with increasing distance. The damping feature b) arises due to the point source nature of the emitter whose field (and hence reflected field) will decrease with distance. Feature c) arises from a significant increase in decay rate as the ion-mirror separation decreases. This corresponds to direct coupling between the dipole field and the surface plasmon polariton (SPP) at the metal/ dielectric interface

introduced in the previous chapter, and also from direct losses to the metal [*Barnes* (1998)].

3.22 Modelling dipole emission

Now we will briefly outline the salient points of a classical theoretical approach for modelling the decay of an emitter. This model can provide insight into the different routes by which power may be lost by the emitter and is the basis for modelling how the dipole dissipates power to the radiative and non-radiative modes in organic LED structures considered in chapter 6.

The emitters are considered to be electric dipole oscillators because many radiative molecular transitions are electric dipole in nature. This theory models the effect of nearby interfaces on the decay rate of the emitter by applying appropriate boundary conditions to Maxwell's equations [*Chance* et al. (1978)]. Several assumptions are made in such a model; these are as follows:

- The interfaces are perfect planes that are infinite in extent.
- The media are isotropic and are characterised by a dielectric permittivity ε.
- A point dipole approximation is used i.e. the wavelength of the radiation λ and the separation between the emitter and an interface must be large compared with the size of the dipole.
- The dipole is embedded in a loss-free medium i.e. the permittivity is solely real.
- None of the media exhibit gain at the emission wavelength.

As mentioned above, the dipole is treated as a forced damped harmonic oscillator. Forced, because the reflected field acts to drive the emission and damped because the emitter radiates power. The equation of motion for the electronic dipole moment p is thus,

$$\frac{d^2 p}{dt^2} + \omega_0^2 p = \frac{e^2}{m} E_r - D_0 \frac{dp}{dt} \tag{3.4}$$

where ω_0 is the oscillation frequency in the absence of all damping, e is the electronic charge, m is the effective mass of the dipole, E_r is the component of the reflected field in the direction of the dipole at the dipole site and D_0 is the damping constant (inverse lifetime) in the absence of any interfaces.

The form of equation 2.1 is identical to that describing the physical behaviour of a damped mechanical oscillator driven by an alternating force [*Pain* (1993)]. The reflected field and dipole oscillate at the same complex frequency with solutions that take the form

$$p(t) = p_0 \exp\left[-\left(i\omega_0 + i\Delta\omega_0 + \frac{D}{2}\right)t\right] \tag{3.5}$$

$$E_r(t) = E_0 \exp\left[-\left(i\omega_0 + i\Delta\omega_0 + \frac{D}{2}\right)t\right]$$

where $\Delta\omega_0$ and D are the frequency shift and the damping rate, respectively in the presence of the interface. By substituting Eqs. 3.5 back into Eq. 3.4 and equating real and imaginary components we may obtain

$$\Delta\omega_0 \approx \frac{D^2}{8\omega} - \frac{DD_0}{4\omega} - \frac{e^2}{2p_0 m\omega}\text{Re}(E_0) \tag{3.6}$$

$$D = D_0 + \frac{e^2}{p_0 m\omega}\text{Im}(E_0)$$

where D_0 is the damping rate in the absence of any interfaces [*Kuhn* (1970)] and is given by

$$D_0 = \frac{e^2 k_0^3 \sqrt{\varepsilon_1}}{6\pi\varepsilon_0 m\omega} \frac{1}{q} \tag{3.7}$$

where ε_1 is the relative permittivity of the medium in which the dipole is located, q is the radiative quantum efficiency of the emitter in the medium and $k_0 = \omega/c$.

The frequency shift $\Delta\omega_0$ is very small and for emitters in the visible the damping rate is sufficiently small that the first two terms

in Eq. 3.6. may be ignored [*Chance et al.* (1975)]. For Eu^{3+} ions considered in the Drexhage plot in figure 3.1 the frequency shift is oft the order of megahertz [*Barnes* (1997)], negligible at optical frequencies. From Eq. 3.6 we note that the damping rate and frequency shift are related to the out of phase and in phase components of the reflected electric field at the dipole site respectively.

To find the relative change of the decay rate upon introducing a nearby interface, the reflected electric fields at the dipole site are all that is required [*Sommerfield* (1949)]. Having determined the fields of the system it is then possible to determine the Poynting vector. This allows calculation of the energy flux into the far field and through interfaces of the waveguide structures. This theoretical formulation is useful as it allows the modelling of radiation patterns from planar OLED devices.

One point that has not explicitly been stated thus far is the importance of the location of the emitting dipole within the waveguide. Returning to the experiment of Drexhage (figure 3.1.), the emitter was spaced from the metal mirror by using multilayer Langmuir-Blodgett films. With sufficiently thick spacer layers the structure may support TE and TM waveguide modes as well as the SPP (see chapter 2, section 2.3). In fact for a given spacer layer we can, by altering the position of the dipoles with respect to the waveguide field profiles throughout the guide, alter the relative importance of the photonic modes in the emission process and hence alter the strength of the coupling to radiation. In terms of practical devices such as OLEDs this means that where electron-hole recombination takes place may, to a great extent, control the radiative efficiency and to some extent the spectral range of the device [*Dodabalapur* et al. (1996)].

To summarise, the decay of an excited molecule is greatly modified by the optical environment. By considering a dipole in a waveguide structure the conditions for coupling between the emitter

and the photonic modes supported by the waveguide may be investigated. We will now leave the theoretical model and discuss the excited states of molecules and atoms within materials.

3.23 Excitons

A mobile molecular excited state is referred to as an exciton and is a bound electron-hole pair. Recombination of excitons results in their annihilation and may generate a photon. This is the mechanism that generates light in OLED devices. Depending on their degree of de-localisation excitons can be identified as either the strongly bound Frenkel or delocalised Wannier-Mott exciton. Both are well known and are described in standard textbooks such as *Kittel* (1996).

An electron and hole may be bound by their mutual coulomb attraction in a similar manner to a hydrogen atom. The exciton may travel trough a medium and transport energy, but due to being electrically neutral it may not transport charge. All excitons are unstable with respect to the ultimate recombination process of the electron 'dropping into the hole' and emitting a photon.

Frenkel excitons correspond to a correlated electron-hole pair localised on a single molecule or atom. Its radius is comparable to the intermolecular distance or the size of the molecule. The Frenkel exciton is essentially the excited state of a single molecule, but is able to hop from molecule to molecule by virtue of the coupling between neighbours. Frenkel excitons appear in molecular materials because the covalent bonding between molecules is strong compared to that arising from Van der Waals bonding.

Wannier-Mott excitons arise in uncorrelated, crystalline materials, in which overlap between neighbouring atoms reduces Coulomb interaction between an electron and hole leading to large exciton radii (4 ~ 10 nm) which is many times the size of the lattice constant. Both types of exciton are illustrated in figure 3.2. These

excitons are not found in van der Waals bonded molecular organic solids.

(a) Frenkel exciton   (b) Wannier exciton
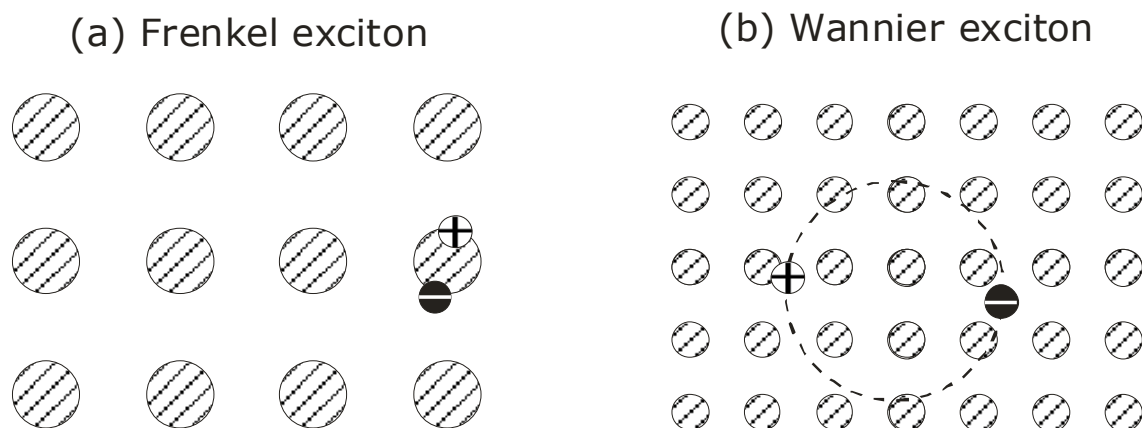
Figure 3.2. An exciton is a bound electron hole pair, usually free to move through a crystal. (a) shows a Frenkel exciton localised on one molecule. (b) shows a Mott-Wannier exciton with a electron-hole separation large in comparison to the lattice spacing.

In the next section we examine organic light-emitting diodes (OLEDs). These devices are well suited to the study of many of the properties of excitons in molecular thin films. Excitons form and recombine in well-defined regions within the OLED; with control over recombination it is possible to effectively study and model emission into the photonic modes of the device [*Dodabalapur* et al. (1996)].

3.3 Organic light-emitting-diodes (OLEDs)

As opposed to photoluminescence (PL) (defined as light emission resulting from the optical absorption of a photon and subsequent relaxation by radiative decay of an excited emitter), excitation of electroluminescence (EL) is achieved via the injection of charge carriers (electrons and holes) into an organic semiconductor from an external circuit.

The simplest form of OLED is a single organic layer device, consisting of either an emissive electron or emissive hole-transporting

layer sandwiched between an anode and a cathode. One of the electrodes needs to be partially transparent to allow light to pass through it. This is usually the anode for which the semi-transparent material indium tin oxide (ITO) is usually employed. A schematic of a generic OLED device is shown in figure 3.3.
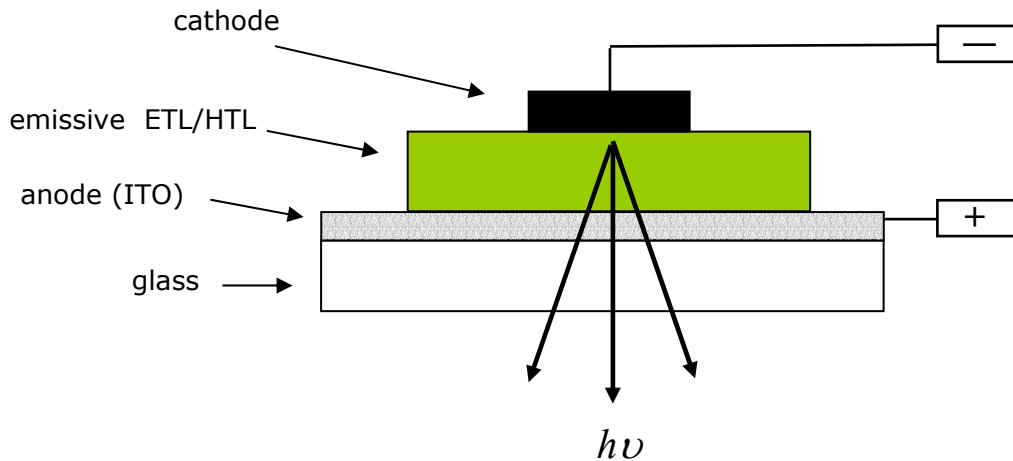
Figure 3.3. Schematic configuration of a single-layer OLED. The active layer may either be an emissive electron transport layer (ETL) or an emissive hole transport layer (HTL).

Tang and VanSlyke (1987) invented the modern organic LED device. Their active emissive layer was a fluorescent metal chelate complex, called 8-hydroxyquinoline aluminium (Alq$_3$) which also acted as an electron transport layer (ETL). This was the first "small molecule OLED" device. OLEDs using an electroluminescent conjugated polymer material (poly(*p*-phenylene vinylene (PPV)) were reported soon afterwards (*Burroughes et al.* (1990)) and recent prototype devices meet realistic device specifications [*Friend et al*. (1999)]. The basic principles of electroluminescence outlined above are essentially the same no matter which type of organic material (polymer or amorphous small molecule) is used. The choice of materials is usually determined by the preferred method of fabrication. Polymer OLED systems are generally spin cast [*Friend et al*. (1999)] from solution onto appropriate substrates or even sprayed down from the nozzle of an inkjet printer [*Comiskey et al.* (1998)].

Because of their low molecular weight small molecule organic materials may also be vacuum deposited as thin films. Because the work presented in this thesis (chapter 5) deals with the manufacture of textured OLED devices, the choice of vacuum deposited devices over spun polymer was considered prudent. The top surface, of spun films of long chain polymers, has been shown to planarise the textured surface onto which they are deposited [*Turnbull et al.* (2001)]. In contrast, vacuum deposited organic layers closely follow the profile of the interface below.

Many OLED devices, including that of *Tang and VanSlyke* (1987), take the form of molecular heterostructures and are composed of two layers, one for hole transport and one for electron transport/EL, successively deposited onto an ITO anode. This allows a greater control over electron and hole injection rates by creating barriers for charge transport at the heterojunction where recombination takes places. By altering the position of recombination within the device the coupling of the exciton to the photonic modes of the device is also altered. The mobilities of electrons and holes in organic films often vary considerably. The result of this is that without a heterojunction, recombination will take place far closer to one interface than the other. Other non-radiative decay routes besides the SPP exist for exciton recombination very near (≤15 nm) to the metal-organic interface. These effects are called lossy waves and compete directly with coupling to the SPP [*Barnes* (1998)]. But, for larger emitter-cathode separations (>15nm for OLED structures considered in chapter 5) coupling to the SPP is the most likely decay route [*Hobson (a)* (2002)].

The OLEDs fabricated in the course of the work all used Alq_3 as the electron transport/ emissive layer. Such metal chelate-based molecules are the most prevalent electron transport emitters in organic EL devices. Thin films of Alq_3 are known to be morphologically stable films and exhibit green photoluminescence.

For a hole transport layer, a a commonly used triarylamine derivative, N,N′-diphenyl-N,N′-bis(3-methylphenyl)-1,1′-biphenyl-4,4′-diamine (NPD) was employed [*Mitschke and Bäuerle* (2000)]. The chemical structures of Alq₃ and NDP are shown in figure 3.4. Unfortunately vacuum deposited NPD has been found to crystallise at ambient temperature after a few days. This film instability is an important limiting factor in device lifetime [*Kato et al.* (2001)]. The change in morphology of the film is caused by a transition of the film from an amorphous non-equilibrium state to a crystalline equilibrium state. The ease of this migration seems dependent on the density or molecular packing in the film, which is in turn dependent on the temperature of deposition. These problems may be overcome by blending NPD with an inert polymer matrix (*Mitschke and Bäuerle* (2000)).
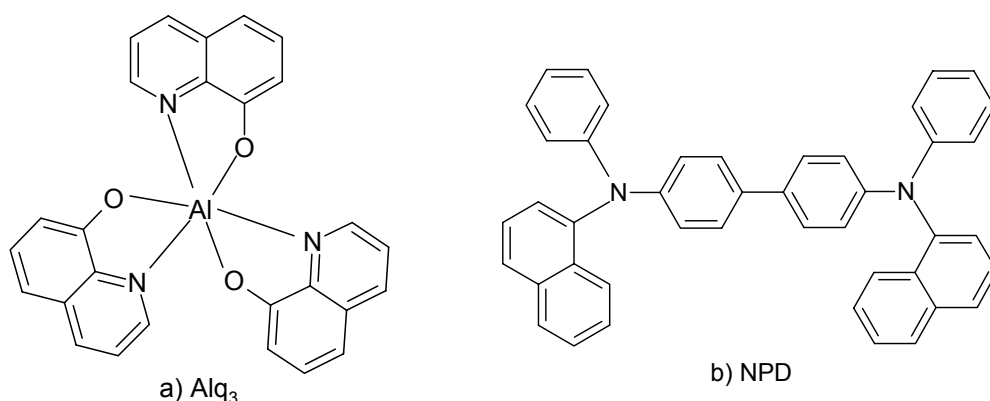
Figure 3.4. Chemical structure of a) Alq₃ and b) NPD.

The characteristic green emission of Alq₃ seems slightly surprising in light of the fact that the optical absorption is typically around 2.7 eV [*Rajagopal* et al. (1997)]. The reason for the large shift between absorption and emission wavelengths is due to the molecular excited state relaxing via phonon generation and is illustrated in figure 3.5. This process, known as the 'Stokes shift' is common in most other molecular organic compounds [*Farchioni and*

Grosso (2001)]. The large Stokes shift in Alq_3 renders the molecule almost completely transparent to its own radiation
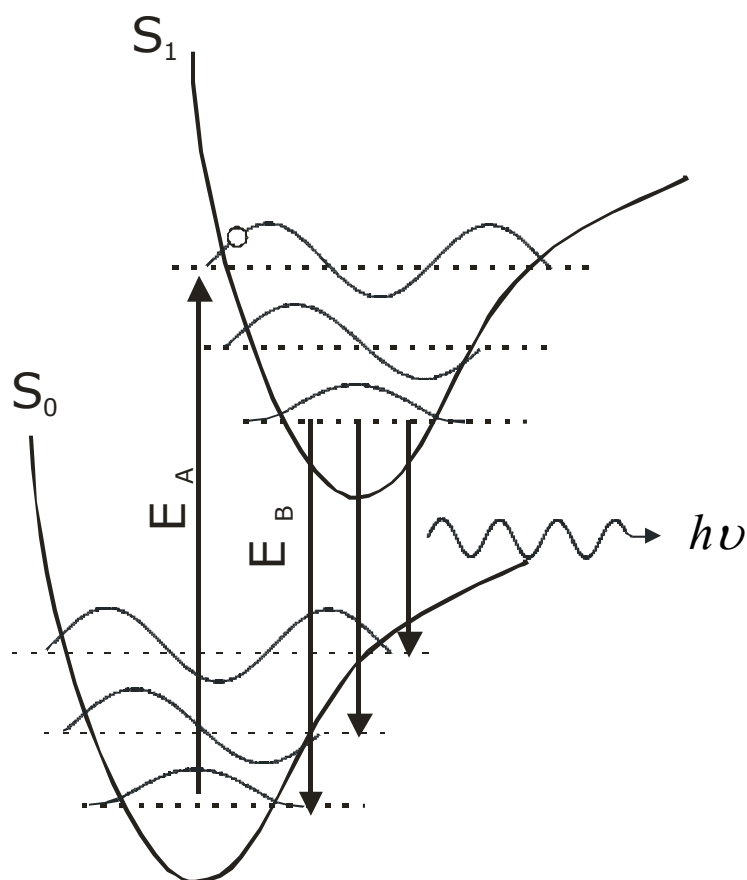
Figure 3.5. Diagram of molecular electronic states S_0 and S_1 of a diatomic molecule. The dashed lines indicate vibrational energy levels. On top of this the vibration wavefunctions of the molecule are drawn.

Figure 3.6 shows a schematic of the planar OLED structure considered in this work. We note the use of an Al/LiF bilayer as an efficient electron-injecting contact into the OLED device. The presence of the thin LiF layer has been found to significantly improve electron injection into the organic layer [*Van Slyke et al.* (1996) and *Jabbour* et al. (1997)]. It may seem strange that LiF, an insulator, may be able to enhance electron injection into the device. One may attribute this fact to tunnelling injection between the Al and Alq_3 layers [*Jabbour et al.* (1997)]
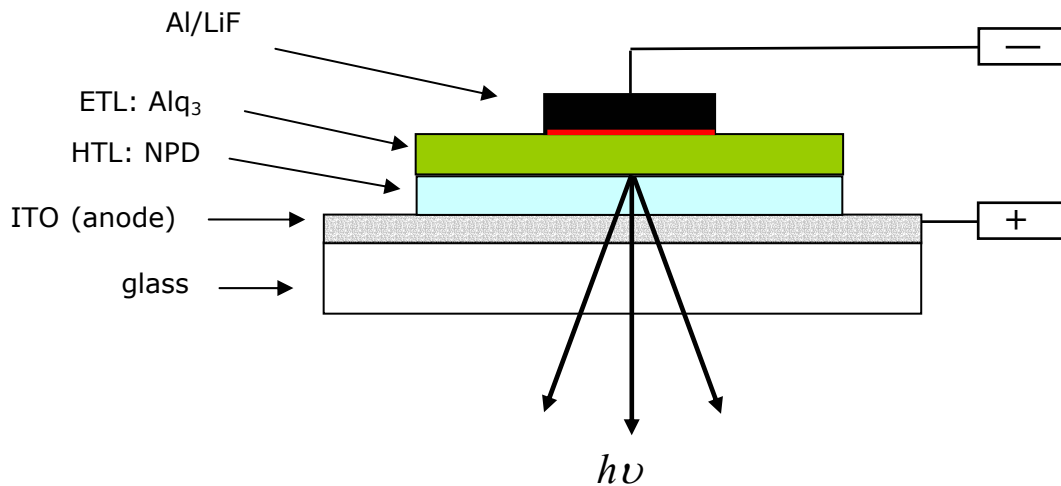
Figure 3.5. Schematic configuration of the two layer OLED considered in this work. The emissive and electron transport layer (ETL) is Alq_3. The hole transport layer (HTL) is NPD.

3.4 Strong coupled systems

Up until now we have limited our discussions to the weakly coupled regime where the photonic modes are unaltered by the presence of the emitter and emission takes place into these modes. A practical manifestation of a weakly coupled system is the OLED. In such a structure emission occurs into both the fully guided photonic modes of the system and also into 'leaky' partially guided modes which couple light out as useful radiation (see chapter 5). This is known as direct emission.

Weak coupling behaviour partially arises due to relatively weak, broad exciton resonances of the emitters. When the exciton resonance is particularly strong and sharp and the widths of the cavity modes are equally pronounced the exciton and photon modes may interact to form two new 'hybrid' modes. These hybrid modes are called cavity polaritons and their formation is manifested as two peaks in reflectivity/ transmission (for reflectivity measurements see chapter 2, section 2.41) of the structure. This splitting is caused by a light matter interaction called strong coupling and is related to vacuum-field Rabi splitting of atoms seen in the quantum regime,

where the optical properties are changed with the addition of a single photon/atom [*Carmichael et al.* (1989)]. The following outline description of strong coupling in atomic and semiconductor systems follows that of *Rarity and Weisbuch* (1995).

In the atomic regime strong coupling is observed when a long lived atomic state (Rydberg atom) is introduced into a high Q cavity. For a single atom sitting in a cavity, the strength of the interaction, i.e. the energy of the splitting is given by

$$\hbar\Omega_0 = 2dE_0 \tag{3.8}$$

where d is the electric dipole matrix element and E_0 is the electric field per photon and is given by

$$E_0 = \sqrt{\frac{\hbar\omega_{cav}}{\varepsilon_0 V_{cav}}} . \tag{3.9}$$

Here ω_{cav} is the frequency of the cavity and V_{cav} is the volume of the cavity, thus

$$\Omega_0 = 2d\sqrt{\frac{\omega_{cav}}{\hbar\varepsilon_0 V_{cav}}} . \tag{3.10}$$

In order for the cavity to undergo Rabi oscillations, both the atom and the cavity resonance must be sufficiently narrow i.e. both the linewidth of the atomic transition $\hbar\Gamma_{at}$ and the line width of the cavity $\hbar\Delta\omega$ must be very small such that

$$\Omega^2 > \frac{\left(\Gamma_{at}^2 + \Delta\omega^2\right)}{2} \tag{3.11}$$

A narrow cavity line width can be achieved by employing high Q structures (Eq 3.3). Also required is that V_{cav} be small, which suggests the use of microcavities. When swapping of energy between the cavity and the atom is driven by an external electromagnetic field the Rabi oscillation frequency becomes larger and is given by

$$\Omega_n = \Omega_0\sqrt{n+1} \tag{3.12}$$

where n is the number of cavity photons. It is clear that even without a driving field (n=0) splitting still occurs and this is known as vacuum Rabi splitting. The presence of many atoms leads to larger co-operative effects and under such circumstances the frequency is

$$\Omega = \overline{\Omega}_0 \sqrt{N} \qquad\qquad (3.13)$$

N is the number of atoms and $\overline{\Omega}_0$ is the average single photon Rabi frequency [*Zhu et al.* (1990)]. This dependence of the Rabi frequency on the number of atoms makes multi-emitter Rabi splitting relatively easy to observe.

Having considered Rabi splitting in the atomic regime we can now consider semiconductor systems. The exciton oscillator strength and the amplitude of the cavity field at the oscillator position determine the coupling. This is again characterised by the vacuum Rabi splitting which for emitters placed close to the electric field antinodes is given by [*Skolnick et al.* (1998)]

$$\hbar\Omega_i \approx 2\hbar \left(\frac{2\Gamma_0 c}{nL} \right)^{\frac{1}{2}} \sqrt{N_{ex}} . \qquad\qquad (3.14)$$

N_{ex} is the number of oscillators in the cavity, L is the effective length of the cavity, n is the refractive index of the cavity and $\hbar\Gamma_0$ is the radiative width of a free exciton. The latter can be expressed in terms of the of the exciton oscillator strength per unit area f_{ex}, which means the cavity-polariton splitting may be expressed as

$$\Omega \propto \sqrt{\frac{f_{ex} N_{ex}}{n_{cavity} L_{cavity}}} . \qquad\qquad (3.15)$$

As already indicated, in the strong coupling regime, where the Rabi splitting is greater than the widths of the radiative exciton emission and of the cavity mode, a measurable splitting in the optical spectrum where two modes anti-cross is observed. Two spectral features due to the mixed exciton-polariton modes are observed. These modes arise from symmetric and asymmetric combinations of the exciton-polariton modes. Only the cavity mode couples to external photons so that away from resonance the predominantly excitonic feature becomes weak when measured in emission. Figure 3.7 shows a schematic of the splitting in the dispersion of the photonic modes of a planar microcavity. The dotted lines indicate the positions of the

unperturbed cavity and excitonic modes. Optical methods for measuring the splitting in the dispersion are discussed in chapter 6.
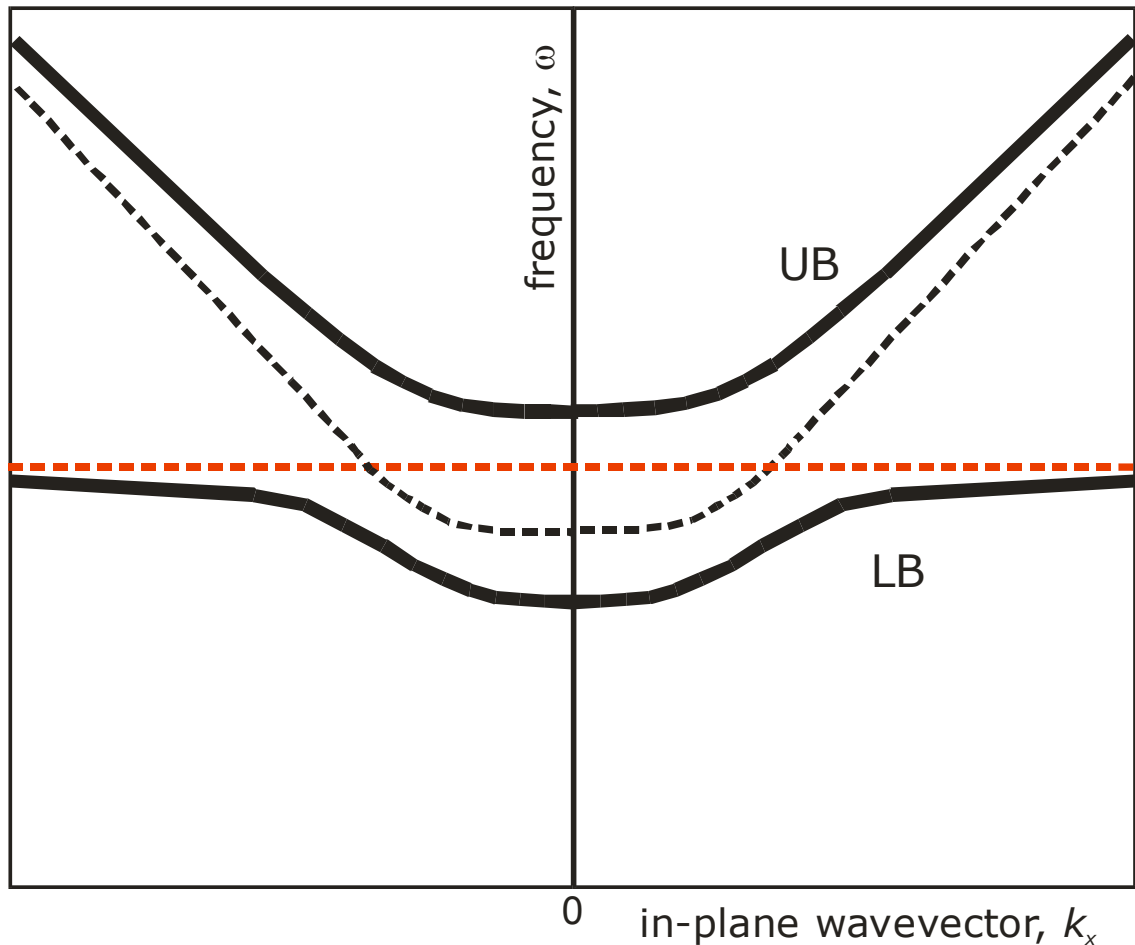
Figure 3.7. Polariton dispersion (solid lines) curves and corresponding non-interacting exciton and photon dispersion (dashed lines, of which that of the exciton is the flat line). UB and LB indicate upper and lower polariton bands respectively.

We shall not discuss the theoretical evaluation of strong coupling any further beyond saying that a simple model treating the cavity and photon modes as coupled oscillators may capture most of the essential physics of the cavity polaritons and has the advantage of being simple enough to solve analytically. The various parameters can be obtained from fitting to the observed data as may be seen in chapter 6. Parameters may be described from a quantum mechanical point of view but there is very little difference from the classical oscillator description. The underlying reason for this is that the

polariton resonance effect, at the heart of strong coupling, is basically a coupling between harmonic oscillators which have very similar behaviour whether considered from either standpoint. The physics behind either of the complementary approaches has been laid out in general reviews of the field e.g. *Khitrova et al.* (1999) and *Skolnick et al.* (1998).

The majority of research in strong coupling has been conducted with inorganic systems. A detailed analysis has been carried out on the manifestation of light-matter interactions in the non-linear optics of semiconductor quantum well structures grown in high-Q Fabry-Pérot etalons such as that of *Houdré et al.* (1994). Current studies benefit from high-Q Fabry-Pérot microcavities that make use of the same fabrication technology used to make vertical-cavity surface-emitting lasers (VCSELs) and RCLEDs.

3.41 Strong coupling in organic semiconductor systems

Up until quite recently [*Lidzey et al.* (1998)] strong coupling in semiconductor microcavities has been limited to the purely inorganic regime. For instance Rabi splittings for III-V (GaAs) based microcavity structures, of ~9 meV at room temperature have been measured [*Nelson et al.* (1996)]. Although organic semiconductors are characterised by considerably larger oscillator strengths (~ 10 times stronger) than inorganic material, promising significantly larger splittings, they generally have broad radiative linewidths which as already mentioned precludes strong coupling. Several candidate molecular materials have been identified with sufficiently small exciton linewidths resulting in so called 'giant' Rabi splitting typically of more than 100 meV. The advantages of using organic semiconductors to study strong coupling are numerous. Recalling Eq. 3.15. we note that along with the greater oscillator strengths, the

relatively low refractive index of organic materials increases the polariton splitting (chapter 6).

One of the organic materials which exhibit strong coupling behaviour is an aggregated form of cyanine molecules. Aggregation arises due to the high concentration of molecules in films, two or more molecules interact sufficiently so that their electronic wavefunctions are delocalised over all of them in both ground and excited states. One such aggregate formation is known as the J-aggregate (as opposed to dimer and H-aggregates). *Jelley* (1936) first noticed J-aggregate behaviour when an unusually sharp absorption band in the visible spectrum of some cyanine dyes was observed at high dye concentrations. This so-called J-band occurs at longer wavelengths than the absorption of molecules at low concentrations and the absorption width is often narrower by an order of magnitude. The appearance of the J-band has been attributed to the formation of molecular aggregates whose electronic transitions are strongly coupled by excitonic interaction. It is strong coupling in this type of system that we explore in chapter 6.

3.5 Summary

In this chapter we have seen that in the weak coupling (perturbative) regime, the optical environment may still have a considerable effect on the spontaneous emission of molecules. The emission rate and spatial distribution of a system may be altered by changes in the local photonic mode density. In this context organic light emitting diodes (OLEDs) were introduced, as were the excited states of molecules in organic semiconductors.

The strong interaction between light and matter was then discussed in which the microcavity is filled with special emitters possessing large oscillator strengths and narrow absorption and emission spectra. The interaction between cavity modes and the

emitters alters the energy levels of the material, resulting in a splitting of the polariton mode.

In the next chapter we examine the various methods employed in fabricating metal-clad microcavities and OLED devices, including the holographic mechanisms for making wavelength and sub-wavelength periodic diffraction gratings used in textured OLEDs (chapter 5).

Chapter 4

Manufacture of nano-textured OLEDs and planar metal-clad microcavities

4.1 Introduction

In this chapter we describe the experimental methods used for the fabrication of nano-textured OLEDs measured in chapter 5. Also discussed are the experimental techniques for making the planar metal-clad microcavities used to investigate strong coupling as detailed in chapter 6. This chapter also contains descriptions of surface profile analysis by atomic force microscopy and details of the operation and degradation routes of the OLED.

This chapter is split into two, the first part of the chapter deals with the complex process of making a prototype OLED incorporating nanostructure. Briefly the process is as follows; beginning with substrate preparation an initial lithographic process is used to form a diffraction grating in a photoresist layer using an interferometer. Following this, the corrugation is transferred into the glass substrate via a process known as reactive ion etching (RIE). The corrugated substrate is subsequently coated with the semi transparent conducting material indium tin oxide (ITO). The ITO surface profile is characterised by an atomic force microscope (AFM) and a mathematical function fitted to it, thus allowing accurate modelling of the photonic modes of the structure (see chapter 2 section 2.5 and chapter 5) and derivation of the optical properties of the ITO. Following this the ITO etched was etched into a stripe in a further lithographic step before the organic layers and metallic cathode were deposited in a high vacuum deposition system.

The second part of the chapter describes the process for manufacturing the organic, planar, metal-clad microcavities. This

includes the deposition of silver mirrors and the formation of thin stable films of aggregated cyanine dye [*chapter 3, chapter 6*].

4.2 Fabrication of textured substrates

In chapter 5 the pitch or wavelength of the grating required to scatter the previously trapped SPP and guided modes back out to light is calculated. For a peak Alq_3 emission wavelength of ~530 nm a sub-wavelength grating pitch of ~290 nm (3.45 μm^{-1}) is required. The grating in each layer of the OLED is provided by corrugation of the glass substrate prior to the deposition of the layers of the device. To corrugate the substrate the profile is first formed in a film of photoresist and then transferred to the glass substrate by an etching process. A 'positive' photoresist is used for the photolithography. This means that areas exposed to an adequate intensity at an adequate optical frequency (blue light) will undergo a chemical reaction that will dissolve under the action of suitable alkaline developer. The greater the intensity of incident light, the more rapid the dissolution in the developer resulting in a physical representation of the light intensity across the photoresist film.

The photoresist is deposited on clean silica substrate by a process of spin coating. Prior to this the substrate, an approximately 25mm square and 1mm thick silica plate, needs to be cleaned of all grease and dust. Cleaning commences by submerging the substrates in concentrated nitric acid for not less than 30 min, after which samples are washed in ultra-pure de-ionised water (DIW). Once dry, substrates are scrubbed with cotton wool buds dipped in acetone to remove any contaminants still stuck to the surface. Subsequently one side is painted black with ebonite paint. This prevents reflections from the back face of the sample during exposure to the interference pattern used to form the diffraction grating.

Once the paint has dried, the front of the substrate can be re-cleaned with acetone and cotton buds, then 'drag cleaned' with iso-

propan-1-2-diol (IPA) and an absorbent lens cloth. Drag cleaning works by dipping the end edge of a lens cloth into propanol and, using tweezers, dragging the wet edge of the cloth across the substrate surface. The wet cloth adheres to the surface and, as it moves across, all dust is removed. The substrate is now ready for photoresist deposition.

Spin deposition of photoresist takes place in a purpose built clean room. Micron-sized particle of dust would severely disrupt the uniformity of the film, which is generally ~400 nm thick, so a clean room environment is necessary. The clean room integrity is maintained by pumping filtered air into the room, thus creating a positive pressure and preventing dust entering from outside. Clean room users are also required to follow stringent guidelines to keep the rooms as clean as possible. This includes the wearing of dedicated clean-room suits, hats, gloves and masks. The suiting-up procedure is also regulated to further reduce the chance of contamination. The clean rooms have filtered lighting to prevent accidental exposure of the photoresist to blue optical frequencies during film manufacture.

Whatever dust may have been left on the substrate is removed using an inert gas spray immediately prior to spinning. The sample is then placed on a vacuum chuck and a few drops of photoresist (Shipley SPR 700-1.2 and EC solvent) deposited on the substrate. The spinner is switched on, and spin velocity, duration and acceleration are all controlled by digital controller. The sample is spun at approximately 4000 rpm for 40 seconds. Once the spin deposition is complete the sample is placed in a light tight box and baked in an oven at 95°C for 30 min. This mild baking drives out remaining solvents from the film, hardening the layer and improving its adhesion to the substrate.

4.21 The interferometer

The photoresist is exposed to an interference pattern generated by a two-beam interferometer [*Hutley* (1982)]. Other methods of generating wavelength scale patterns include embossing or stamping [*Paul et al.* (1998)] and e-beam lithography [*Moll et al.* (2002)]. The main features of the interferometer are shown in figure 4.1. The Argon ion (Ar$^+$) laser has a tuneable output with several available wavelengths to choose from. The wavelength closest to the maximum absorption of photoresist is 457.9 nm.
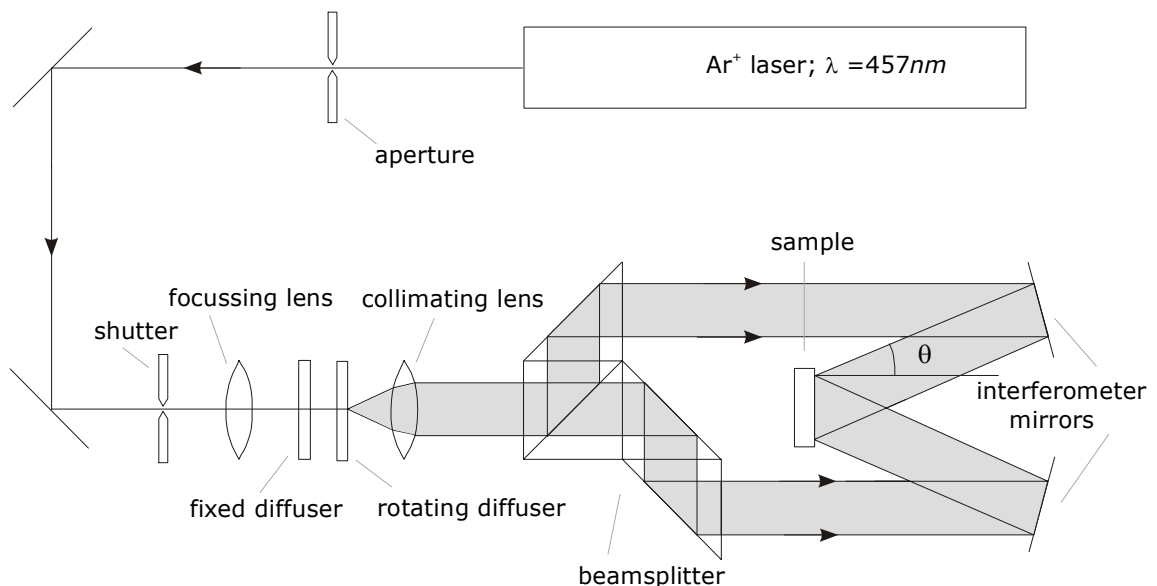
Figure 4.1. Schematic of the interferometer. [*Andrew* (1998)].

The laser output was collimated and expanded using two lenses. The second lens has a longer focal length than the first, thus expanding the beam. Along with the collimating optics there are two diffusers, one stationary and one rotating. The stationary diffuser acts to destroy the spatial coherence of the beam across its diameter. This diffuser is placed close to the focal point of the first lens and also gives a more even intensity cross section to the beam, helping to ensure constant exposure intensity across the sample. The stationary

diffuser also prevents any dust particles moving through the beam from forming any interference pattern. The second diffuser is placed at the focal point of the first lens and rotated. The rotation introduces a time variance into the speckle pattern, which serves to wash out any ring interference patterns that may form from the optics. Without the diffusers the interferometer would have to be operated in an ultra-clean environment to ensure that even single specks of dust could not interfere with the procedure.

In the present study, the expanded beam was passed through the arrangement of 5 silica prisms shown in figure 4.1. The centre of the arrangement is a 50/50 beam splitter. The beam splitter was manufactured by depositing a thin layer of aluminium on the hypotenuse of the first prism. This prism was then index matched with silica matching oil to the second prism. The use of matching oil eliminates spurious reflections and increases transmission. The other prisms serve to realign the output beams of the beam splitter so they run parallel down the bench. These prisms are also index matched to the beam splitter and each other. The parallel beams strike the faces of two aluminium coated silica discs, which act as mirrors. Both mirrors are flat to $\lambda/10$ and each is fully adjustable, allowing precise steering of the beam. This arrangement ensured that each beam, although not having identical path lengths, underwent the same number of reflections throughout the system. This means that a spot in the beam would, after splitting into two parts, accurately recombine when incident on the photoresist layer and provide an interference pattern with no DC offset.

By adjusting the distance of the sample from the mirrors the pitch of the grating formed by the interference pattern changes. Moving the sample in relation to the mirrors adjusts the angle of incidence of the beam and hence the in-plane momentum of the incident light. The geometric relationship of the grating pitch to the angle of incidence makes the manufacture of gratings at a required

pitch theoretically straightforward. The following expression relates the grating pitch to the angle of incidence

$$\frac{\lambda_0}{2\sin\theta} = \lambda_g \qquad\qquad (4.1)$$

where $\lambda_0 = 457.9nm$, λ_g is the wavelength of the required pitch and θ is the angle of incidence. It can be seen from Eq. 4.1 that there exists a minimum achievable pitch corresponding to $\sin\theta = 1$ or $\lambda_g = 229nm$. There are no constraints on the upper limit of the pitch other than the practicality of positioning mirrors several meters away from the sample.

After interferometer alignment, the sample was placed in a special clamp that securely holds it in position. An electronic timer connected to a mechanical shutter controlled the duration of exposure to the interference pattern. Grating depth and quality are strongly dependent on exposure time with over-exposure 'burning' holes through the photoresist.

Another factor affecting exposure time was the grating pitch required. The reflectivities of surfaces are strongly angle dependent with reflectivity increasing as incident light approaches grazing incidence. These two factors coupled with the fact that development is strongly dependent on both concentration and temperature means that grating manufacture is an iterative process requiring many trial samples to be made before satisfactory results are achieved. Typical exposure times for the gratings fabricated was 5 min.

Development was achieved by submersion of the sample in a dish of sodium hydroxide solution. A rapid submersion was necessary to ensure even development across the sample surface. Development times were approximately 5 s, after which the sample was quickly transferred to a dish of DIW, thus rapidly quenching the reaction. The sample was then dried with an inert gas jet. The pitch of the grating could immediately be checked by measurement of the Littrow angle of the diffracted order [*Pedrotti and Pedrotti* (1993)].

4.22 Reactive ion etching

Photoresist is a polymer with relatively low mechanical strength. The hardness of photoresist gratings may be improved with further baking at high temperatures (~180 °C) interspersed with periods of intense UV irradiation. Unfortunately this adversely effects the optical properties of the material. Also, even after baking, a grating is not particularly robust and is susceptible to chemical attack. Photoresist is an efficient absorber of the blue [*Salt and Barnes* (1999)] and after further baking changes colour from a pale red to a deep red. As a transmitting layer in prototype OLEDs and optical microcavities, photoresist is a poor choice [*Lupton et al.* (2000)]. Transferring the grating profile into the silica substrate, which is chemically inert and mechanically robust, makes permanent and optically better gratings. This may be achieved by etching.

In contrast to physical sputtering, RIE operates by the chemical reaction of gaseous compounds formed from a plasma discharge with the solid surface to be etched. The RIE reactor is essentially an adaptation of a sputtering rig. The system operates at a pressure of ~40 mtorr. With the sample placed on a non-grounded electrode (see figure 4.2).
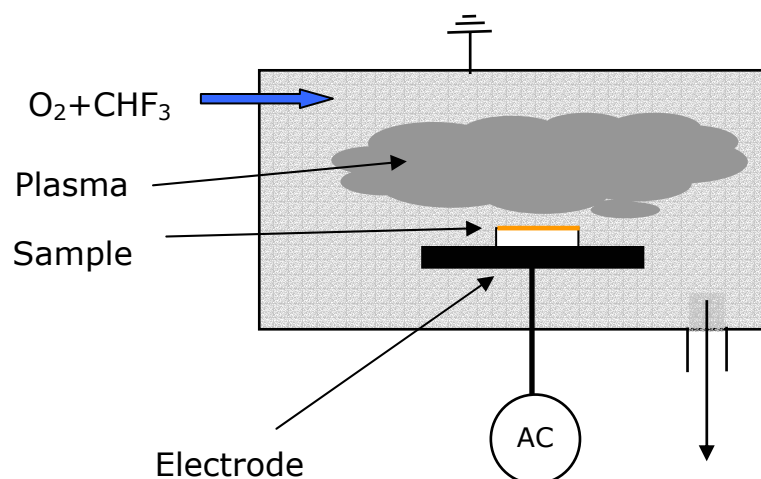
Figure 4.2. Schematic of the reactive ion etcher. RF frequency is ~14 MHz with a DC bias of ~-500V.

The etching of silica and photoresist is commonly achieved with fluorine based gases and oxygen respectively. The fluorine gas derivative employed during this work was CHF_3 (trifluromethane). The purpose of the glow discharge is to convert the molecular fluorine and oxygen that at room temperature do not attack photoresist or silica, into active ions that will readily react. This creation of reactive ionic species is achieved via electron bombardment. The rate of etch is controlled by pressure of the gasses within the chamber and by altering the partial pressures of the gases. With this, differential etch rates of the silica and photoresist may be obtained. The gratings made in the course of this work were generally etched in a CHF_3 to O_2 ratio of 8:1.25. This results in an approximately 1:1 silica:photoresist etch rate. Etch duration was approximately 10 min in duration and the RF power was approximately 180 W.

4.3 OLED manufacture

After the photoresist grating had been etched into the substrates, the first layer of the OLED could be deposited. This was a layer of semi transparent anode material ITO. ITO evaporation requires specialised equipment. Avimo Thin Films Ltd (UK) kindly deposited the ITO using a Leybold 1104 APS (advanced plasma source) plant in which the ITO was electron-beam evaporated The finished films had a resistance of approximately 25 $\Omega/\square$ (sheet resistance, ohms per square). A series of planar control and corrugated substrates of 290 nm were coated with ~356 nm of ITO.

Following ITO deposition the grating profile was analysed with an atomic force microscope. This allowed the grating profile to be accurately determined, a vital step that allowed accurate numerical modelling of the dispersion of the ITO layer and consequently the rest of the device. In the AFM, a sharp tip is attached to a cantilever. The tip is forced to oscillate at its resonant frequency. As the atoms in the tip interact with the electrostatic fields of the surface atoms of the

sample, the oscillating tip is effectively mass loaded and the frequency of oscillation drops. The frequency of the tip is measured by laser illumination which when detected is fed into a feedback controller which regulates the force between the sample and the tip by moving the sample up or down. A piezoelectric scanner moves the sample.

Deposition of the organic and metals layers on OLED devices took place at the QinetiQ labs based at Malvern (UK) using the purpose built OLED deposition system based there. Dr. I. Sage of QinetiQ and the author deposited device layers. The author is indebted to Dr. I. Sage for his invaluable contribution. During the course of this work several methods for fabricating OLEDs have been tried. Initially, the metal contacts were circular pads evaporated through a mask on top of the device. Electrical connection was achieved by pushing a wire against the pad. Maintaining such a precarious mechanical connection whilst taking angle dependent measurements proved to be impractical as the slightest movement often pushed the wire through the metal contact and shorted out the device or else the wire lifted off and broke the contact. Conductive adhesives such a silver dag promised to be a solution to the problem, but the solvent in the glue attacked the organic layers and destroyed the device. Consequently a more complicated system of mask and etching was adopted, allowing electrical contact to be made via a conducting adhesive on the substrate. Figure 4.3 shows the OLED fabrication steps beginning with an ITO coated substrate.

ITO

a) etch ITO

b) deposition of insulating polymer

Al/LiF

Organics

ITO

c) deposit organics and metals
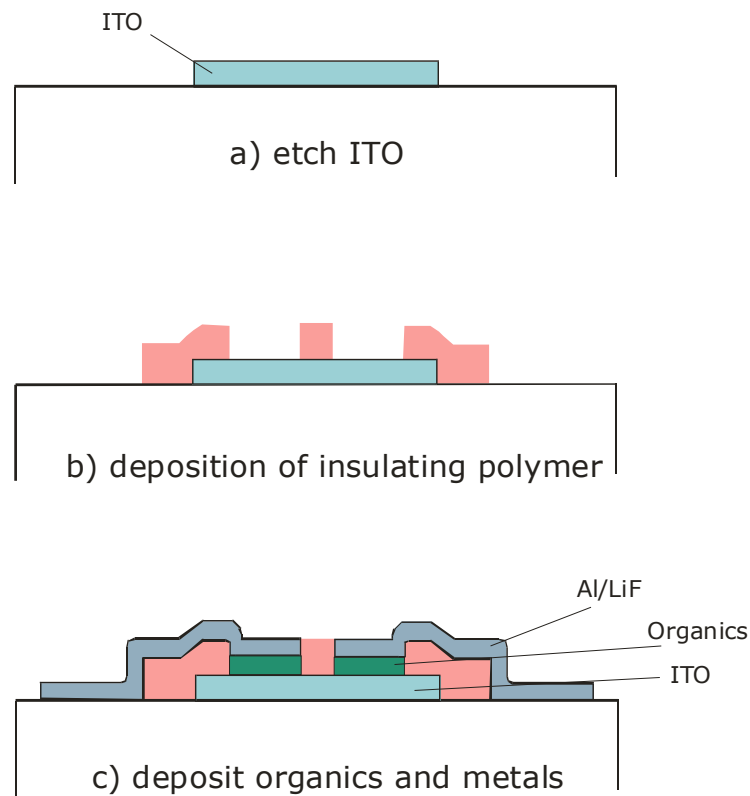
Figure 4.3. Manufacture steps of encapsulated OLED devices.

Initially the ITO is simply masked and etched. This results in a stripe of ITO down the centre of the substrate thus allowing adhesive electrical contacts to the cathode to be made on the substrate away from the ITO and organic layers. The second step entails the deposition of an insulating layer of polyamide (PI) (JSR BRP107LL from Japan Synthetic Rubber). This polymer layer prevents the metal cathode layer shorting out against the edge of the ITO and also provides a degree of encapsulation and hence protection against moisture in the atmosphere. This layer was initially spin cast and then exposed to UV radiation through a specially designed mask. Upon development the appropriate design remains. Finally the organic layers and metals were deposited in a purpose built evaporator. By depositing both organic and cathode layers together in one purpose built evaporator the entire device could be deposited in one go without exposure to the atmosphere. This improves device lifetime

and stability. Both Alq$_3$ and NPD layers were deposited at a rate of 4 Å/s. In initial samples 50 nm of both NPD and Alq$_3$ were deposited. Subsequent devices employed 68 nm of Alq$_3$ and 38 nm of NDP. All devices used cathode layers consisting of LiF 5 Å and Al ~150 nm. The evaporation system used for deposition of both the organic and metal layer was a Kurt J. Lesker Company (KJLC) Spectros OLED deposition system. A schematic of the main features of the system is shown in figure 4.3
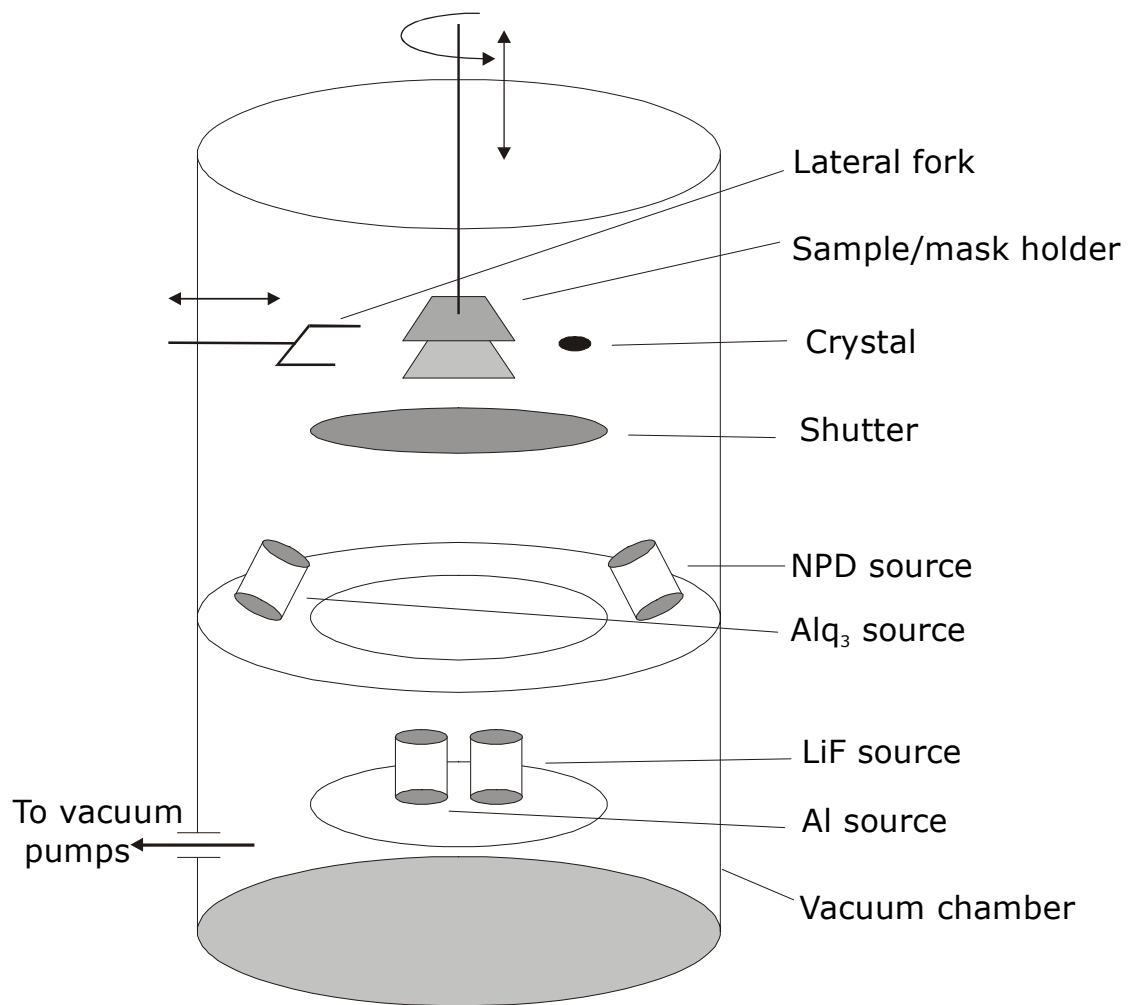
Figure 4.4. Schematic of the multiple source UHV deposition systems used to deposit manufacture the OLEDs in this work

KJLC's Spectros is a research and development system designed specifically to investigate the deposition methods and characteristics of emissive films used to make OLEDs. The deposition chamber is an ~0.5m diameter x ~1m tall cylinder made from

stainless steel. Substrates are changed and sources replenished through a tall, flat O-ring sealed door. The substrate holder consists of a series of plates rotating about a central rod and may hold substrates and masks stacked on different levels. Vertical motion is achieved using a manual rack and pinion. A horizontal linear translator allows mask/ substrate changes. Eight organic layer sources and three thermal evaporation boat sources can be accommodated in the chamber. The OLED sources are designed for low temperature evaporation and are composed of a ceramic container surrounded by a coil of wire to provide resistive heating.

4.4 Device operation and degradation

Connections to the device were made by soldering a wire with indium solder onto an exposed area of ITO and sticking fine gold thread to the aluminium contact using the conductive adhesive silver DAG. Because the aluminium contact was only ~150 nm thick every care was taken not to damage the device, hence the use of fine gold thread. With relatively permanent and robust contacts made to the device, angle dependent measurements of electroluminescence could be made. The experimental set-up for such measurements is essentially identical to that for the photoluminescence (chapter 5 figure 5.9). Essentially the device needs robust connections that may withstand both angular and azimuthal rotation.

One of the necessary prerequisites of a modern LED is that it provides high luminescence for a small input power. This places certain restraints on the output of potential power supplies. Consequently a simple constant current source was constructed in the electrical workshop in Exeter to power the devices. Controlled by a 10 turn potentiometer this device when placed across the driving power supply allowed the input current to the device to be controlled with mA sensitivity. Generally devices were driven ~10 mA (± 1 mA) and drew ~10V.

Once under operation the typical lifetime of a device was approximately 60 min during which time luminescence gradually faded. In our observations both planar and corrugated devices suffered from such short lifetimes. There have been many studies of the degradation mechanisms in small molecule based OLED devices. Different strategies for improving OLED stability have been suggested [*Popovic and Aziz* (2002)] however most previous workers have experienced luminescence half-lives in excess of 50 hours. The shorter lifetimes of the devices fabricated in the course of this work show that the problems are more severe.

Upon operation degradation progressed through a visually distinct route and was due to the filing of the aluminium cathodes. Seconds after device turn on bubbles were seen to form on the device electrode and luminescence, rather than coming uniformly from all over the device, appeared speckled. Figure 4.5 shows a low magnification microscope picture of the edges of two neighbouring electrodes.
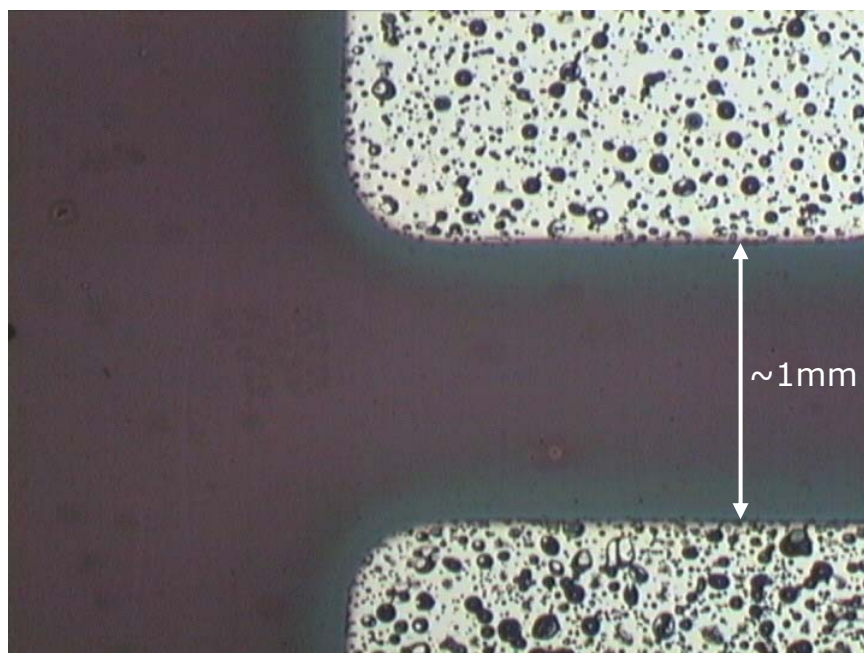
Figure 4.5. Low magnification microscope image taken of the edges of two neighbouring OLEDs under white light illumination. The aluminium cathode appears white in reflection and the features appear black.

Small irregularly shaped dark marks are much in evidence all over the sample. To the naked eye this gives the previously mirror-like electrode a matt sheen. Higher magnification (figure 4.6) reveals that many of the features are elevated cathode bubbles that appear dome like. Other formations with darker centres are also clear as are some small black spots.
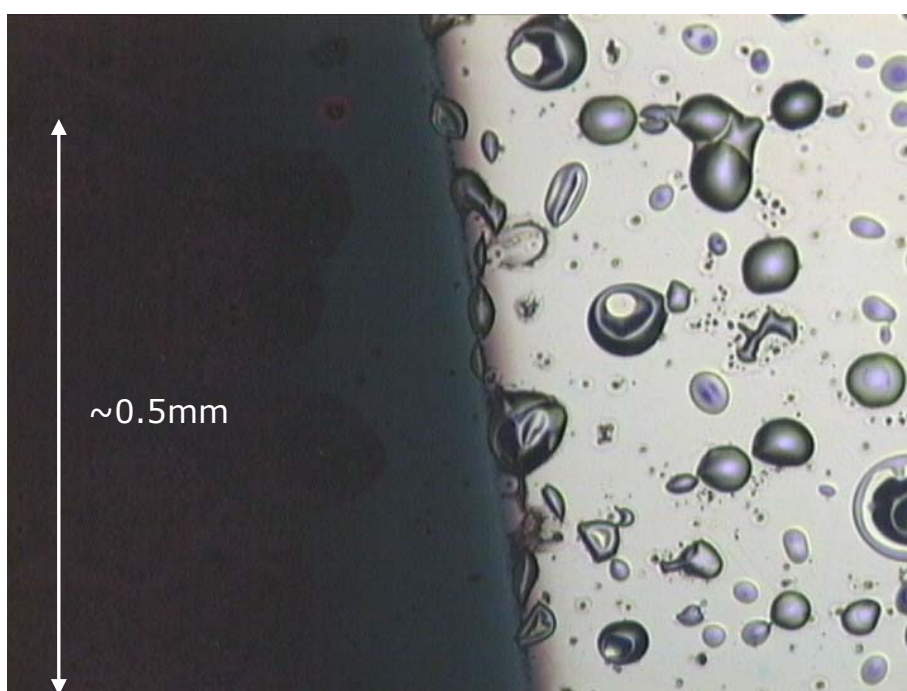
Figure 4.6. Higher magnification microscope image taken of the edges of an OLED cathode under white light illumination. The features can clearly be seen to be bubbles.

Recently many workers [*Kolosov et al.* (2001), *Liew et al.* (2000), *Aziz et al.* (1998)] have looked at degradation processes in Alq$_3$ based OLEDs and have proposed various models to support their observations. However, none of the recent studies have looked at degradation in Al/LiF cathode devices, dealing exclusively with magnesium silver alloy cathodes. This is possibly a matter that should be addressed if Al/LiF becomes the most prevalent cathode material in OLED devices. Never the less many of the observations on Mg:Ag cathode systems are similar to those seen during this work. Therefore we may conclude that similar process are involved. The growth of

elevated cathode spots or bubbles, which may lead to the formation of non-emissive spots was found to be caused by gas evolution from the electrolysis of absorbed moisture. These bubbles only develop during device bias and are enhanced by humidity. This process leads to failure by cathode de-lamination from the underlying organic layers and causes non-emissive spots [*Aziz et al.* (1998)].

Prior to full operation, devices were exposed to ambient atmosphere on several occasions. Post-deposition of the organic and metal layers of devices they were transferred to a glove box containing an inert atmosphere. However the glove box was not an extension of the deposition chamber so the samples would for a short time come into contact with air and moisture. For operation and measurements devices were transported from Malvern to Exeter in a desiccater jar containing dehydrated silica gel to keep the atmosphere dry. Storage prior to measurement in Exeter was also in a desiccater in which air had been replaced with nitrogen. This served as a simple glove box. Measurements of devices under operation were conducted with a flow of nitrogen blowing across the sample as an extra protection against the atmosphere.

Another mechanism for the formation of dark spots may be due to cathode defects. After operation, devices were examined under a transmission microscope and small pinholes in the cathode were noted. These defects have been observed in other systems and workers have suggested that the defects are created during the deposition of the cathode and are not the result of pre-existing defects in the underlying organic layers [*Liew et al.* (2000)]. Such defects would act as routes for moisture to enter the device.

In light of the above, it is not particularly surprising that the devices operated for only a short period of time and suggest that the partial encapsulation provided by the polyamide insulating layer prevented moisture completely destroying the device. We can conclude that the only way to protect an OLED device from dark spot formation is to manufacture and operate the device in a completely

inert atmosphere. Long lifetimes for prototype OLED devices may only be realised with either complete encapsulation of the device during its manufacture under vacuum or the adoption of sophisticated sealed chambers within which measurements may be conducted in an inert atmosphere. Naturally the latter approach is impractical for realistic devices in practical display applications.

Up until now this chapter has dealt with the experimental details of manufacturing and operating the OLED devices measured in chapter 5. The work in chapter 6 details optical experiments in the strong coupling regime. The samples used in that work were metal clad microcavity structures. The remainder of this chapter details the manufacture of these structures.

4.5 Planar metal-clad microcavity

The planar microcavities used in the strong coupling work consisted of a thin, stable film of J-aggregates dispersed in polyvinyl alcohol (PVA) bounded on top and bottom by optically thin silver mirrors. A schematic of the microcavity is shown in figure 4.7. The bottom mirror was deposited directly onto the bare, clean silica substrate and the top mirror was deposited on top of the J-aggregate film.
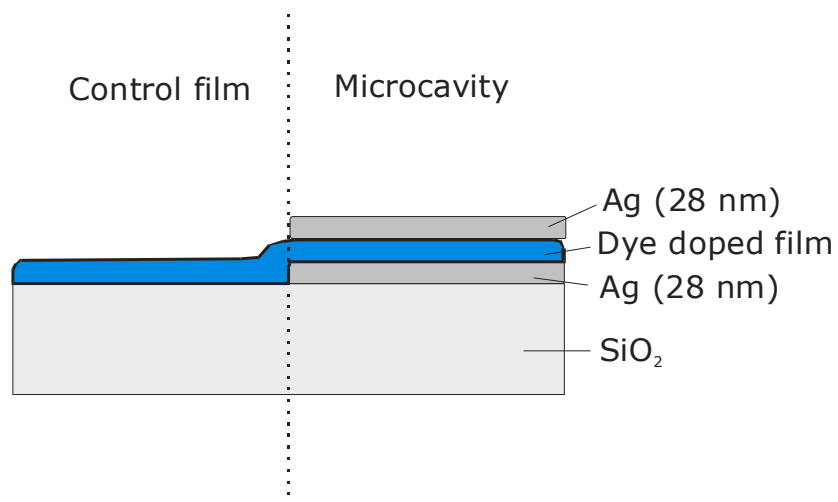
Figure 4.7. Schematic of the microcavity samples fabricated.

As in previous cases the building block of the device is a silica glass substrate. As for the deposition of photoresist, the silica substrates need to be methodically cleaned of not only micron sized dust particles, which would severely disturb wavelength scale thin films of organic and metals but any grease contaminants from oil deposited from fingers. Oil and grease areas would locally alter the optical characteristics of the device and perhaps prevent film metal adhesion to the glass substrate. This is achieved as above by submerging the substrates in concentrated nitric acid for at least 30 min. The substrate is then washed in DIW. Once dried under a jet of inert gas the substrate was cleaned using the procedure outlined above namely with acetone and cotton wool buds and finally drag cleaned with propanol.

4.51 Deposition of silver mirrors

The mirrors that form the planar microcavities are deposited by a process of thermal evaporation similar to that employed for depositing the cathode metals on the OLED devices. The bottom mirrors were deposited directly onto the clean, bare silica substrates using a vacuum evaporator. The top mirror was formed on the aggregate film. The procedure for depositing both films is identical.

The clean, dust free substrates were placed face down on a sample holder in the evaporator. Each sample was further masked so that only one half of each substrate would be metal coated. This ensured that each substrate, upon deposition of the aggregate film, would consist of a microcavity sample and also a control film sample from which the optical absorption and hence the oscillator strength could be ascertained.

The vacuum chamber was pumped out in two stages, roughing and backing. Roughing took place with a rotary pump and took the chamber down to a pressure of $\sim 1 \times 10^{-3}$ torr. An oil diffusion pump

was then used to further evacuate the chamber down to $\sim 2 \times 10^{-6}$ torr. High purity (99.99%) grains ($\sim$ 2 mm diameter) of silver were used for the evaporation, with one grain placed in a molybdenum boat being essentially a resistive heater. Once a sufficiently low pressure was reached evaporation was achieved by passing a high electrical current through the boat. By varying the current flow the rate of evaporation was controlled. Like OLED deposition, a quartz oscillator placed at the same height as the samples measured the rate of deposition. As material was deposited the resonant frequency of the crystal would shift due to mass loading. The change in frequency was monitored by a calibrated frequency meter which gave the thickness of the silver on the crystal and hence the samples.

4.52 Spin coating J-aggregate films

The optically active layer of the strong coupling devices was composed of a dye-doped layer of PVA and made by Dr D. Lidzey of Sheffield University and the author. This was achieved by dissolving 3 g of PVA in a mixture of water and methanol (60:40 by volume respectively), this mix formed the basic polymer matrix to which the dye was added in varying amounts. Two separate dye concentrations were utilised in the experiments described in chapter 6 to form two distinct oscillator strengths. This was achieved by adding 49 mg or 33 mg of cyanine dye to the basic PVA matrix described above. In each case approximately 1g of PVA was dissolved in 1 cm^3 of the solvent mixture. The chemical structure of the cyanine dye is shown in figure 4.8.
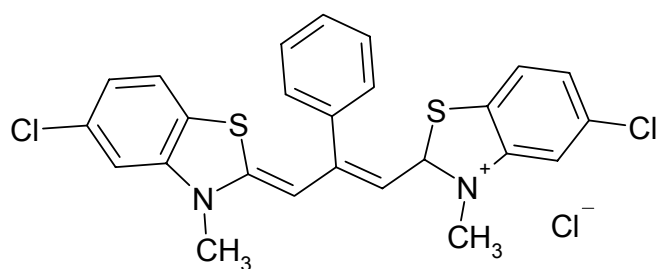
Figure 4.8. Chemical structure of cyanine dye, 2,2'-dimethyl-8-phenyl-5,6,5',6',-dibenzothiacarbocyanine chloride, (NK2535) used to dope PVA films in metal microcavity structures

Dissolving the PVA and dye in the water, methanol mix required the mixture to be heated and vigorously agitated until a homogeneous solution was formed. This was achieved by putting the mixture in a small volumetric flask and alternatively heating on a hot plate and shaking. After 10 min of this treatment a dark purple viscous liquid formed. Film thickness in the range 175-200 nm were deposited on a number of half silvered substrates. This thickness range corresponded to spin speeds between 2.5-8 $\times 10^3$ rpm. The thickness of metal mirrors and dye films was measured by with a Dektak™ surface profiler.

4.6 Summary

In this chapter all of the main experimental techniques used to make the samples studied in chapters 5 and 6 have been outlined. Operation and possible degradation mechanisms in OLEDs have also been discussed. Degradation of OLEDs is of major consideration if the technology is to be incorporated into display applications. For displays it is assumed that a half-life of at least 10000 hours at a luminescence of 100 cd/m^2 is needed [*Popovic and Aziz* (2002)]. We speculated the main cause of device degradation in this work was due to the presence of moisture within the device environment. This

caused the device lifetimes to be very low ~1 hr. The moisture problem may be overcome with better encapsulation of the device.

In the next chapter (chapter 5) the experiments and measurements taken on OLED structures are detailed, with the intention of studying the coupling between emitters and the various photonic modes of the device. The comparatively simple metal-clad microcavity devices with dye doped layers of aggregated cyanine dye are investigated in chapter 6.

Chapter 5

Surface Plasmon Mediated Emission from Nanostructured Light Emitting Diodes

5.1 Introduction

In chapter 3 the modification to spontaneous emission by microcavity effects was introduced. Some years ago *Purcell* (1946) formulated the first theoretical model that can be used to describe weak exciton-photon interactions in a microcavity. Subsequent workers such as *Kleppner* (1981) found that, in the weak coupling regime, the microcavity (by altering the photonic mode density) alters the spontaneous emission lifetime of the exciton, together with the spectral width and spatial distribution of the emitted light.

Light generated by organic light emitting diodes (OLEDs) results from radiative recombination of excitons (see chapter 3) generated by electrical stimulation of organic molecules. These molecules also de-excite by spontaneous emission. Also, the thin dielectric layers and metallic electrode of the OLED constitute a weak optical microcavity, so that we might expect the structure of the OLED to modify the emission of excitons within it.

One of the key goals in OLED research is that of optimising device efficiency. In the past there have been two approaches to this problem. The first approach considers device operation from an internal perspective and strives to increase the efficiency by increasing the fraction of radiative recombination of the charge carriers within the device [*Tang et al.* (1989)]. The second approach considers the optical properties of the device and looks at the coupling out of light from the OLED to useful far field radiation. It is the second of these processes, which is the subject of this current work.

As mentioned above the generic OLED structure constitutes a microcavity and usually comprises a glass substrate, a transparent dielectric anode, one or more emissive dielectric layers and an optically thick metal layer to act as a cathode (See figure 5.1). Consequently much of the emitted radiation will remain trapped in the relatively high index layers of the structure by total internal reflection, forming waveguide modes. The efficiency can be estimated from a simple $1/2n^2$ model, [*Greenham* (1994)] where *n* is the refractive index of the medium. Putting in the corresponding figures for Alq$_3$ at 550 nm near its peak emission, we find *n*=1.74 resulting in an efficiency of ~16%.

Many authors have proposed interesting solutions to increase out coupling and thus improve efficiency. These included the introduction of a low index Silica Aerogel layer [*Tsutsui et al.* (2001)], or scattering out of waveguide modes from either random [*Windisch et al.* (1999)] or periodic nanostructure [*Lupton et al.* (2000)]. Despite these diverse solutions to the out coupling problem, most workers have not considered the lowest order transverse magnetic (TM) waveguide mode, or surface plasmon polariton (SPP) mode. This is rather odd because in small molecule based OLED structures the coupling to the SPP is the dominant decay channel for light and is ubiquitous in all OLED devices using metal cathodes [*Hobson (a) et al.* (2002)]

To maximise OLED extraction efficiency the recouping of all trapped guided modes including the SPP mode is desirable. The work presented in this chapter, reports the first experimental demonstration of a new LED device that couples out light that would otherwise be lost to the SPP and other guided modes. Enhancements to device emission are clear, as are polarisation changes and spectral changes in the emission spectra. For electroluminescent emission in the forward direction we have a doubling of efficiency compared to the planar device and conclude that coupling out of SPP modes alone gives an increase in emission of around 48%. We will begin though

by modelling a generic planar LED to calculate the extent to which radiative excitons couple to SPPs and other guided modes.

5.2 Modelling of planar OLED structures

In planar OLED structures the extent of the loss of light due to coupling to bound modes is not easily perceived from experimental observations as they lie outside of the air light line. To quantify the problem of coupling to SPP and bound modes in OLED systems, (based upon the emitter aluminium tris-8-hydroxyquinoline (Alq_3)), we have therefore undertaken extensive modelling of the device shown in figure 5.1. The nature and number of optical modes in a given structure depends entirely on the physical parameters (dimensions/ optical constants) of the structure under consideration. The strength of coupling between the emitter and the different modes is however dependent upon the position of the emitters within the structure. In an electrically pumped OLED this is dictated by the location at which electrons and holes recombine. Before we examine how the emitter position alters the coupling to the SPP mode we first need to identify the different optical modes associated with our OLED device.

Aluminium

Alq_3 (100 nm)

ITO (100 nm)

Glass

$h\upsilon$
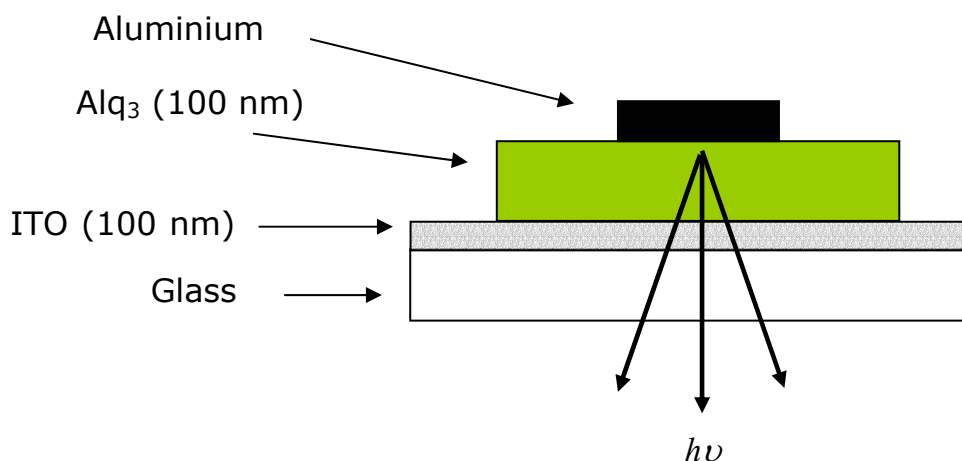
Figure 5.1. Schematic cross section of a generic planar organic light emitting diode considered in modelling this work.

We have calculated the extent to which emission from radiative excitons is lost to surface plasmons and other guided modes [*Hobson a) et al.* (2002), *Hobson b) et al.* (2002)]. We made use of a model established by *Chance et al.* (1978), developed *by Ford and Weber* (1984) and especially adapted by *Wasey and Barnes* (2000) based on considering radiative excitons as classical dipole oscillators. The author is indebted to J. Wasey of Exeter for the majority of the modelling used in this chapter. Using this model we are able to incorporate the effects of material dispersion, absorption and if appropriate, birefringence. The advantage of this technique is that it allows us to calculate the power lost by emitters to the different optical modes of any given planar multilayer structure. We considered an OLED of a generic structure based on silica glass substrates coated with 100 nm of ITO to form the anode. In the calculations it was assumed that organic layers have a thickness of 100 nm, and that they were capped with an aluminium cathode, see figure 5.1. The material parameters used and their wavelength dispersion together with the emission spectra we used to model these devices are given in appendix A.

We calculated the power dissipated by the dipole within the emissive layer as a function of in-plane wavevector to form the power dissipation spectrum at 550 nm (approximately the peak emission for Alq$_3$). This modelling is shown in figure 5.2 (top). It is clear that a significant amount of the emitted light is coupled to guided modes to the right of the silica light line. Coupling to the SPP is seen to be the single most significant decay route for radiative excitons.

We calculated the power lost by the emitter in terms of frequency and in-plane momentum, thus revealing the dispersion diagram for the OLED figure 5.2 (bottom). Here dark corresponds to strong coupling to optical modes. For the dipole emitter placed midway the emissive layer there was strong coupling to the guided modes of the system. These are revealed as a region of high power loss.
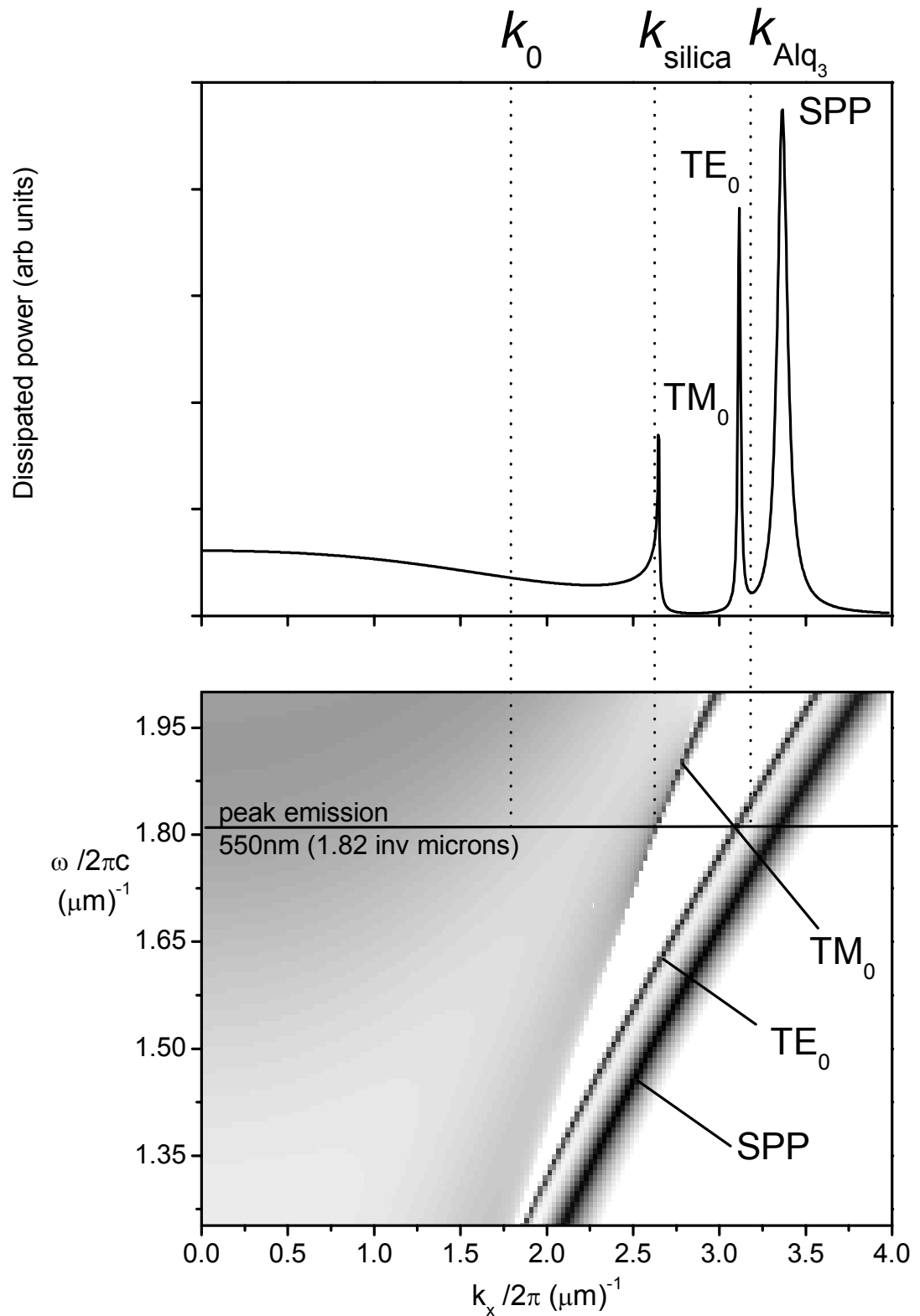
Figure 5.2. Calculated power dissipation spectrum (top) (for the structure in figure 5.1) as a function of frequency and wavevector thus forming a dispersion diagram (bottom). Dark regions correspond to coupling between the emitter and optical mode. Mode designations are indicated, as is the silica light line. Modes to the right of the light line are bound to the structure. Calculation is for emitters placed in the centre of the Alq$_3$ layer. Model by J. Wasey taken from *Hobson a* (2002).

Also indicated on figure 5.2 (b) are the mode identities and the silica light line. Modes to the right of the silica light line are also called 'bound' modes and posses a greater momentum than photons propagating in the air or silica substrate. The continuum of 'leaky' modes is also evident to the left of the light line. These modes are leaky because they may couple to far-field radiation thus contributing to useful emission from the device. The dispersion diagram provides a good qualitative feel for the relative strength of the different modes in the structure. For a more quantitative grasp of the relative strength of the different decay routes we can integrate the area under the peaks. Alq_3 is optically isotropic and the excitons in the Alq_3 system have no preferred orientation so coupling between excitons and SPPs and other modes may be calculated from a weighted mixture of two orthogonal emissive dipole orientations, parallel and perpendicular to the film plane. Figure 5.3 shows how the power coupled to the SPP mode and other decay routes varies with position of emitter within the emissive layer.
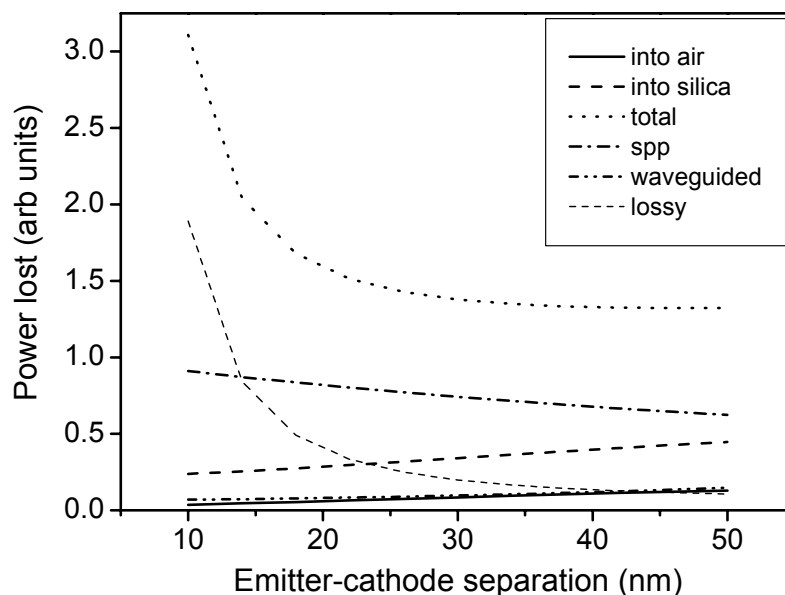
Figure 5.3. The power coupled to different modes of the generic OLED (figure 5.1) as a function of separation between emitter and the Al cathode. Account has been given to the spread in emission wavelengths from Alq_3 by an intrinsic emission spectra [Hobson (a) (2002), appendix A].

It is clear that the SPP mode is the dominant decay route of the system for emitter-cathode separations greater than 15 nm. We may re-express the data in figure 5.3 to indicate the extent to which SPPs alone limit the light output from Alq_3 based OLEDs. The key results from such modelling are given in figure 5.4. The data are presented in the form of the fraction of radiative power coupled to the SPP mode as a function of position of the emitter within the structure. There are two important points to note.
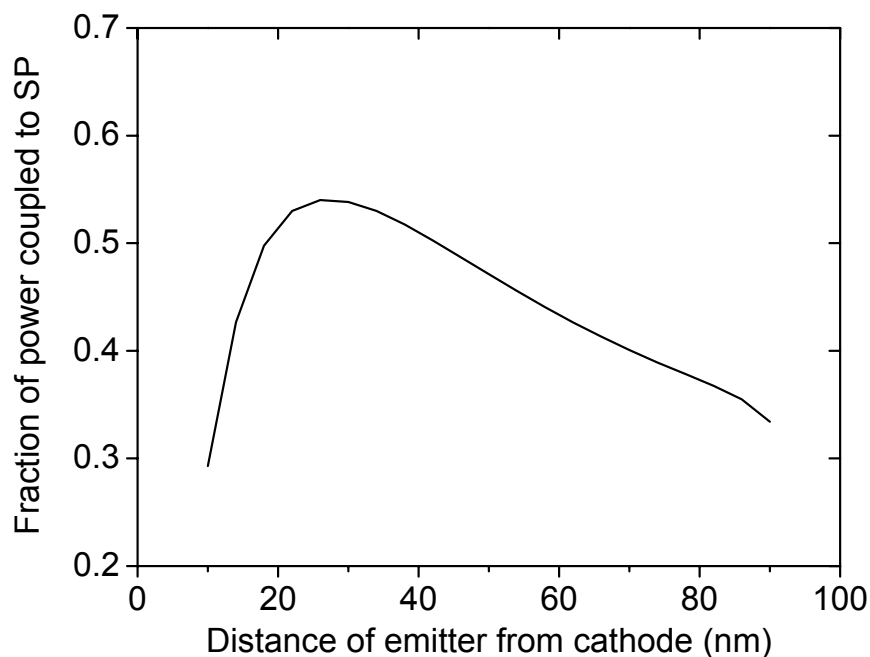
Figure 5.4. Calculation of the fraction of power lost from radiative excitons to surface plasmon modes as a function of position of the exciton within the Alq_3 layer. Modelling by J. Wasey taken from *Hobson (b)* (2002).

Firstly we observe that quenching by SPPs is significant right across the emissive layer. Secondly, the quenching by SPP modes falls off as the distance between the cathode and the exciton drops below 30 nm. At first sight this may seem surprising, but arises because at these small distances coupling of organic excitons to exciton excitations in the metal dominates [*Barnes* (1997)], indicated on figure 5.3 by the lossy mode contribution. These data demonstrate

that coupling to SPP modes is a significant factor in OLED operation. Next we discuss the strategy we adopted for recouping the power lost to the SPP and other guided modes.

5.3 Experimental strategy.

As already intimated by the modelling, to recover power lost to the bound modes of an OLED will require a suitable mechanism to allow out-coupling to far-field radiation. The mechanism implemented in this work for out-coupling of the guided modes was to nano-texture the glass substrate with a periodic Bragg diffraction grating. Subsequent deposition of the device layers on top of this textured substrate allowed the grating profile to be transferred effectively to each layer of the structure.

Guided modes are trapped within the structure in accordance with the law of conservation of momentum, because their in-plane momentum or wave vector is greater than that of light propagating in air. Such modes are often called 'bound' modes as their momentum binds them to the dielectric layer in which they propagate. Modes which can couple to far-field radiation have momentum which falls within the air light line i.e. have in-plane wave vectors less that light propagating in air, these modes are often termed 'leaky'. For a bound mode to become leaky it must suffer a reduction to its momentum. A Bragg grating provides a precisely controlled mechanism for achieving this. The Bragg grating will add or subtract an integer multiple N of the grating momentum k_g from the momentum of the mode k_m so that the mode now lies within the air light-line, (refer to Eq.5.1.)

$$k' = k_m \pm Nk_g \qquad\qquad (5.1)$$

The SPP mode arises due to interaction between electromagnetic radiation and free charges at a metallic surface (chapter 2). Like other bound modes the SPP momentum is greater

than that of light in air and therefore may not couple to far field radiation. Also, because the SPP mode propagates at the dielectric/ metal interface rather than in the bulk dielectric like other guided modes, it may not be suppressed by thinning down the dielectric layer until it is unable to support other guided modes. So only by employing non-metallic cathode materials may coupling to the SPP mode be suppressed, and only by employing a momentum matching mechanism such as a Bragg grating may the SPP mode be recouped.

We can briefly estimate the pitch or wavelength of the grating required to scatter the surface plasmon mode back out to light. The peak Alq$_3$ photoluminescence from a thin film is around 530 nm. At this wavelength the surface plasmon has approximately 1.8 times greater momentum than a photon propagating in air. This can be calculated from the surface plasmon dispersion relation Eq. 2.12. and the material parameters given in appendix A. Rewriting Eq. 5.1 using this information we find

$$k_0 \sin\theta = 1.8 k_0 \pm N k_g.$$

(5.2)

We want ideally, to have the benefits of plasmon emission for normal emission i.e. $\theta = 0$ degrees. This simplifies Eq. 5.2 to

$$1.8 \lambda_g = \lambda_0.$$

(5.3)

At 530 nm this gives a grating pitch requirement of 294 nm. In the next section the experimental realisation of the proposed structure is discussed.

5.4 Device fabrication and characterisation

The OLED system employed in these experiments was based on the small molecule emitter aluminium tris(8-quinolinolate) (Alq$_3$) developed by *Tang and VanSyke* (1987). A hole transport layer of indium tin oxide (ITO) was used along with a hole transport layer of NPD (4,4'-bis(N-(1-naphyl)-N-phenyl-amino) biphenyl). Electron injection was by an aluminium cathode on top of a thin layer of

lithium fluoride (LiF) [*Hung et al.* (2001)]. Planar reference devices as well as the nanostructured OLEDs, were also fabricated so that accurate comparisons between planar and textured systems could be taken. The corrugated device schematic is shown in figure 5.5.
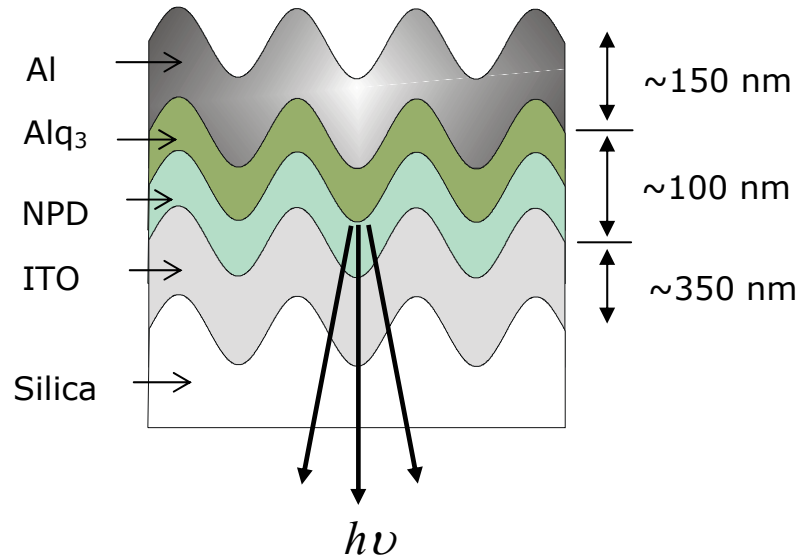
Figure 5.5. Cross section of the OLED structure fabricated for this work. (For the numerical modelling we assumed the hole transport layer, NPD, had similar optical properties to the to Alq$_3$.

The OLEDs were fabricated directly on top of a suitably corrugated substrate. Initially, under clean room conditions, a photoresist layer was spin cast onto a silica substrate. Nanoscale patterning of the photoresist was achieved by an optical interference technique using an argon-ion laser (457.9 nm) followed by chemical development, the full details of which have been discussed in chapter 4. These steps resulted in the formation of diffraction gratings with a pitch λ_g of 290 nm, close to the optimum pitch of 294 nm calculated above. Reactive Ion Etching (RIE) was used to transfer this pattern onto the silica substrates. Etching took place at a pressure of 50 mtorr for 10 minutes. The volatile etch chemicals were formed from a glow discharge plasma of CHF$_3$ and O$_2$ gasses which attack the silica and photoresist respectively. An electrode of ITO with a sheet resistance of approximately 25 $\Omega/\square$ and 356 nm thickness was

deposited by electron beam evaporation ITO deposition was kindly provided by C. Cole at Avimo thin films Ltd. (UK).

Non-contact AFM characterisation images of the ITO surface were taken. Figure 5.6 shows a typical AFM image of the grating; light and dark regions represent high and low features respectively. The mean surface profile $s(x)$ was determined by fitting the function

$$s(x) = a_0 \sin(k_g x) + a_1 \sin(2 k_g x + \phi_1) \qquad (5.4)$$

to the AFM data, giving $a_0 = 15$ nm $a_1 = 1.5$ nm and $\phi_1 = 90^0$. On top of the patterned ITO the hole transport layer (50 nm) and Alq$_3$ layer (50 nm) were deposited by vacuum sublimation. The structure was capped with a cathode comprising of LiF (0.8 nm) and an optically thick layer of Al (150 nm) [*Hung et al.* (2001)].

As will be seen later, the AFM characterisation of the surface profile allowed us to accurately model the Bragg scattered modes of the device. The fact that all layers are deposited using evaporation techniques meant that each interface had almost the same corrugation as the layer below. Long chain polymer based OLEDs devices such as MEH-PPV [*Burroughes et al.* (1990)] are usually deposited by a spin casting, a process that inevitably leads to some planarising of the top surface. In such spin cast polymer systems, over the deposition of several layers, its is probable that the corrugation would be 'washed out' before the metal was deposited, so preventing the Bragg scattering re-radiation of the SPP modes. This has yet to be checked but may have significant consequences for the ultimate efficiency of different types of OLED.
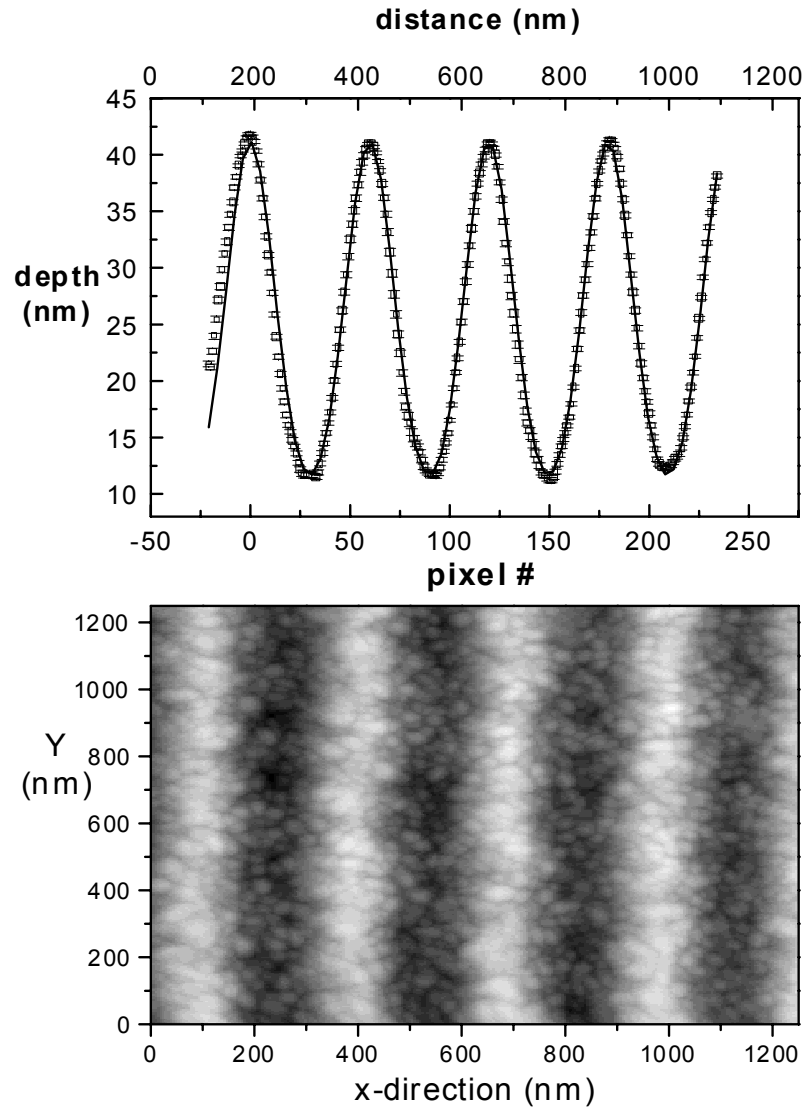
Figure 5.6(a) Shows the mean profile of the diffraction grating taken from (b). (b) shows an non-contact AFM image of the corrugated ITO surface. Background roughness can clearly be seen with feature sizes between 3-4 nm in height.

The AFM image of the patterned ITO also revealed some background roughness. This background roughness was between 3-4 nm in height. AFM images of planar ITO (not shown) deposited at the same time also revealed similar surface roughness, indicating it is the ITO itself rather than the patterning technique that caused the roughness.

5.5 Experimental Results and further modelling.

To accurately identify the modes supported by the corrugated structure, a map of the dispersion diagram for the system needs to be established. We undertook four types of measurement to map the modes in two stages. Firstly before deposition of the OLED a mode map of the ITO on silica diffraction grating was obtained from optical transmission measurements. Transmission was measured as a function of wavelength and incident angle, both of which were computer controlled; a schematic of the experimental set-up for recording transmission is given in figure 5.7.

This structure supports guided modes in the ITO layer because ITO has a higher refractive index than the silica. Accurate modelling of these modes allowed independent verification of the grating profile and the thickness of the ITO. Results and modelling of the transmission data are shown in figures 5.8 and 5.9.
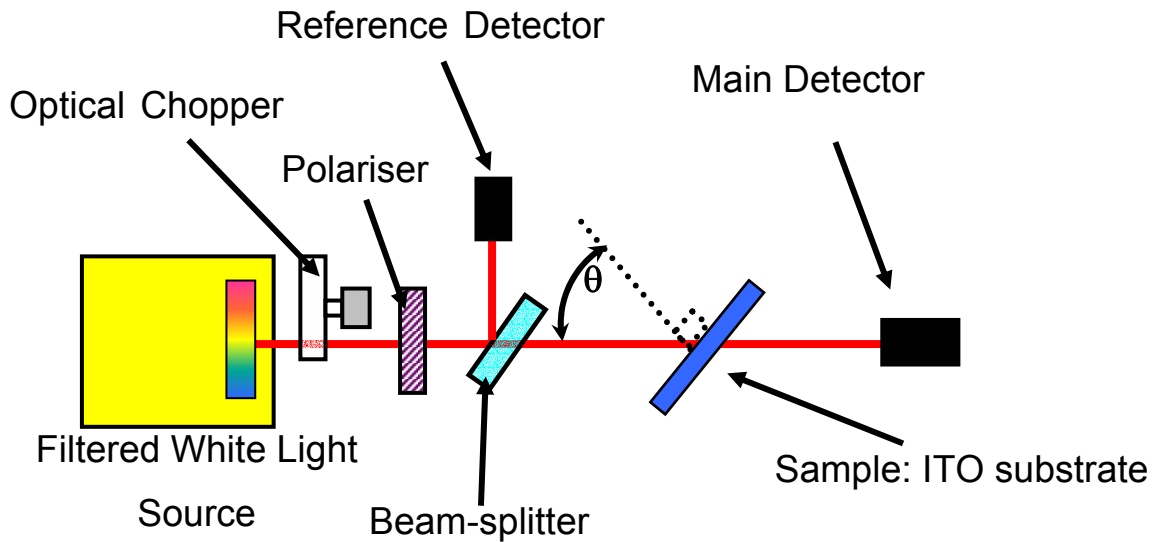
Figure 5.7. Experimental set-up for studying transmission through the corrugated ITO substrates. A spectrometer is used to sweep the emission from a white light source whilst the sample is rotated to maintain a constant in-plane momentum for a chosen energy.

(a)   (b)
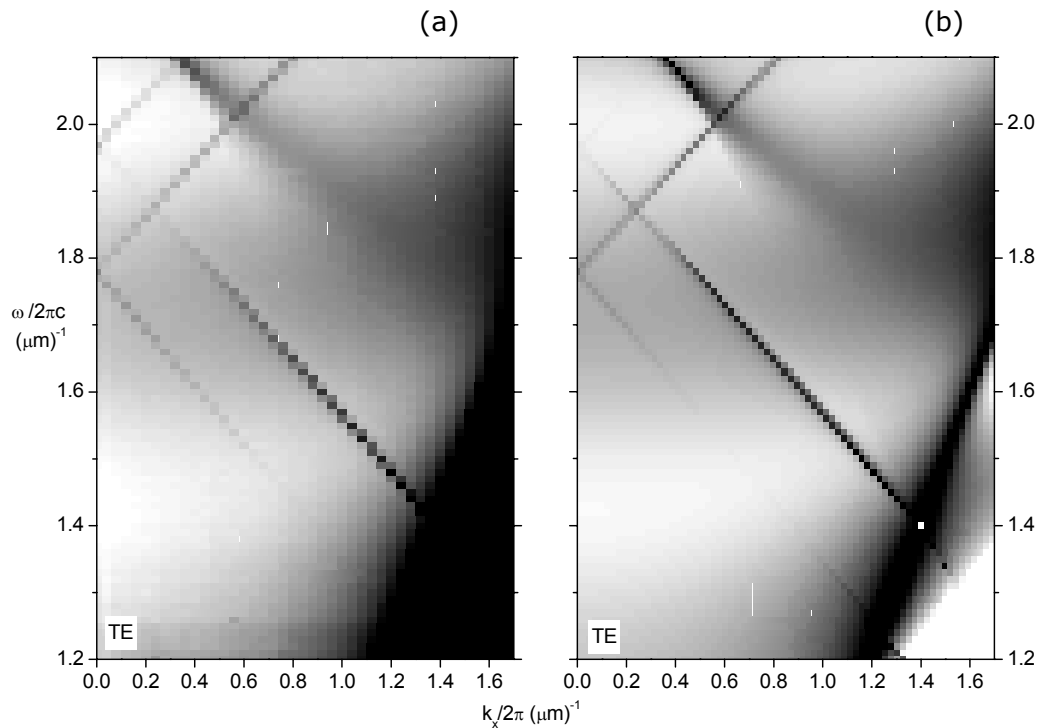
Figure 5.8. (a) Experimentally measured transmission data (TE polarised) of the nanostructured substrate. The thickness of the ITO is 356 nm; 5.7 (b) shows the theoretically modelled transmission data for TE polarisation. Grey scale range, Z_{min}=0 (white) and Z_{max} =0.4 (black).

Suitable choices of wavelength and angle allow plotting of the transmission as a function of frequency and in-plane wavevector. Dark indicates high transmission, where incident light is coupled to one of the modes of the system. The forward and backward Bragg scattered modes can clearly be identified and excellent agreement is seen between the transmission data and the modes produced from a specially adapted mathematical model shown in figure 5.8 (b) and 5.9 (b). The adapted modelling technique developed by J. Wasey of Exeter from a technique originally developed by *Chandezon et al.* (1982) is based on solving Maxwell's equations in a transformed co-ordinate system in which the corrugated interfaces are planarised. Thus, the sinusoidal nature of each interface can be properly incorporated into the calculation.
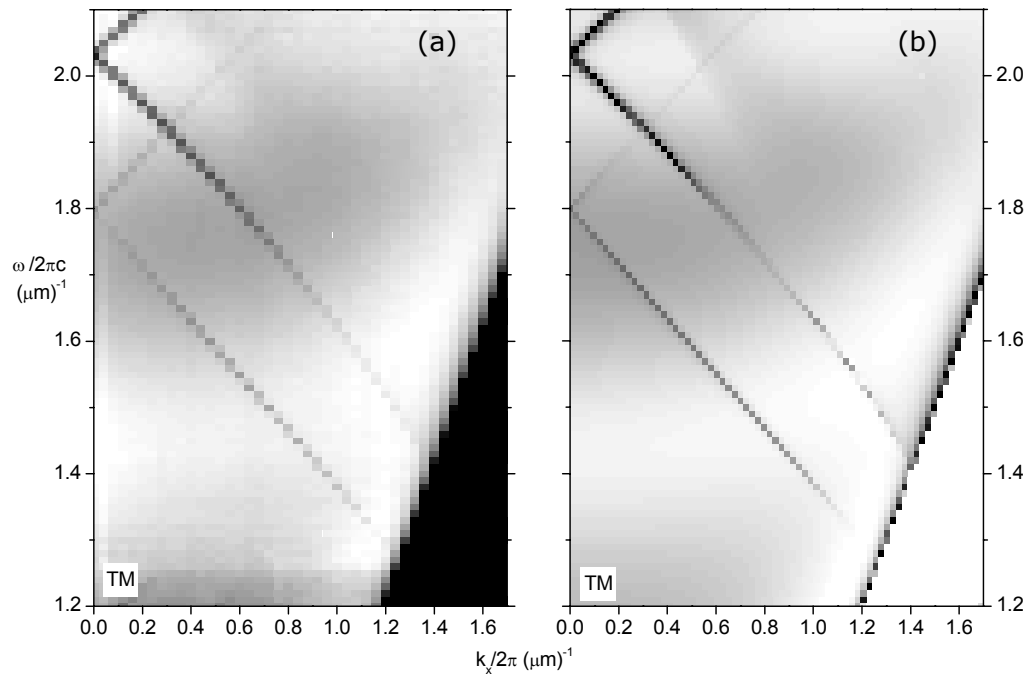
Figure 5.9 (a) Experimentally measured transmission data (TM polarised) of the nanostructured substrate. The thickness of the ITO, is 356 nm; 5.8 (b) shows the theoretically modelled transmission data for TM polarisation. Grey scale range, $Z_{min}=0$ (white) and $Z_{max}=0.5$ (black).

After deposition of the remaining device layers, the photoluminescence, as a function of emission angle for the planar and corrugated OLEDs was recorded. The experimental configuration used in the photoluminescence experiments is shown in figure (5.10). The sample was mounted at the centre of rotation of a motorised stage. This stage allowed angle selection to an accuracy exceeding 8×10^{-3} of a degree. Excitation of the Alq$_3$ was achieved by irradiation from an argon-ion laser at 457.9 nm. The pump light was coupled into an optical fibre fitted with a focusing lens. This arrangement allows the light source to be mounted on the sample holder and so provide constant pump conditions throughout the experiment. The emitted light was collected through a 2 mm diameter aperture via a polariser and focused through a 4 cm focal length lens onto an optical fibre. The optical fibre carried the light to the detection system, which

consisted of a spectrometer and Charge Coupled Device (CCD) detector.
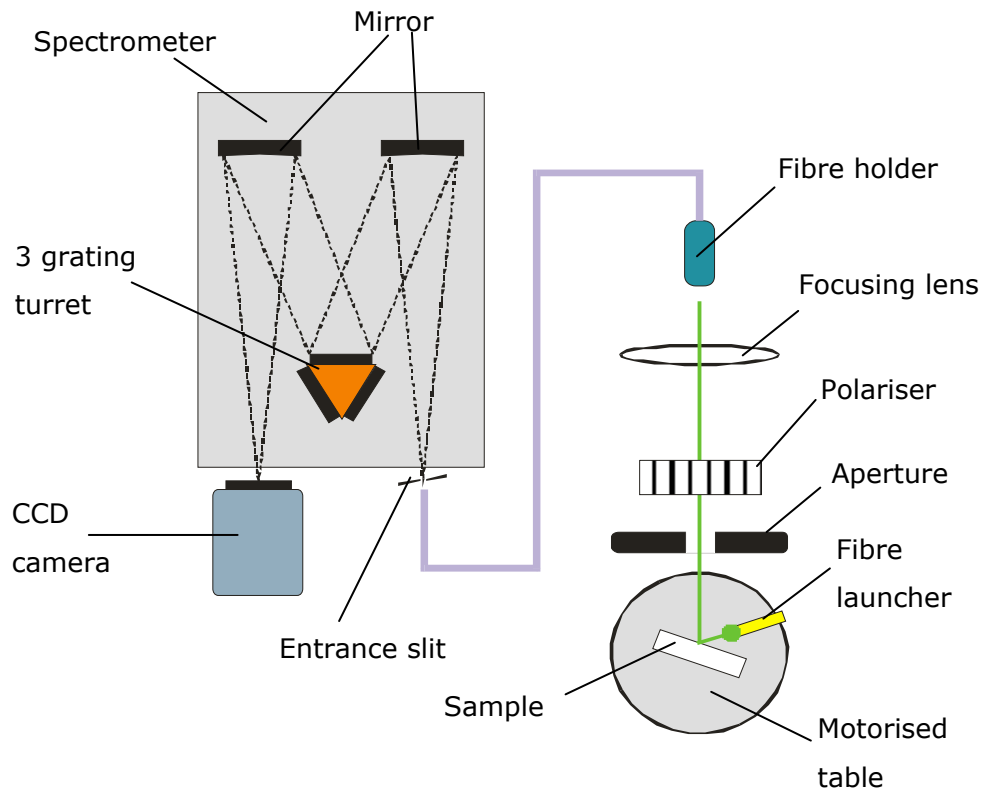
Figure 5.10. Schematic of the experimental set-up used for taking the photoluminescence measurements.

Light entering the entrance slit of the spectrometer is incident onto the collimating mirror. The collimated light then strikes one of the three gratings mounted on the motorised turret. The grating disperses the light into the individual wavelengths which are then focused by a second mirror to form an image of the entrance slit on the CCD detector. Each position in the image represents a different wavelength. The entire system is controlled by software and allows effective snap shots of the spectrum to be taken for any incident angle. Individual line spectra were recorded for each angle of incidence. An example of a typical line spectrum is shown in figure 5.11.
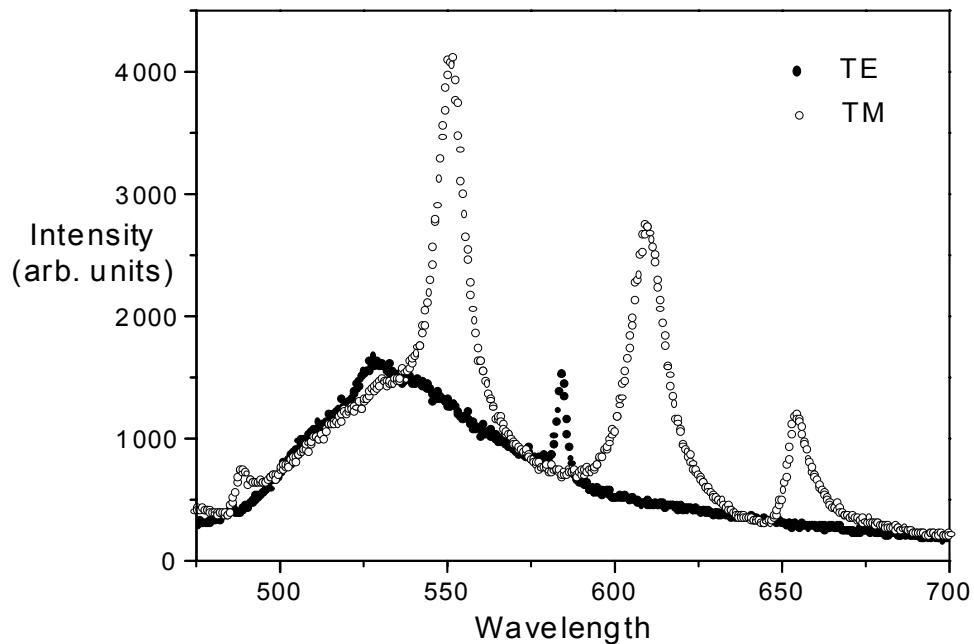
Figure 5.11. A typical example of line spectra, showing photoluminescence from the microstructured OLED manufactured in this work (schematic shown in figure 5.5). Emission for both polarisations is shown. Data was taken at $\theta=0^0$.

Employing the motorised table allowed very small steps in angle to be selected making it possible to accurately track modes which change energy very quickly as a function of incident angle. Because the data was recorded in such small increments in angle ($\leq 0.5^0$) a large number of recorded spectra were measured in each experiment. Therefore it was convenient and useful to compile a matrix and express the data as a grey scale graph. For a planar OLED structure the emission (shown in figure 5.12) takes place via leaky modes of the device and tails off with viewing angle as expected for lambertian emission. Furthermore the emission was found to be unpolarised; this is expected from small molecule based devices with isotropic dipole distributions.
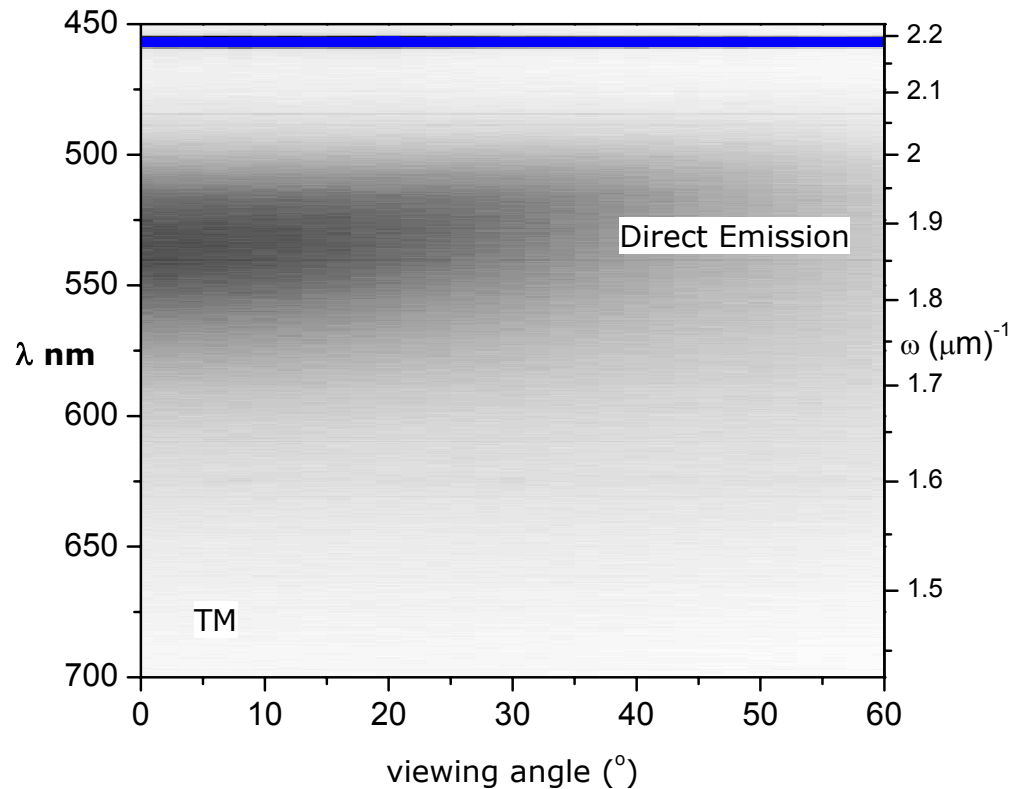
Figure 5.12. Grey scale image of photoluminescence from a planar OLED structure of the form shown in figure 5.5. Dark indicates direct emission into 'leaky' modes of the device.

Figure 5.13 shows photoluminescence from an equivalent corrugated OLED structure. The photoluminescence data indicates which of the structure-scattered optical modes may be coupled to via direct emission. We have indicated on the diagram the identity of the modes. These modes are deduced from modelling the reflectivity data shown later. We note the pronounced effect that adding the corrugation to the structure has on the emission of the device. The TM emission data shows modes significantly stronger than the background emission, whereas in TE emission the Bragg scattered modes are only slightly stronger than the background emission. The strongly polarised nature of the emission has clear implications for device applications especially if OLEDs are used in conjunction with liquid crystal displays. In all cases here and later, the samples were mounted such that at zero degrees incidence TM emission is defined

as emission. With its electric field component perpendicular to the grating groves, the Bragg vector associated with corrugation lies in the plane of incidence.
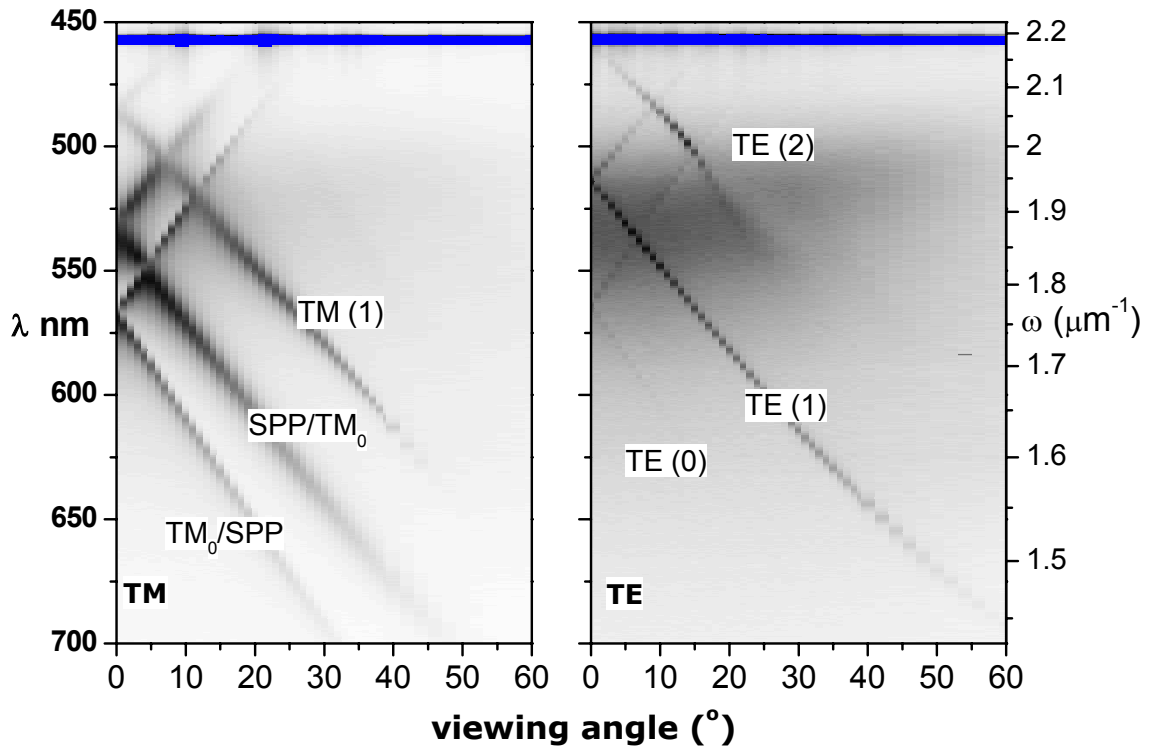
Figure 5.13. Photoluminescence spectra recorded from a nanostructured OLED for TM and TE polarisations. Dark indicates strong emission. The forward and back-scattered modes are clearly visible as they pass through the Alq_3 emission. Light of wavelength 457.9 nm from an argon-ion laser was used as the pump source.

Secondly, reflectivity data for the structure as a function of both incident angle and wavelength were recorded. As for transmission, a computer controlled rotation table was used to move the sample. Suitable choices of both wavelength and angle allowed the reflectivity as a function of frequency and in-plane wavevector to be plotted. Full details of this process have been published elsewhere [*Salt and Barnes* (1999)]. The results of the measurements are shown in figure 5.14 and 5.15 (a) and (b) for TE and TM polarisation respectively.
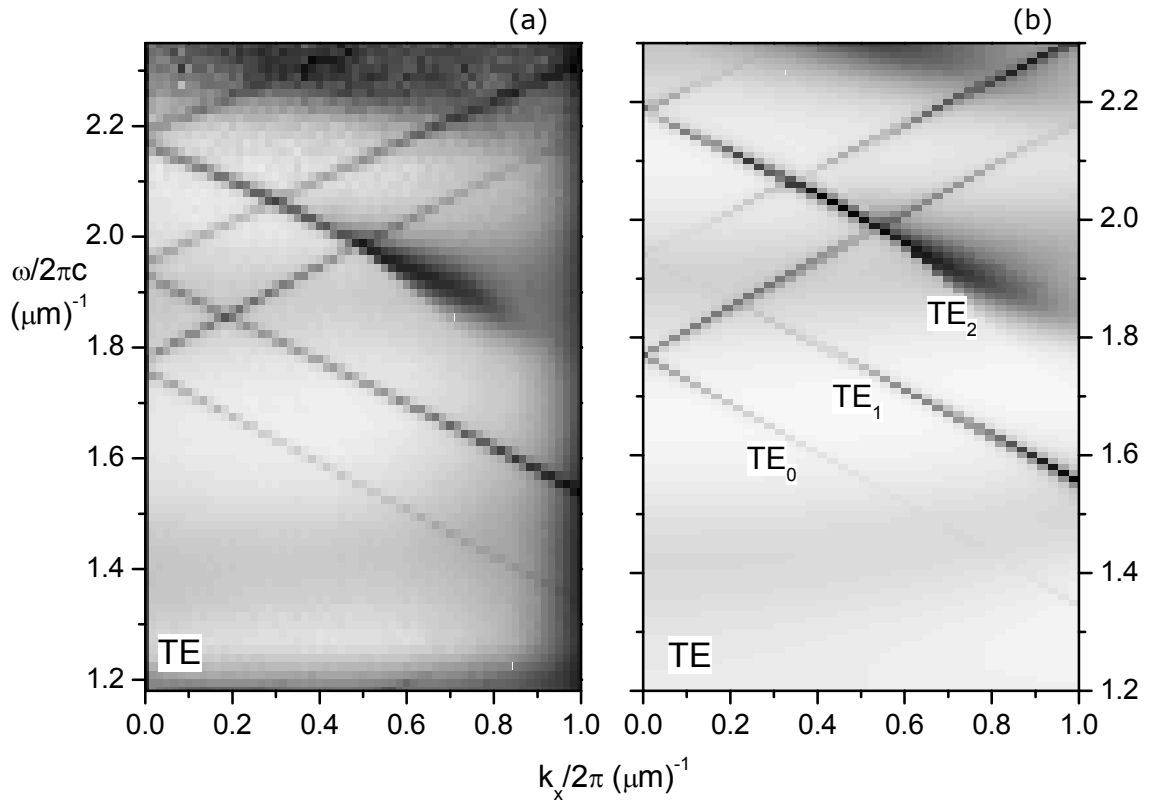
Figure 5.14 (a) Experimentally measured reflectivity data (TE polarised) of the nanostructured OLED. The thickness' of the different layers were as follows; ITO, 356 nm; combined thickness of NPD and Alq$_3$, 100nm; LiF, 0.8 nm (nominal); Aluminium cathode, 150 nm. 5.13 (b) shows the theoretically modelled reflectivity data for TE and TM polarisations respectively. Modelling using adapted conical program by J. Wasey. Grey scale range, Z_{min}=0 (black) and Z_{max} =0.9 (white).

Dark regions on these data correspond to low reflectivity, where incident light couples to the modes of the structure. As in the photoluminescence data, forward and back-scattered modes can clearly been seen. We note that the position of the modes in reflectivity agrees with the features seen in the photoluminescence spectra.

In the reflection and photoluminescence data, some interference, or gaps, between forward and backward scattered modes may be seen. These gaps are precursors to the formation of photonic band gaps, the optical equivalent of the energy gap in semiconductors.

Photonic crystal structures were initially realised by *Yablonovitch et al.* (1989), who made the first photonic crystal in the microwave regime by drilling millimetre diameter holes into a block of material. The new optical material was named "Yablonovite", and exhibited a 3-D photonic band gap. This is a very active area of research world wide with promising applications in optical computing and communications [*Parker and Charlton* (2000)]. Recent practical applications of band gap effects produced by single corrugated Bragg gratings have been realised by *Andrew et al.* (2002) in distributed-feedback polymer lasers fabricated on corrugated silver gratings.
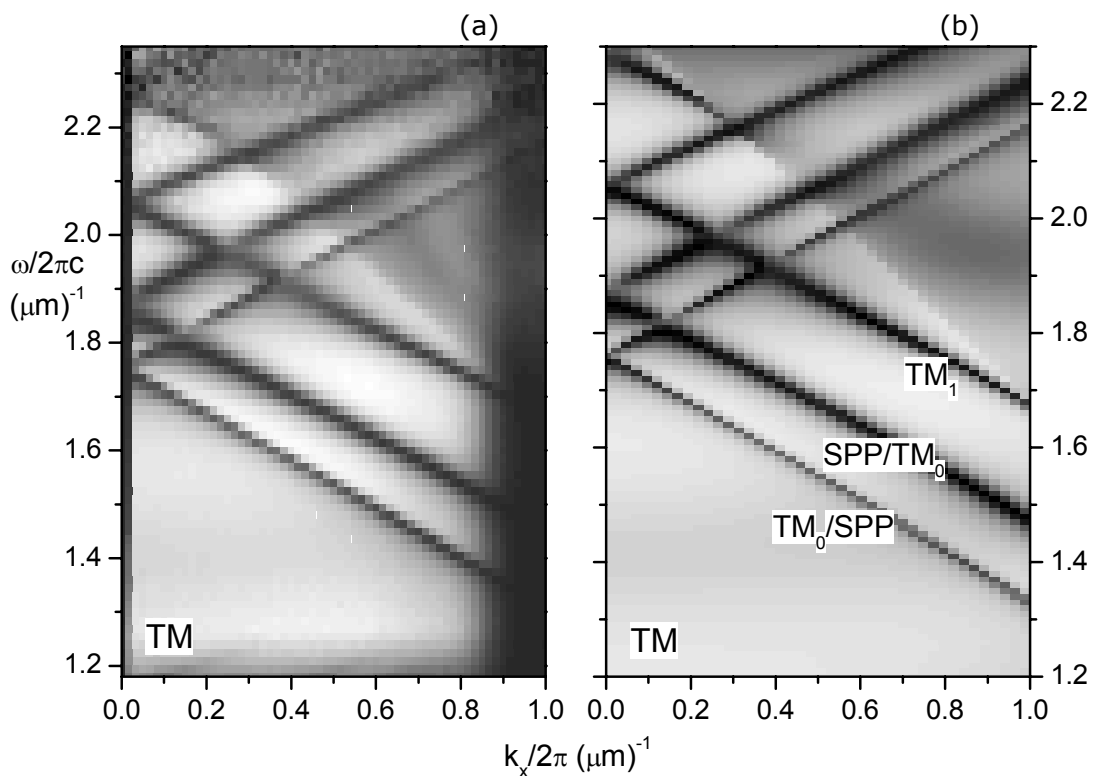
Figure 5.15. (a) Experimentally measured reflectivity of TM polarised light from the nanostructured OLED. The thickness' of the different layers were as follows; ITO, 356 nm; combined thickness of NPD and Alq_3, 100nm; LiF, 0.8 nm (nominal); Aluminium cathode, 150 nm. 5.14 (b) shows the theoretically modelled reflectivity data for TM polarisation. Modelling using adapted conical program by J. Wasey. Grey scale range, $Z_{min}=0$ (black) and $Z_{max}=0.9$ (white).

As with the photoluminescence data, we have indicated which mode is responsible for which feature. A surprising discovery was the fact that there appear to be two SPP modes in the system. Actually both modes are hybrid SPP-guided modes each having the character both of an SPP and a guided mode. The mode labelled SPP/TM$_0$ most resembles the optical fields associated with a conventional SPP. The reason for this puzzling hybrid SPP is due to the thickness of the ITO.

TE polarisation optical reflectivity data strongly resembles the transmission plots of the ITO on silica substrate (figure 5.8), with modes appearing at almost identical energy and wavevector. This is not the case for the TM polarisation optical reflectivity data. Here the SPP mode propagating along the Al/ Alq$_3$ interface complicates the mode map. The other TM modes do not appear at quite the same energies as in the ITO substrate grey scale because of the presence of the SPP mode. From a brief examination of the reflectivity dispersion we might imagine that the SPP mode has been inserted at an energy in-between the TM$_0$ and TM$_1$ modes, its presence shifting the TM$_0$ mode to a lower energy. It not *a priori* obvious that this is the case. Consequently we undertook modelling of the optical fields on the band-edges of the dispersion diagram using an adapted version of the conical code used for modelling the reflectivity and transmission data. Three frequencies were modelled, corresponding to where the three back-scattered modes cross the k=0 µm^{-1} axis on figure 5.15(b). The modelling (shown in figures 5.16 –5.18) is of the $|E_y|$ fields normal to the plane of the sample. We recall from chapter 2 that the SPP has strong E$_y$ fields and so modelling $|E_y|$ will show up any SPP field enhancement. Figures 5.16 and 5.17 indicate field enhancement near the metal cathode that decays into the ITO.
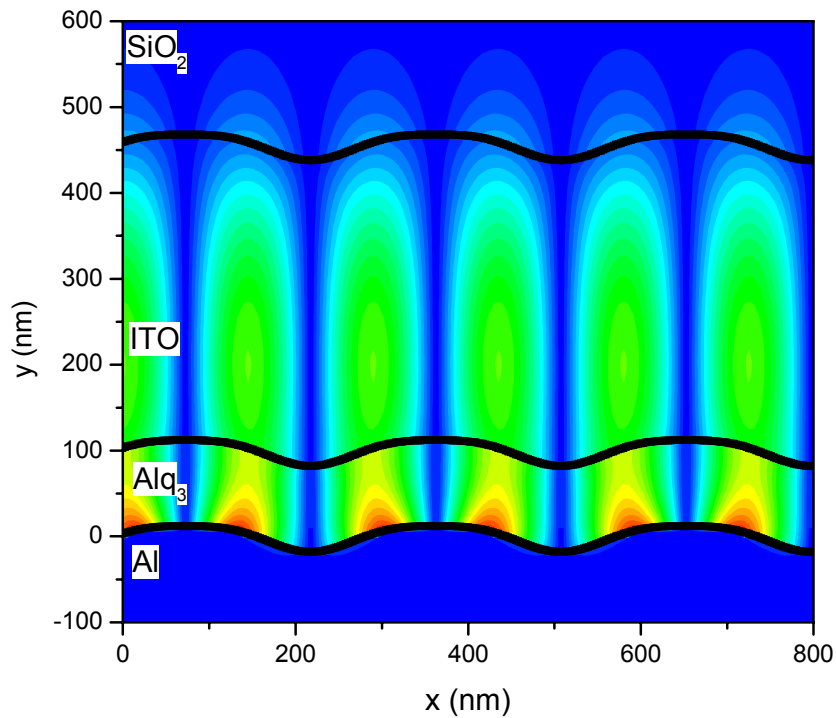
Figure 5.16. Calculated, relative $|E_y|$ field intensity at $\omega=1.75$ µm^{-1} and k=0 µm^{-1} for the TM$_0$/SPP mode supported by the textured OLED structure, obtained from the theoretically calculated reflectivity data. Red areas indicate high field strengths and blue low field strengths.

These correspond to the two lowest order TM modes (TM$_0$/SPP and SPP/TM$_0$ on figure 5.15) and indicate that the two modes have optical fields of both SPP and guided modes. We conclude these two fully guided TM modes will have plasmon fields associated with them. The extent of this plasmon 'mixing' will depend on energy and wavevector, with some modes being more plasmon-like than other modes. The difference between the TM$_0$/SPP and SPP/TM$_0$ modes is an antinode roughly mid-way through the ITO layer and is a useful way of distinguishing between the hybrid solutions.
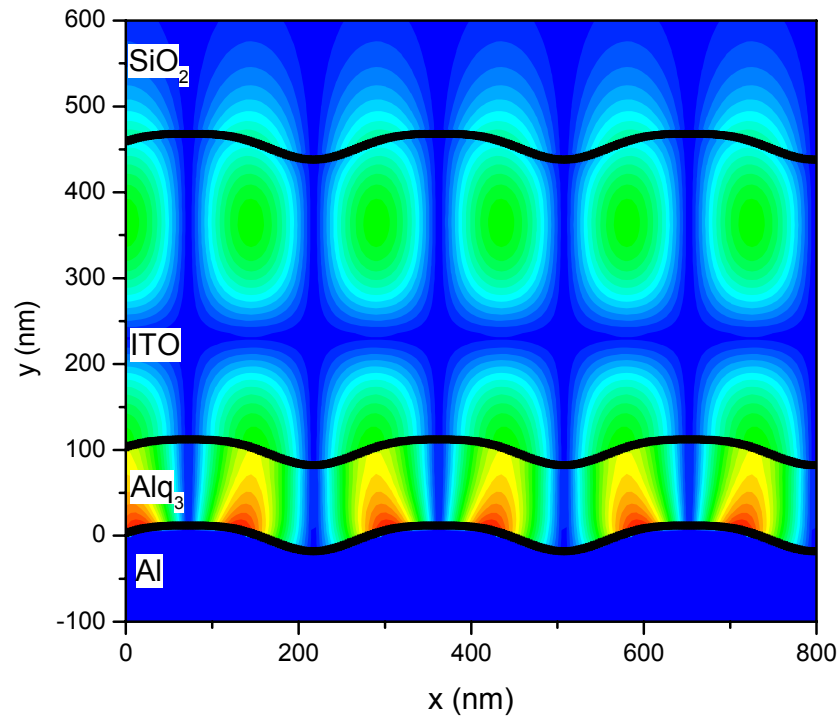
Figure 5.17. Calculated, relative $|E_y|$ field intensity at $\omega=1.85$ µm^{-1} and k=0 µm^{-1} for the SPP/TM$_0$ mode supported by the textured OLED structure. Obtained from the theoretically calculated reflectivity data. Red areas indicate high field strengths and blue low field strengths.

Figure 15.18 shows the E_y fields of a TM$_1$ mode. From the field profile diagrams in chapter 2 (figure 2.7) we expect 3 nodes in the TM$_1$ field with some field enhancement at the metal-dielectric interface but without the long decay into the ITO associated with an SPP.
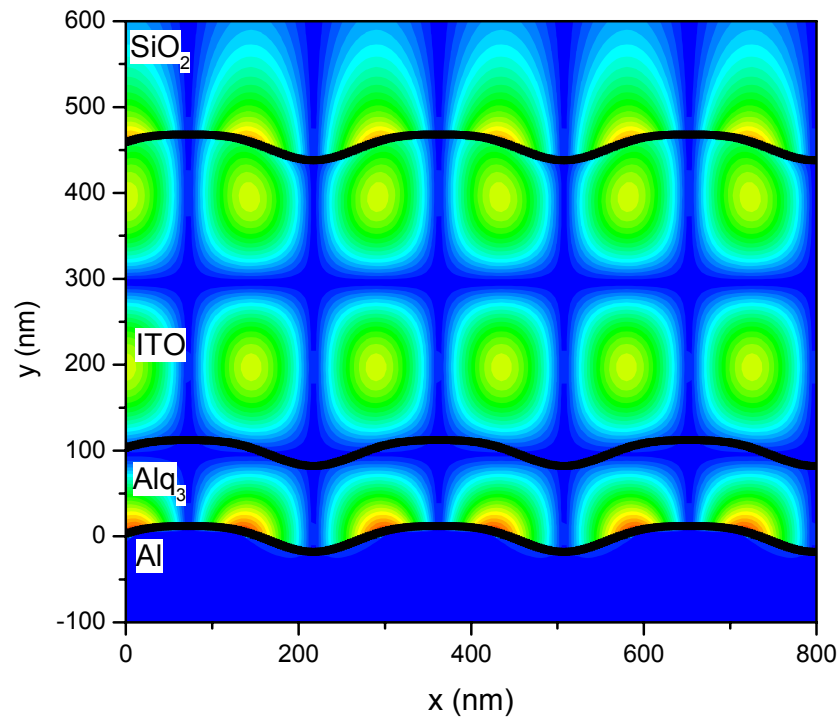
Figure 5.18. Calculated, relative $|E_y|$ field intensity at $\omega=2.05$ μm^{-1} and $k=0$ μm^{-1} for the TM_1 mode supported by the textured OLED structure, obtained from the theoretically calculated reflectivity data. Red areas indicate high field strengths and blue low field strengths.

Figure 5.19 illustrates how the hybrid SPP guided mode evolved. The increase in ITO thickness results in the interaction of two dissimilar electromagnetic modes [*Gruhlke and Hall* (1989)] (namely the SPP and the TM_0 waveguide mode) in the ITO and occurs in the near infrared region of the spectrum. The interaction manifests itself as anti-crossing between the SPP and TM_0 [*Gruhlke and Hall* (1989)]. The result of this anti-crossing is that the SPP mode is deflected away from the Alq_3 light-line across towards ITO light line, so resembling a guided mode (TM_0/SPP). The TM_0 mode is forced up along the Alq_3 light line becoming SPP like (SPP/TM_0). As we increase in frequency other guided modes can be supported by the structure. They may in turn anti-cross with the 'SPP' becoming SPP like too. This anti-crossing phenomenon is similar to the strong exciton-photon interactions examined in chapter 6.

121
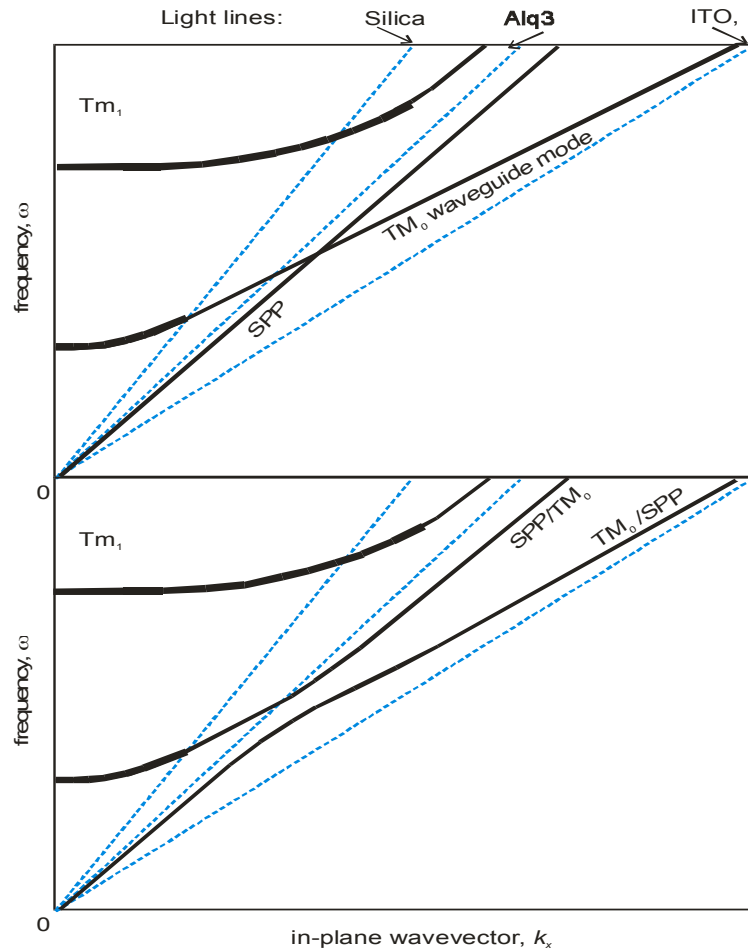
Figure 5.19. Schematic of the dispersion curves for SPP guided made interaction a) shows modes crossing without interaction b) shows the formation of the band gap due to the SPP TM_0 interaction.

We undertook modelling of the power dissipation spectrum for the OLED as before but adjust for ITO thickness of 356 nm (figure 5.20, upper spectrum). The fraction of power underneath the curve to the left of the silica light line indicates the amount of power coupled to leaky modes of the device. The sharp peaks to the right of the silica light line at higher in-plane wave vectors correspond to the trapped waveguide modes. The power dissipation spectrum plotted against frequency and in-plane wave vector gives the dispersion diagram shown in figure 5.20 (bottom) where the different modes have been labelled. The sharp distinct lines are to the right of the silica light line and are all guided in the Alq_3 and ITO. From modelling the optical fields within the OLED alluded to before, we know that the

modes immediately to the right of the Alq_3 line will be most SPP like in nature whilst the modes up against the ITO light line will most resemble guided ITO modes.
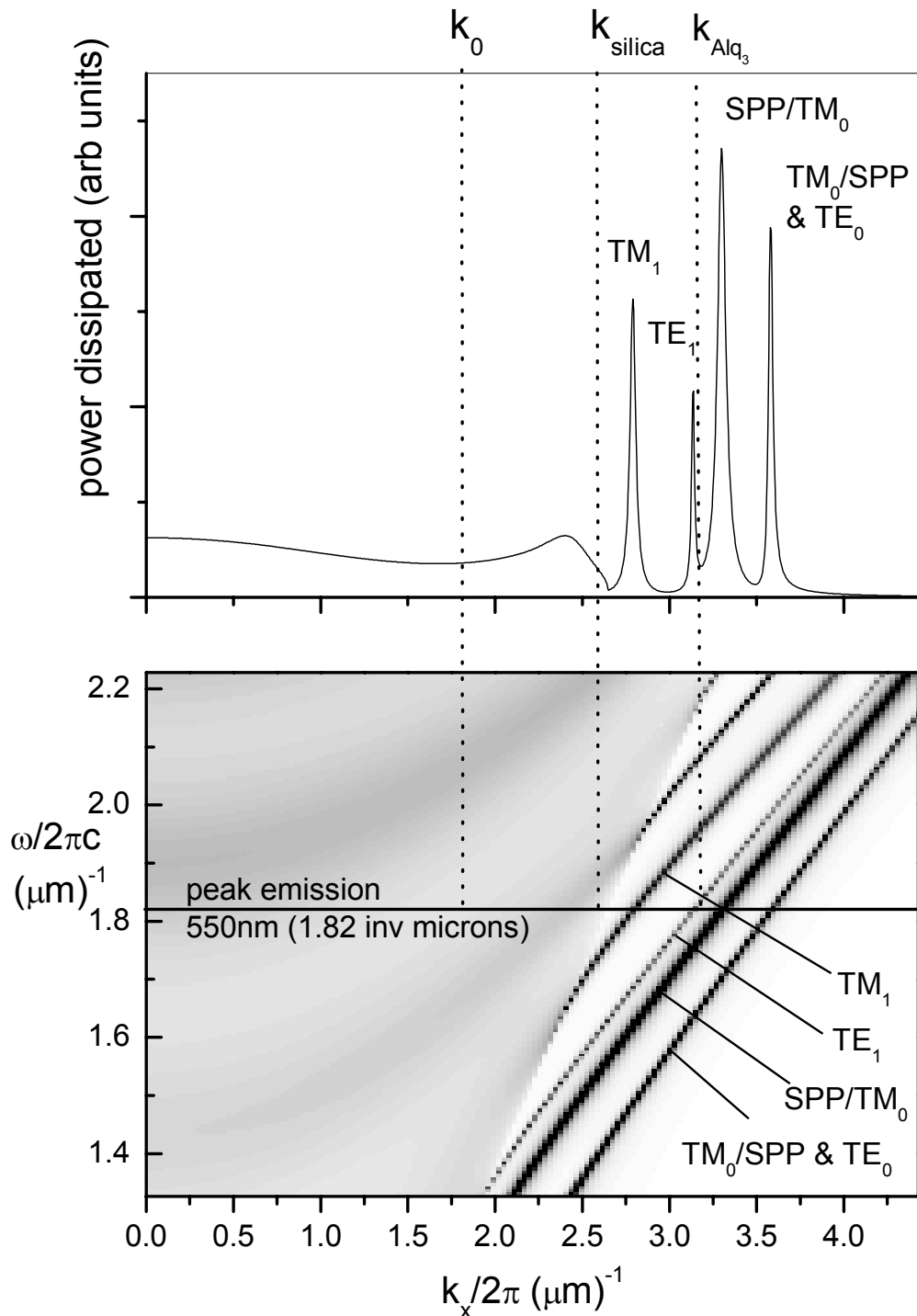
Figure 5.20. Calculated power dissipation spectrum (top) for the planar OLED structure used in these experiments. The permittivities of the different media are given in the appendix. Modes to the right of the silica light line are fully guided. This dissipation spectrum was calculated at the peak of the bulk Alq_3 emission spectrum 550 nm. Figure 5.16 (bottom) shows the dissipated power spectrum in terms of frequency and in-plane wavevector thus mapping the dispersion of the Planar

OLEDs manufactured in this work. Dark indicates strong coupling to modes. In these calculations the emitter was placed 50 nm from the aluminium cathode. Model by J. Wasey.

We conclude that although the extra thickness of ITO increases the number of modes in the device. It is not expected that this effect will greatly alter efficiency. Selectively integrating the area under the guided modes for different emitter cathode separations (figure 5.20) yields similar results to those shown in figure 5.3 in that the SPP decay route is the dominant power loss mechanism for cathode emitter separations between 15 and 70 nm. This is because the increase in modes simply results in a redistribution of power between a greater number of modes [*Benisty et al.* (1998)]. By the same token further modelling undertaken (but not presented here) has shown that just 10 nm of ITO is sufficient to support the lowest order waveguide modes as well as the SPP. From figure 5.21 we estimate that in the absence of any corrugation only ~ 8 % of the light emerges into the air from the Alq_3 based device.
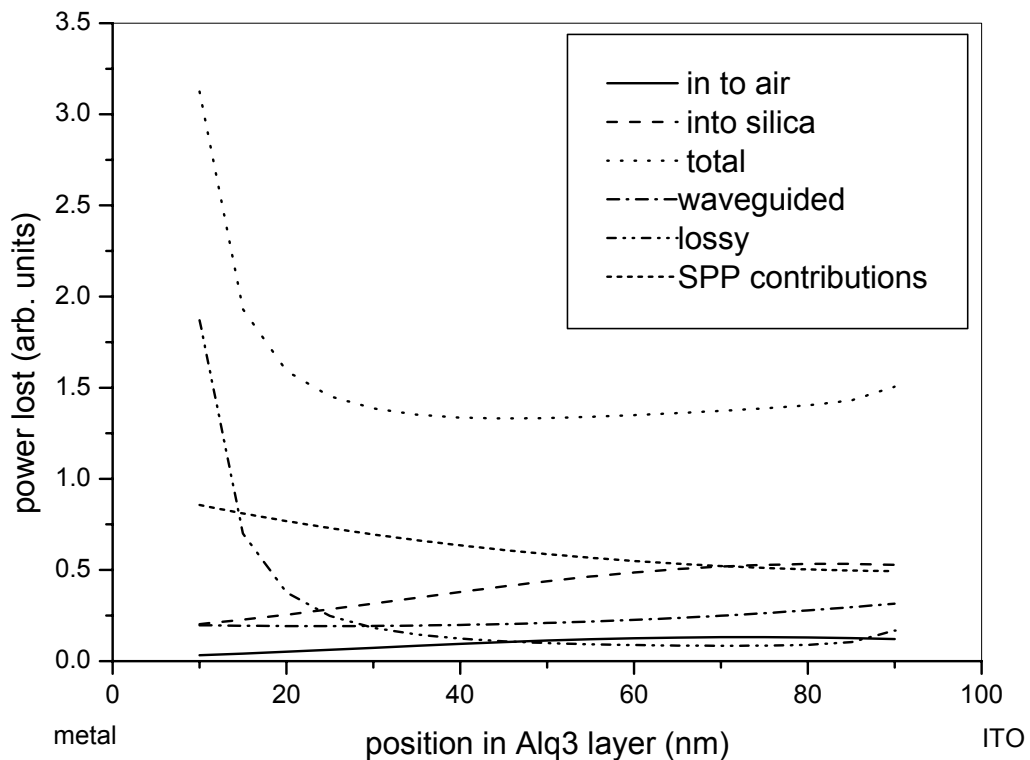
Figure 5.21. Calculation of the power coupled to the different modes of the planar OLED as a function of distance between emitter and the aluminium cathode. Coupling to SPP contributions is the dominant power loss for emitter-cathode separations between 15 and 70 nm. Model by J. Wasey.

Finally, and possibly most importantly we now demonstrate that SPP modes also dominate electroluminescence. Figure 5.22 (a) and (b) show electroluminescence data taken for an incident angle of zero degrees for TE and TM data respectively. Electrical operation was achieved by driving the OLEDs at ~ 10V and a current of ~10 mA. Also included in each case are the electroluminescence spectra from a planar control OLED. For accurate comparison between planar and corrugated structures the strongly varying background emission of both TE and TM corrugated emission has been normalised to that of the planar device. As expected all the modes that appeared on the reflectivity and photoluminescence data also appear in electroluminescence. In particular we note the presence of the SPP modes. The exact mode position however does not quite agree with the photoluminescence data. This is attributed to a slight difference in film thickness. The devices used for electroluminescence were made

125

on identical ITO coated substrates as those measured in photoluminescence. However the organic layers are slightly different. 38 nm of NPD and 68 nm of Alq_3 were used as opposed to 50 nm of each layer before. The line spectra also allow us to calculate the increase in emitted light in the forward direction arising from the inclusion of the corrugation.
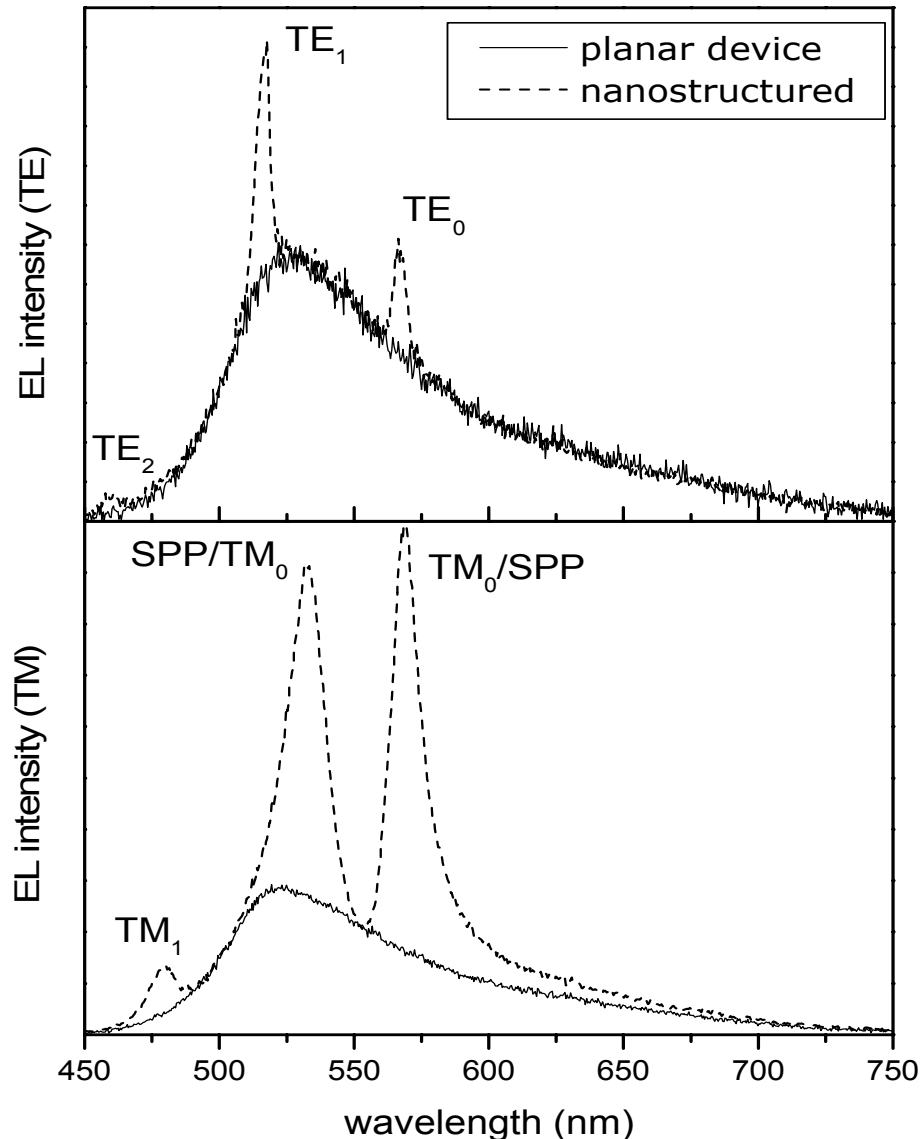
Figure 5.22. (a) and (b) are sample electroluminescence spectra for TE and TM polarisations respectively for the corrugated OLED (figure 5.5). The spectra were taken at a polar angle of zero degrees and correspond to emission in the forward direction. Also included are the emission spectra for the planar device. In both cases the background emission for both planar and corrugated structures has been

scaled (2% nominally) to aid direct comparison. The modes shown in electroluminescence show the same dispersion as those shown in reflectivity and photoluminescence.

Analysing the TM polarisation line spectra, by integrating the area under the curve across the visible, shows that the corrugated structure out-couples a factor of 2 more light than the planar device. We calculate that in the forward direction with the grating vector lying in the plane of the emission ~50 % (calculated from the area under the peak) of the emitted light is from the Bragg scattered SPP modes. This agrees well with similar measurements to out-couple waveguide modes from OLED devices based upon the conjugated polymer MEH-PPV [*Lupton et al.* (2000)].

5.6 Summary

We have fabricated, measured and numerically modelled an Alq$_3$ based organic LED structure with a sub-wavelength grating patterned into each layer of the device. We have demonstrated in photoluminescence and electroluminescence that emission couples effectively to the waveguide modes of the device including surface plasmon modes and that much of the power lost to SPP modes may be recouped by using periodic microstructure. Reflectivity and transmission measurements allowed all the modes of the structure to be identified and excellent agreements were found upon comparison with a numerical model.

Modelling of a planar OLED structure indicates that only ~ 8 % of the light emerges into the air from the Alq$_3$ based device. Based on studying emission spectra of our corrugated device as a function of emission angle we estimate that ~ 50 % of the power radiated by this device is due to surface plasmon mediated emission, i.e., via hybrid SPP/ TM$_0$ and TM$_0$/SPP modes. This implies an increase in out-

coupling efficiency from 8% to 16%. It is clear that there is considerable scope for improving device efficiency.

5.7 Future work

We can consider other possible geometries that may allow us to couple light out of an OLED. One possibility is the extraction of the light lost to the SPP mode on the metallic cathode through the metal layer. Work by *Ebbesen et al.* (1998) looking at the extraordinary transmission of light through a thick metal film perforated with sub-wavelength holes suggests this may be possible. Indeed, it is true to say that there is much interest in this subject as extraction of light through a metallic cathode promises to lead to the integration of OLEDs with existing silicon technologies. A question we may speculate on is whether the metal really requires holes, or whether an appropriate texturing of a continuous film suffice instead. Work by *Gruhlke* (1986) on cross-coupling of surface plasmons through optically thin continuous films also suggests that extracting energy through films using surface plasmons may be a viable option. Although the exact mechanisms involved in achieving this are still not properly understood it looks to be a promising area for research.

In the next chapter we again examine cavity interactions with excitons, but from a rather different perspective. So far we have only considered so called 'weak' interactions between an electromagnetic cavity field and the optical excitations of a photonic material. In the next chapter we look at strong coupling between excitons and cavity photons and the formation of new quasi-particles which are a mixture of the two optical states, so called cavity polaritons.

Chapter 6

Strong Exciton-Photon Coupling in Low-Q all Metal-Mirror Microcavities.

6.1 Introduction

Solid-state cavity quantum electrodynamics allows a range of new phenomena to be investigated. Of primary interest are methods to control spontaneous emission [*Kleppner* (1981)]. By limiting the number of modes into which the emission may take place, the emission of light may be modified. A particularly simple and attractive way of providing such modal control is by using a microcavity. Here, the emitting species are placed between two plane mirrors that are separated by a distance of the order of the emission wavelength. There are two regimes of operation. In the weak coupling regime the spatial and temporal distribution of the emitted radiation can be altered, but the emission frequency remains unaltered (at least in the case of monochromatic emission). This is a simple perturbation embodied in Fermi's Golden Rule. Weak coupling effects were discussed in the context of organic LED devices in the previous chapter. In the strong coupling regime new states are created which are a superposition of exciton and photon states; in this case Fermi's Golden Rule no longer holds for the optical transition probabilities. Strong coupling can occur in the single quantum limit in very high Q cavities [*Carmichael. et al.* (1989)], or in the many quanta regime where the required absorption is obtained through the presence of many emitting species (commonly excitons) inside the cavity [*Weisbuch. et al.* (1992)]. This latter case is also known as normal-mode coupling [*Khitrova. et al.* (1999)] and is an intensive area of research due in part to the interest in coherent, stimulated effects in such systems [*Yamamoto Y. et al.* (1991), *Savvidis. et al.* (2000)] which may lead to new devices.

The field has recently expanded to include Frenkel excitons supported by organic materials [*Lidzey. et al. (a)* (1998), *Lidzey. et al. (b)* (1999), *Lidzey. et al. (c)* (2000)], as well as those involving excitons in inorganic semiconductors, the materials in which such strong coupling was originally observed [*Weisbuch. et al.* (1992)]. The use of organic materials has been important in that it has lead to the observation of significantly larger strong coupling effects at room temperature and leads to the possibility of more easily fabricated devices [*Lidzey. et al. (c)* (2000)].

In strong coupling, the exciton mode of the cavity material and the photon mode of the microcavity interact to create a new quasi-particle termed a cavity polariton. A key phenomenon associated with strong coupling is the anti-crossing of the exciton and photon mode where, in the absence of a significantly energetic interaction, they would have crossed (see section 3.4). For single quantum oscillators interacting with a photon, this effect is known as vacuum Rabi splitting [*Rarity and Weisbuch* (1996)]. The phenomenon has commonly been observed by studying the frequency and angle dependence of the reflectivity of microcavity structures [*Weisbuch. et al.* (1992), *Lidzey. et al. (c)* (2000)]. Though very successful, this technique has some limitations. Firstly, until now investigations into strong coupling in organic and inorganic materials have been conducted either using two high quality Bragg reflectors as microcavity mirrors or one Bragg reflector together with one optically thick metal mirror [*Lidzey. et al. (c)* (2000)]. Bragg reflectors consist of alternating layers of high and low index dielectrics and allow high Q microcavities to be constructed [*Carmichael. et al.* (1989)]. Materials are chosen to provide the largest index difference between mirror layers and hence the shortest cavity length, thereby confining the optical fields more and giving rise to a larger splitting (chapter 2).

However Bragg mirrors are resonant structures that have high reflectivities over a relatively narrow 'stop-band' frequency range. Consequently, for a given wavelength they also have high

reflectivities over a limited range of in-plane wavevectors. One would prefer to cover as wide range of in-plane wavevectors as possible. Furthermore Bragg mirrors are complicated multilayer structures of alternating λ/4 layers of semiconducting materials such as GaAs and AlAs that are grown by molecular-beam epitaxy (MBE).

These limitations could potentially be overcome by using metal films for both of the mirrors. Also, if the metals are thin enough then transmission as well as reflection measurements become possible. Metals provide high reflectivities over wide range of angles and frequencies thus allowing studies over a wide range of in-plane wavevectors and wavelengths. Finally, metallic mirrors represent a far simpler fabrication route as metals may be simply deposited by thermal evaporation (chapter 4).

Despite the recent use of metal mirror microcavities in studying photonic band gap effects [*Salt and Barnes. (a) (2000)*], it is not clear whether microcavities made with all metal mirrors will be able to sustain strong coupling. This is because metal microcavities offer a much lower Q than typical microcavities used so far in strong coupling experiments. In this chapter we show for the first time that microcavities fabricated using two metal mirrors can exhibit strong coupling behaviour.

The recent use of organic materials to study strong coupling has identified aggregates of organic dye molecules as an advantageous physical system. Microcavities based upon organic materials and employing at least one metallic mirror have relatively modest Q. Consequently to observe strong coupling, excitons with very large oscillator strengths and small Stokes shift between absorption and emission are desirable, both properties applying to cyanine dyes that form J-aggregates [*Kobayashi.* (1996)]. The formation of the J-aggregate results in a large sharp absorption peak with large oscillator strength (called the J-band) below the monomer transition band, with spectral features significantly different to that of the monomer spectrum. Emission is similarly sharp, showing a

characteristically small Stokes shift of ~ 10 meV. The appearance of the J-band is due to the coherent coupled excitonic interaction of many of the aggregated molecules. It is this large oscillator strength and narrow absorption band that allows the observation of strong coupling at room temperature. It is interesting to note that in the natural world, aggregate systems are believed to play a key role in photosynthesis [*Sumi.* (1998)].

In this chapter we present the results of a study on strong coupling between organic aggregate excitons and the photonic mode of a metal-mirrored microcavity. As discussed above, one of the key signatures of strong coupling is an anti-crossing of the exciton and photon modes.   In section 6.2 we describe the fabrication of appropriate samples and indicate how they were characterised.   In section 6.3 we report our measurements demonstrating that strong coupling can be observed in a metal clad microcavity, and that the strong coupling can be observed in both reflection and transmission. In section 6.4 we discuss the results of measurements to look at cavity polariton emission [*Lidzey et al. b* (1999)]. Finally in section 5, we examine possible future directions for the work involving exciton-surface plasmon polariton (SPP) interactions.

6.2 Fabrication and experiment.

Our first requirement was to form a thin stable film of J-aggregates. This was done by dissolving the cyanine dye (2,2'-dimethyl-8-phenyl-5,6,5',6',-dibenzothiacarbocyanine chloride) (see right inset figure 6.1) with the transparent host polymer polyvinylalcohol (PVA) in a 40:60 water:methanol mixture using concentrations of the order of 5×10^{19} molecules/cm^3 and agitating and heating to approximately 90^0C. The solution was spin cast onto a silica substrate (SiO$_2$ n = 1.45) and formed stable, good optical quality films. D. Lidzey of Sheffield and the author made the films. Figure 6.1 shows the room temperature absorption spectrum

obtained from such a PVA matrix film spin cast onto a silica substrate. The microcavities (see left insert of figure 6.1) used in our experiment were fabricated by evaporating a thin silver film (28 ± 5 nm measured by a crystal film thickness monitor) onto a silica substrate. The thickness of the silver films was verified using a Dek-Tak™. The cyanine-dye/PVA mix was then spin cast on top of the metal film, the spin speed being adjusted to produce a film thickness that ensured the cavity polariton modes were close in energy to the organic exciton mode. Six cavities were made in total, and two different concentrations of dye were used. The exact amounts of dye used to form the different concentrations were 49 mg of dye to 3g of PVA and 33 mg of dye again to 3g of PVA. Some 3 cm^3 of solvent were used for each concentration. Film thickness in the range of 175 nm to 202 nm were deposited at a spin speed ~2.5x10^3 rpm, so placing the cavity photon mode approximately 120 meV lower in energy than the exciton mode for normally incident light (in-plane wavevector $k_{//}$ = 0). The microcavity was completed by evaporating a second thin film of silver (28 ± 5 nm) on the top of the organic layer, so forming a low Q cavity (Q ~ 10) of line width ~ 120 meV. For comparison we also fabricated and measured hybrid cavities (D. Lidzey, Sheffield) in which a Bragg mirror replaced the lower metal mirror. The Bragg mirrors (S. Walker, Sheffield) comprised of 9 ¼ wave stacks made from silicon nitride (n=1.95, d=89.7 nm) and silica (n=1.45, d= 120 nm) as high and low index layers respectively.
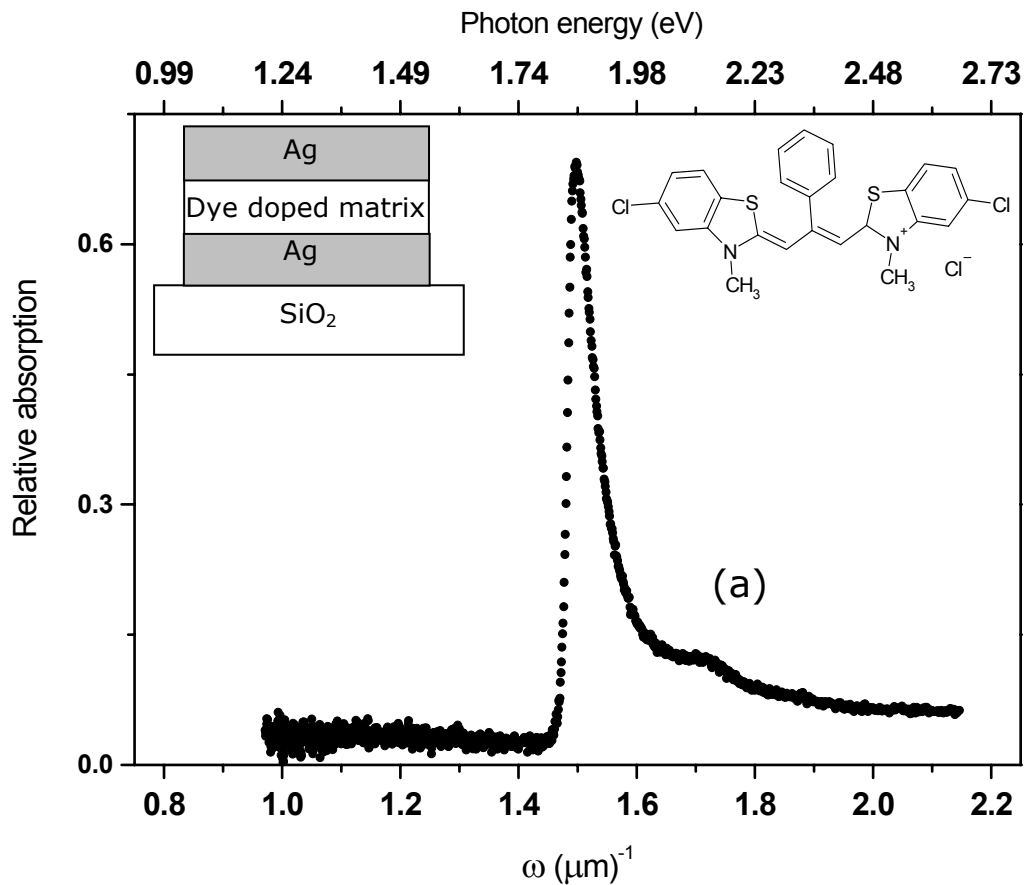
Figure 6.1. The absorption spectrum of a thin film of cyanine dye *J*-aggregates dispersed in a PVA matrix. The inset on the right shows the chemical structure of the cyanine dye studied in this work. (a) indicates a weak shoulder on the absorption and is attributed to oscillatory transitions between coupled monomers. The left inset shows a schematic of the planar microcavity structure.

To characterise the sample we measured its optical transmission [*Salt and Barnes a* (1999)] and reflectivity. When the frequency and in-plane wavevector of the incident light matches that of a microcavity mode, transmission/reflectivity is resonantly enhanced/reduced. Thus by measuring the transmission/reflectivity as a function of frequency and in-plane wavevector, the dispersion of the cavity modes can be determined. The experimental set-up is shown in figure 6.2. Light produced using a 250 W tungsten lamp, was passed through a spectrometer to select the desired wavelength. The sample was mounted on a computer controlled rotation stage

that allowed accurate selection of any incident angle θ, so enabling control of the in-plane wavevector for the selected frequency. Transmission was detected using a photomultiplier tube and a lock-in amplifier. A second detector monitored the incident beam, thus allowing variations in the intensity of the incident light to be accounted for. A polariser allowed selection of either TE or TM radiation for the experiment and a second polariser in front of the main detector eliminated any spurious signals due to polarisation conversion (due to roughness) within the sample.
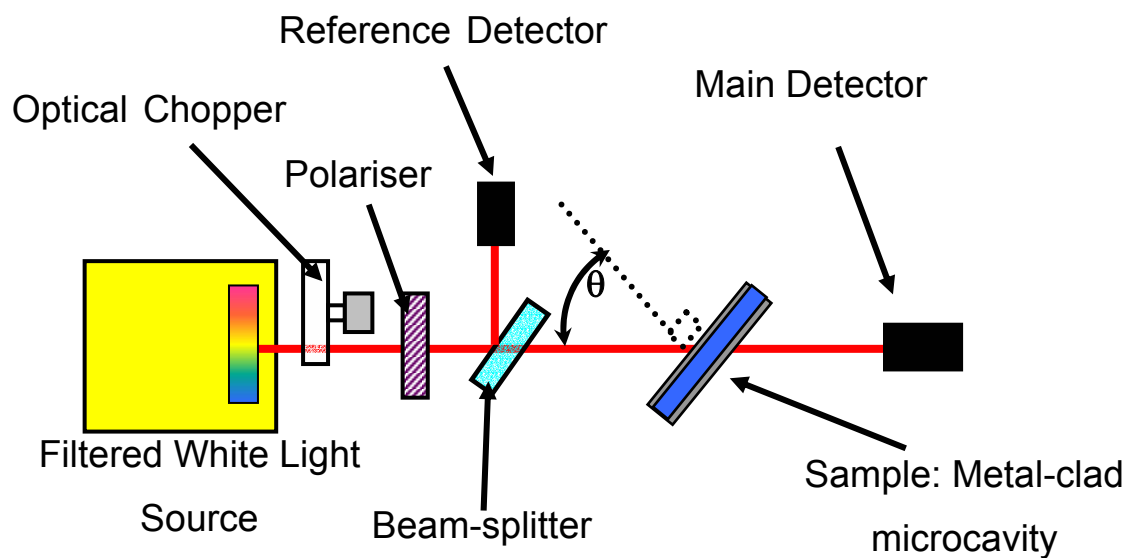
Figure 6.2. Experimental set-up for studying transmission through a metal-metal microcavity. A spectrometer is used to sweep the emission from a white light source whilst the sample is rotated to maintain a constant in-plane momentum for a chosen energy.

Photoluminescence (PL) was measured following non-resonant excitation by a He-Ne laser operating at 594 nm (1.68 μm^{-1}). The PL was detected by a CCD spectrometer system with a spectral resolution of 1 nm. Emission spectra were recorded for a range of emission angles, an optical fibre being used to deliver the laser light to the sample, thus ensuring a constant excitation flux as the sample was rotated. Light exiting the optical fibre was focused down to a ~100 μm diameter spot using a fibre optic collimator.

6.3 Results and analysis

The data acquired from the TE-polarised transmission measurements are shown in figure 6.2. The data are shown as a grey scale map. Since transmission is enhanced when the incident frequency and wavevector match those of a cavity mode, high transmission regions (represented by dark regions in the figure) map out the dispersion of the cavity modes. The data shown in figure 6.3 were taken at room temperature. The data shown correspond to angles of incidence between 0° and 89°. For comparison, measurements of reflectivity from an identical sample are also shown in figure 6.3 (b). The data shown in figures 6.3 (a) and 6.3 (b) indicate that both transmission and reflection may be used to study the metal clad structure since the mode dispersion obtained by the two techniques is very similar. Mode anti-crossing (splitting) is evident for all accessible in-plane wavevector values shown in figure 6.3. At $k_{//} = 0$ $(\mu m)^{-1}$ the photon mode is $\sim$190 meV from resonance with the exciton mode. At $k_{//} \sim 0.75$ $(\mu m)^{-1}$, two nearly equal intensity and approximately equal line-width features are observed. For larger $k_{//}$ the high energy mode gains in strength at the expense of the low energy mode.
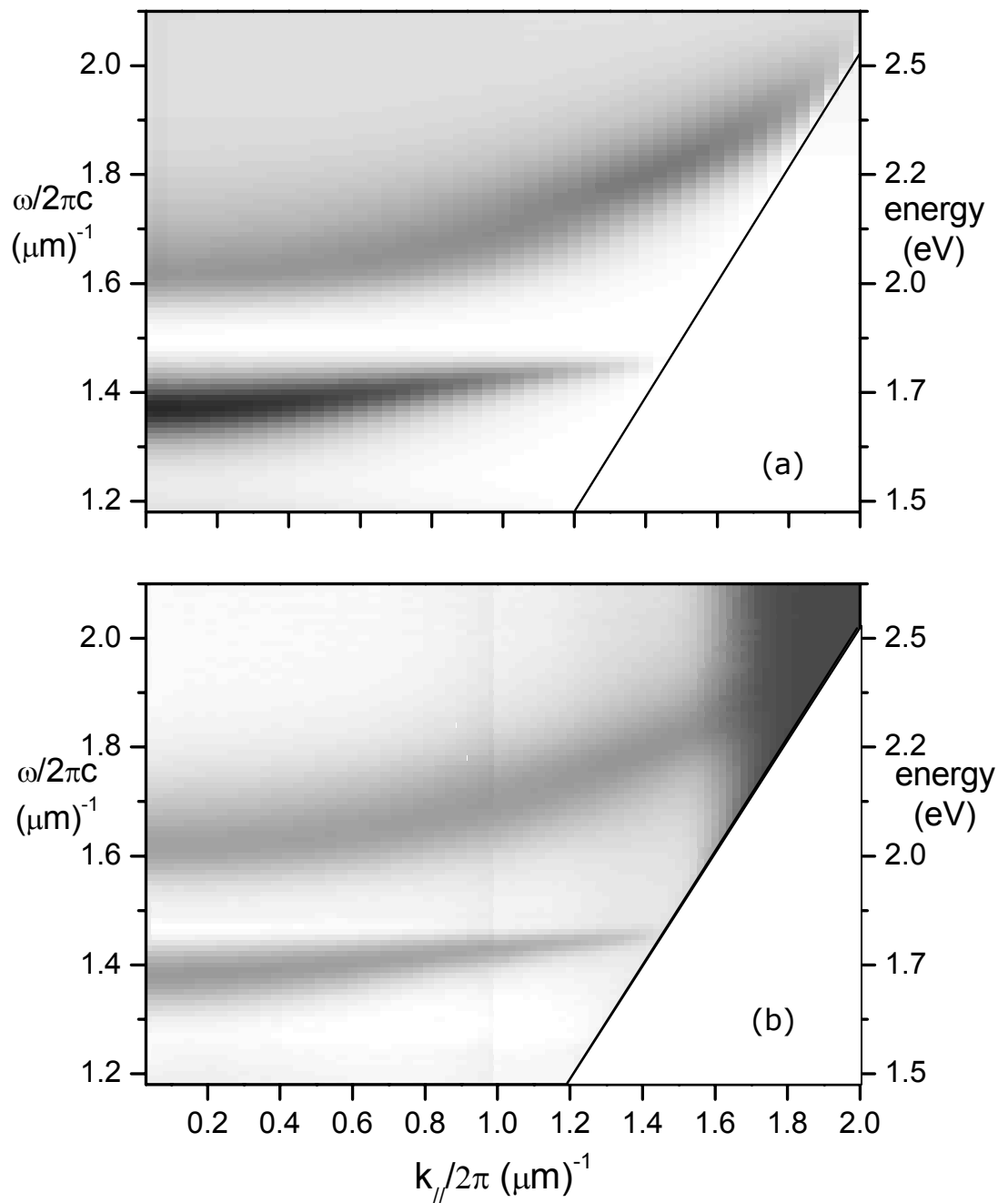
Figure 6.3. a) Transmission across the visible region of the spectrum for TE polarised radiation for the metal-metal cavity. Anti-crossing of the cavity modes and the exciton is very clear. The diagonal line on the right of the plot signifies the maximum accessible scan angle (~90°). b) Reflectivity across the visible region of the spectrum for TE polarised radiation for the same sample as in 3a. Dark regions are areas of low reflection, the dark region beyond $k_{//}=1.6$ (µm)$^{-1}$ is an experimental artefact.

We also measured the PL emission from the sample by recording the emission spectrum as a function of emission angle. As a control we measured the emission from a similar aggregate/PVA film spun directly onto a silica substrate, i.e. no metal mirrors. The PL emission spectra for both the microcavity and bare film were collected for emission angles every 1° from 0° to 90°. Spectra are shown in figure 4a for the bare film and 4b for the microcavity structure. Both data sets are plotted every 5^0 up to 50^0 for clarity. Details of the exact experimental set-up for recording the photoluminescence are given in chapter 5.
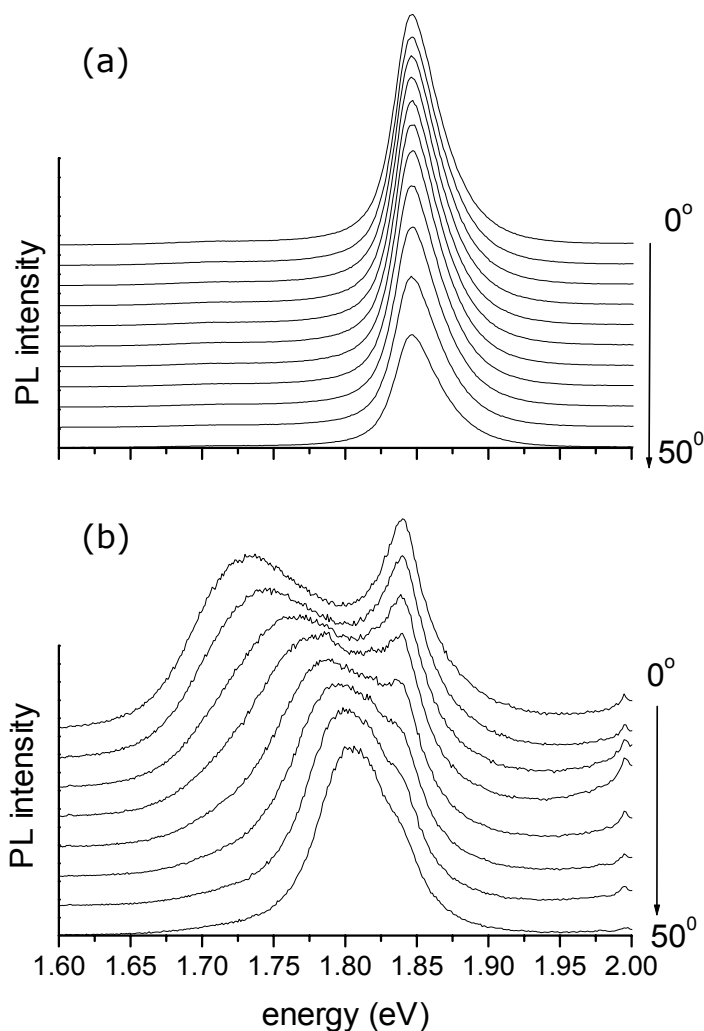
Figure 6.4. Photoluminescence emission spectra recorded for (a) film of cyanine *J*-aggregates deposited on a silica substrate and (b) microcavity containing cyanine *J*-aggregates. The spectra for different angles have been displaced vertically.

For the bare film the emission is as expected from a structure displaying weak coupling, (figure 6.4a) direct emission from the structure occurs at the same energy for all emission angles with only a small Stokes shift from the absorption spectrum. The emission intensity falls with increasing emission angle following the usual Lambertian form. The behaviour of the microcavity sample, shown in figure 6.4b, is markedly different. Two main features are apparent: a strong low energy feature ($\omega = 1.36$ μm^{-1}, photon energy = 1.69 eV) and a higher energy peak ($\omega = 1.49$ μm^{-1}, photon energy = 1.85 eV) corresponding to the direct emission exhibited by the bare film (figure 6.4a). The dispersion of the strong, low energy feature follows the dispersion of the lower polariton branch seen in transmission and reflection, figure 6.3a and figure 6.3b. Note, in agreement with *Lidzey b* (1999), that no emission was seen from the upper branch. This is because the emission comes from an energetically relaxed exciton population, which can only efficiently scatter into the lower branch polariton states). The wavelengths and angles of the photoluminescence peaks are shown superimposed on the reflectivity measurements in figure 6.5 (b).

To analyse the enhancement to Rabi-splitting of the metal microcavity we use a standard model based on the interaction between two oscillators [*Skolnick M. et al.* (1998)]. D. Lidzey of Sheffield performed the theoretical modelling. This approach is commonly used to predict both the energy of the polariton modes as a function of the energetic separation between the exciton and photon modes. The J-aggregate excitons are modelled as oscillators having an absorbance that peaks at $\omega/2\pi c = 1.49$ μm^{-1} (1.85 eV). The dispersion of the cavity mode is calculated using a standard transfer matrix model. The results of our analysis are shown superimposed on the transmission measurements in figure 6.5 (a). It can be seen that the agreement between the predicted dispersion of the polariton modes and the regions of high cavity transmission are very good, giving us confidence that we are observing strong-

coupling. We are thus able to identify both the upper and lower polariton branches as shown. In this particular cavity, we find that the cavity photon is resonant with the exciton mode at approximately $k_{//} = 0$.
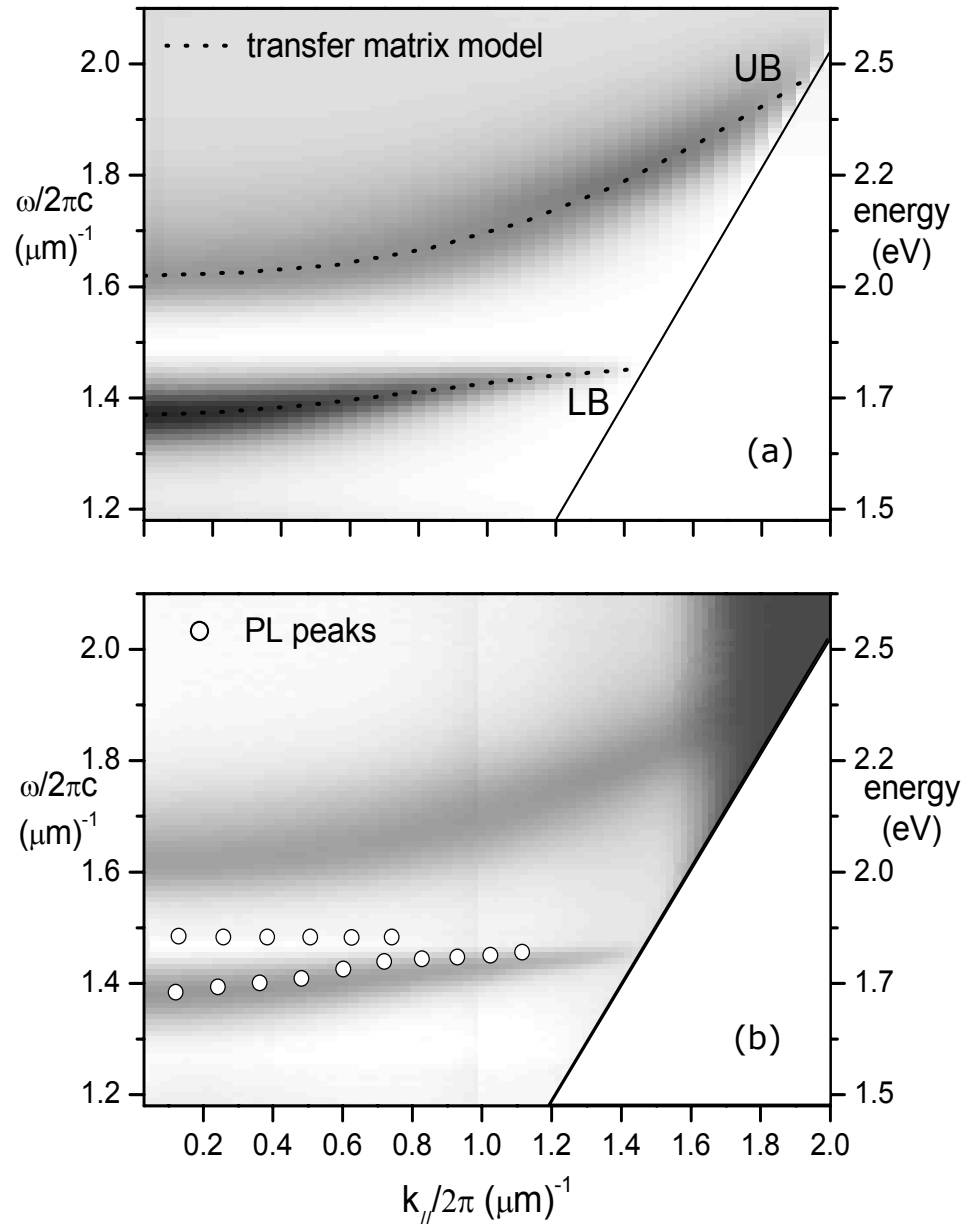
Figure 6.5. a) Transmission across the visible spectrum for TE-polarised light for a metal-metal cavity. Superimposed on the transmission data are the results of the transfer matrix model, allowing identification of upper polariton band (UB) and lower polariton band (LB). b) TE polarised reflectivity for the same structure superimposed with the peaks obtained from PL spectra. These correspond to emission from the lower polariton band and direct emission from aggregated dye molecules not undergoing strong coupling.

From reflectivity and transmission measurements, we determine a Rabi-splitting energy between the polariton branches of 300 meV. This value is significantly larger than previous measurements using the same cyanine dye in a metal-dielectric cavity and to our knowledge is the largest Rabi-splitting ever measured in a microcavity.

To further investigate the enhancement to the splitting in metal-metal microcavities, we fabricated a number of all-metal cavities and hybrid metal-DBR cavities in which the optical concentration of the aggregate and hence the oscillator strength was varied. For each cavity we also determined the Rabi-splitting from transmission and reflectivity data. Also, for each cavity, an identical control (non-cavity) film of J-aggregates in PVA was fabricated. We determined the relative oscillator strength of each control film from measurements of absolute optical transmission. From this measurement we calculated a dielectric function for the control films, which was then used in a transfer matrix model to yield the oscillator strength of each control film (in units of cm^{-2}).

The results plotted against the square root of the oscillator strength are shown in figure 6.6. We note two interesting facts. Firstly, the Rabi-splitting measured in a cavity is proportional to the square root of the oscillator strength of the material placed within the cavity as expected from Eq. 3.15. Secondly, the giant Rabi-splitting measured in the all-metal cavities is enhanced by a factor of ~ 2.3+/-0.3.
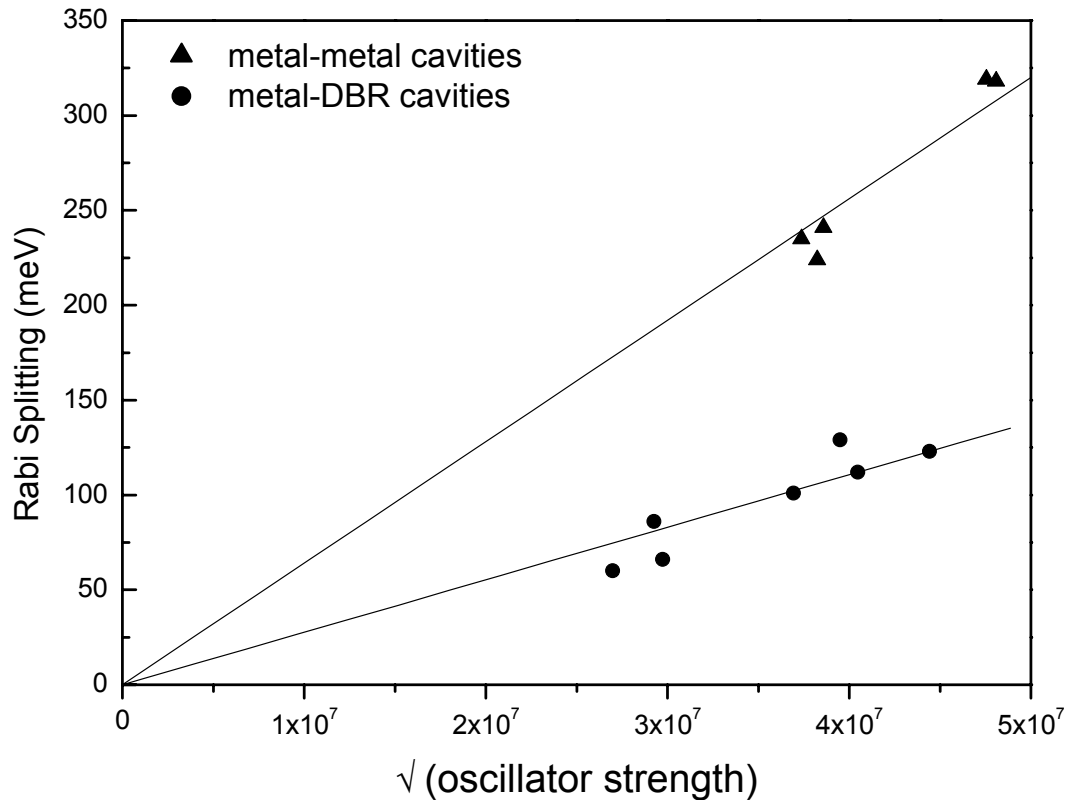
Figure 6.6. Measured Rabi-splitting for all metal [triangle] and hybrid metal-DBR [circle] microcavities as a function of relative Oscillator strength. The lines are to guide the eye only.

We can explain this large increase in splitting on the basis of the reduced optical path-length of the metal-metal cavity compared to the metal-dielectric mirror cavity. The optical field within a cavity defined using dielectric mirrors penetrates a significant distance into each dielectric mirror [*Skolnick et al.* (1998)]. In the metal-dielectric mirror cavity, we calculate that the optical field penetrates approximately 0.87λ into the dielectric mirror. This penetration increases the effective cavity length (L_{eff}), and it has been shown in chapter 2 that the Rabi-splitting is proportional to $L_{eff}^{-1/2}$. We calculate that the effective optical path-length of the metal-dielectric cavity is approximately 2.7 times longer than the metal-metal cavity, which implies that the Rabi-splitting in the metal-metal cavity should be enhanced by a factor of approximately 1.7 times. A full transfer matrix simulation yields a very similar result. This factor is in

reasonable agreement with the measured enhancement in the splitting of approximately 2.3. We therefore explain the enhanced splitting by better confinement of the optical field in the all-metal cavity as the penetration of the optical field into a silver mirror is very small (~ 10 nm for light of λ = 670 nm). This significantly shortens the effective cavity length of the metal-metal cavity, which enhances the optical field that interacts with the J-aggregates. The enhancement of the optical field is thus reflected by an increase in the Rabi-splitting. Indeed, if the splitting were not enhanced in the metal-metal cavity, then it might be difficult to reach the strong-coupling regime. This is because the low Q of the metal-metal cavity results in a cavity-photon mode having a relatively broad linewidth (~120 meV), which is larger than the typical splittings of 80 to 100 meV observed in the metal-dielectric mirror cavity.

6.4 **Summary**

We have reported the first experimental observation of strong exciton-photon coupling in low-Q planar microcavities composed of an organic semiconductor positioned between two metallic, silver mirrors. The use of metal mirrors allows investigation of the cavity polaritons out to high in-plane wavevectors using transmission measurements. Using transmission and reflectivity measurements, we observed a very large, room temperature Rabi splitting in excess of 300 meV between upper and lower cavity polariton branches. We have shown that the Rabi-splitting is enhanced in all-metal microcavities by a factor of more than 2 times compared to microcavities composed of an organic film having the same oscillator strength positioned between a silver mirror and a dielectric mirror.

This enhancement results from the significantly larger optical fields that are confined within all-metal microcavities. Our results offer an alternative strategy in the exploration of coherent phenomena in organic based, strongly coupled systems. Furthermore

it is a strategy that can also be implemented using simple fabrication techniques.

6.5 Future Work: Strong exciton–SPP coupling

So far we have looked exclusively at the interaction between cavity photons and the exciton. A logical extension of this work would be to examine the possibility of strong coupling between the surface plasmon mode and the cavity polariton. During the course of this work a brief initial study of such an interaction was undertaken with promising initial findings as presented below.

The physical origin and dispersion of the surface plasmon polariton (SPP) has been thoroughly discussed in chapter 2. To recap the SPP arises due to the interaction of electromagnetic radiation (TM polarisation) with the free charges that exist in a metal. The SPP mode propagates at the interface of a metal and dielectric.

Previous workers [*Pockrand et al.* (1979), *Philpot and Swalen* (1978)] have looked at weak exciton-surface plasmon interactions. *Pockrand et al.* (1979) investigated the optical properties of monolayers of organic dye molecules deposited on metal films by the Langmuir-Blodgett technique using attenuated total reflection (ATR) spectroscopy [*Raether* (1988) and chapter 2]. They found that SPP waves excited at the metal interface interacted with the monolayers of dye. This resulted in a perturbation of the SPP dispersion curve with small wiggles or 'back-bending' becoming apparent. Due to the fairly weak oscillator strength of the dyes used in the experiments the observed effects were small and took place over a very small angular range. The resulting back bending of the dispersion was a weak example of the perturbation of the mode associated with normal mode coupling in cavities.

In our experiment, a thin stable film of J-aggregate was spin deposited on a silver grating. The grating was formed in photoresist by the standard holographic procedures explained in chapter 4.

Briefly, photoresist was spin deposited onto a silica substrate and exposed to UV radiation in an interference pattern. Upon development, a periodic diffraction grating is left in the photoresist. After a brief period of post developing baking a stable photoresist grating is formed. Upon this an optically thick (600 nm layer of silver) was thermally deposited.

As described in chapter 2, the grating allows Bragg scattering of the bound SPP mode so as to be enable it to couple to radiation (see chapter 5). For such a mechanism the grating pitch is the most critical parameter with film thickness second. The objective is to scatter the SPP mode back inside the light line and for the dye absorption and unperturbed SPP modes to cross at a convenient angle. For the experimental set up used in our reflectivity measurements this was between 10 and 50 degrees. A sub-wavelength pitch of approximately 280 nm was used.

Using the surface plasmon dispersion equation introduced in 2.12.

$$k_{SPP} = k_0 \sqrt{\frac{\varepsilon'_m \varepsilon_d}{\varepsilon'_m + \varepsilon_d}} \qquad (6.1)$$

and substituting in values for the real part of the silver permittivity ε'_m and the PVA permittivity ε_d we estimate

$$k_{SPP} \approx 1.8 k_0 \qquad (6.2)$$

which if we substitute into the Bragg scattering equation 2.50 we find

$$1.8 = n \sin\theta \pm \frac{\lambda_0}{\lambda_g} \qquad (6.3)$$

For experimental reasons it was convenient for the SPP to interact with the exciton at 30^0, so that we calculate a grating pitch λ_g in the region of 300 nm.

A 280 nm pitch grating was fabricated and a 200 nm film of dye was spin cast on to it. Reflectivity measurements were recorded and are shown in figure 6.7.
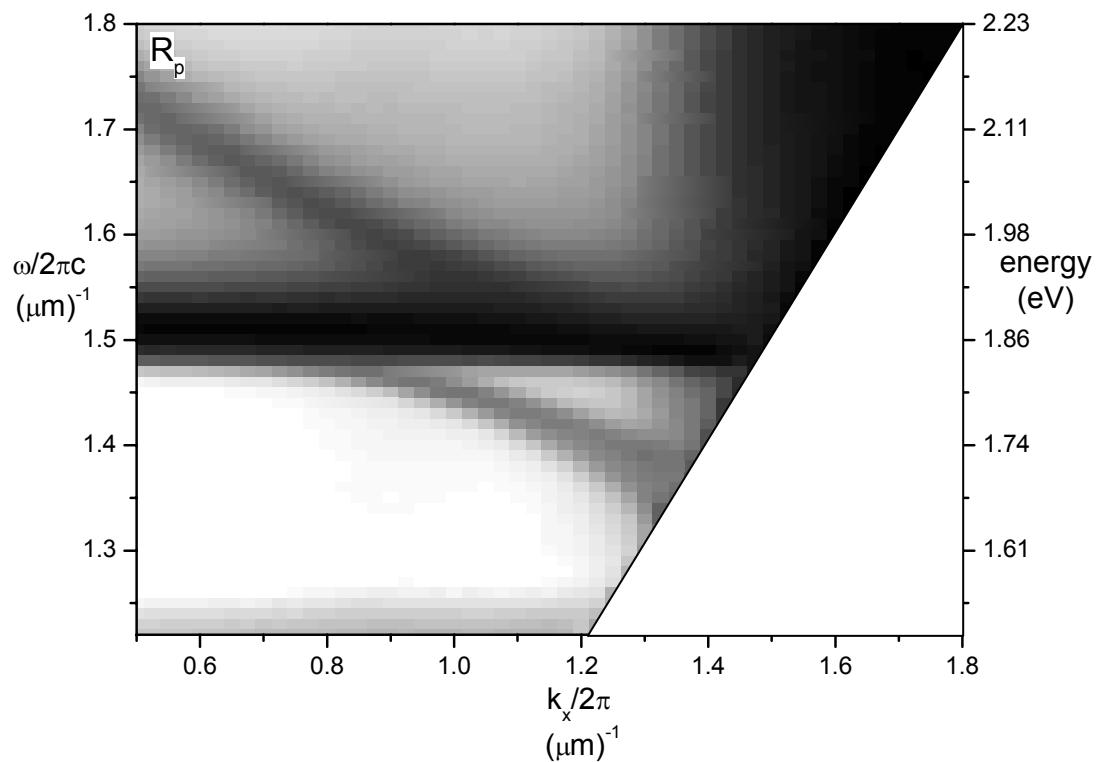
Figure 6.7. TM-polarisation reflectivity scan showing a back scattered SPP mode strongly interacting with the J-aggregate absorption. Due to both features being reflectivity minima it is not possible to distinguish between the J-aggregate absorption and the distortion of the SPP. Consequently, the SPP mode splitting is obscured.

The reflectivity measurements do demonstrate a large SPP-exciton interaction, which to our knowledge is largest measured in any comparable system. However unlike the transmission in the cavity experiment there is no contrast between the SPP mode and the J-aggregate absorption; both modes appear as black features. This means it is impossible to confirm if the mode is actually split into upper and lower polariton bands or is merely a rather extreme case of the 'back-bending' previously observed by *Pockrand et al.* (1978).

Chapter 7

Conclusions

7.1 Introduction

In this thesis optical microcavity structures were used to conduct experiments on the interaction of light with organic photonic materials. The interaction falls within two regimes known as weak and strong coupling. In weak coupling an excited species emits into the photonic modes of a device when it decays. The presence of the emitter does not alter the photonic modes of the structure. In contrast, the signature of strong coupling is an anti-crossing of the exciton and photon modes resulting in new, hybrid excitonic-photonic modes. Both interactions were experimentally investigated in chapters 5 and 6 of this thesis.

7.2 Surface plasmon emission from OLEDs

Organic light emitting diodes (OLEDs) take the form of an optical microcavity containing relatively high index layers of organic semiconductor and dielectrics. Generally one layer of the device is a metallic cathode. OLED operation is an archetypal weak coupling phenomenon the result of which is that much of the emitted radiation will become trapped by the photonic modes of the structure.

The work in chapter 5, reported on the first experimental demonstration of an OLED device that couples out light that would otherwise be lost to the surface plasmon polariton (SPP) mode as well as other guided modes. Also observed were enhancements to device emission and polarisation changes and spectral changes in the emission spectra. We estimated that only ~ 8 % of the light escapes into the air from conventional small molecule based planar devices, this is partly due to strong coupling to the SPP. From studying

emission spectra of our corrugated device as a function of emission angle we estimate that ~ 50 % of the power radiated by this device is due to surface plasmon mediated emission. This implies an increase in out-coupling efficiency from 8% to 16%.

7.21 Future work on OLEDs

Further increases to the power recovered from SPP modes could be accomplished by optimising the surface profile of the corrugation and using 2-dimensional periodic pattering. Other work [*Worthing and Barnes* (2001)] suggests that 50 – 60 % of the power that would usually be lost to SPP modes may be recouped. Although not all of this power will necessarily be radiated into useful directions, it is clear that this is a potential route for further increasing the efficiency of OLEDs.

Another issue for future enquiry is whether SPP modes might be extracted through the metallic cathode rather than being scattered out through the anode and substrate. There has already been some work on transmission through perforated metal films [*Ebbesen et al.* (1999)]. An important question is whether the cathode must contain holes, or whether an appropriately textured continuous metal film suffice? Initial studies by *Gifford and Hall* (2002) on cross-coupling of surface plasmons through textured continuous films suggest that extracting energy through films using surface plasmons may be a viable option. This research is motivated in part by the desire to integrate OLEDs onto opaque substrates such as silicon.

7.3 Strong coupling

In chapter 6 we presented the results of a study on strong coupling between organic aggregate excitons and a waveguide mode

in a metal-mirrored microcavity. As stated in chapter 6, the key signature of strong coupling is an anti-crossing of the exciton and photon modes. The anti-crossing manifests itself as two features in the reflectivity and transmission of the microcavity. Our measurements demonstrate the first observation of strong coupling in a metal clad microcavity.

We demonstrated that microcavities with all-metal mirrors may be successfully used to explore strong coupling phenomena, despite the absorption exhibited by the metals and the associated low Q of such cavities. Indeed, the strength of the splitting is the largest ever measured in a microcavity (> 300 meV) and is due to the large oscillator strength of the organic film, and the strong field enhancement in metallic microcavities. Rabi-splitting is enhanced in all-metal microcavities by a factor of more than 2 times compared to microcavities composed of an organic film having the same oscillator strength positioned between a silver mirror and a dielectric mirror. Our structures offer an alternative strategy in the exploration of such coherent phenomena in organic based, strongly coupled systems, one that can be implemented with simple fabrication techniques.

7.31 Future work on strong coupling

Strong coupling arises due the interaction between excitons and the photonic mode of a cavity. In chapter 5 we speculated that a similar interaction might arise between the SPP mode propagating on a metallic grating and organic aggregate excitons.

A preliminary experiment was conducted, and reflectivity measurements were taken from a silver grating coated with a film of J-aggregate dispersed in a PVA polymer matrix. Although a large interaction was observed (to our knowledge the largest ever seen in such a system), we were unable to conclude whether the SPP mode was actually split into distinct upper and lower polariton branches or

just bending back on its self as it passed through the J-aggregate absorption. This is because both the J-aggregate absorption and the SPP are observed as reflectivity minima in the data. Further experiments, possibly conducted on optically thin metal gratings to allow transmission measurements, may reveal the exact nature of the interaction.

Publications and presentations

"Birefringence and dispersion of the light emitting polymer MEH-PPV".
A. Boudrioua, P.A. Hobson, B. Matterson, I.D.W. Samuel and W.L. Barnes.
Synth. Met. **111-112**, 545-547 (2000)

"Identification and recovery of the trapped guided modes in LED structures using nanoscale texturing."
P.A. Hobson, J. A. E. Wasey. I. Sage and W.L. Barnes.
Organic Photonic materials and Devices IV. SPIE proceedings, **4642,** 102. (2002).

"The role of surface plasmons in organic light-emitting diodes."
P.A. Hobson, J.A.E. Wasey, I. Sage and W.L. Barnes.
IEEE Journal of Selected Topics in Quantum Electronics, **8** (2): 378-386 (2002).

"Strong exciton-photon coupling in a low-Q all-metal mirror microcavity."
P.A. Hobson, W.L. Barnes, D.G. Lidzey, G.A. Gehring, D.M. Whittaker, M.S. Skolnick.
Accepted by Appl. Phys. Lett.

"Surface Plasmon Mediated Emission from Organic Light Emitting Diodes."
P.A. Hobson, S. Wedge, J.A.E. Wasey, I. Sage and W.L. Barnes
Accepted by Adv. Mat.

"Optical properties of the light emitting polymer MEH-PPV"

A. Boudrioua, P.A. Hobson, J.A.E. Wasey, W.L. Barnes, B.J. Matterson and I.D.W. Samuel.

poster at **ICEL2**, Sheffield, U.K., May 1999.

"Strong coupling in an organic metal-clad microcavity"

P.A. Hobson, M.G. Salt, W.L. Barnes, D. G. Lidzey, D.D.C. Bradley, and M.S. Skolnick.

talk at **QELS 2000**, San Francisco, U.S.A., May 2000

"Identification and Recovery of the Trapped Guided Modes in LED Structures using Nanoscale texturing."

P.A. Hobson, J.A.E. Wasey, I. Sage and W.L. Barnes.

poster at **ICEL3**, Los Angeles, U.S.A., Sept 2001

"Identification and Recovery of the Trapped Guided Modes in LED Structures using Nanoscale texturing."

P.A. Hobson, J.A.E. Wasey, I. Sage and W.L. Barnes.

talk at **Photonics West**, San Jose, U.S.A., Jan 2002

References

| Andrew P (a). | (1998) | PhD. Thesis University of Exeter (unpublished) |

Andrew P (a).   (1998)   PhD. Thesis University of Exeter (unpublished)

Andrew P (b), Turnbull GA, Samuel IDW and Barnes WL.   (2002)   In press App. Phys Lett.,

Aziz H, Popovic ZD, Tripp P, Hu N, Hor, and Xu G.   (1998)   Appl. Phys Lett. **72**, 2642

Barnes WL.   (1998)   J. Mod. Opt. **45**, 661-699

Benisty H. De Neve H and Weisbuch C.   (1998)   IEEE J. Quant. Elec., **34**. 1632

Burroughes JH, Bradley DDC, Brown AR, Marks RN, Mackay K, Friend RH, Burns PL and Holmes AB.   (1990)   Nature. **347**, 539

Carmichael HJ, Brecha RJ, Raizen MG, Kimble HJ and Rice PR.   (1989)   Phy. Rev. A. **40**, 5516

Chance RR, Prock A and Silbey R.   (1978)   Adv. Chem. Phys, **37**. 1

Chandezon J, Dupuis MT, Cornet G and Maystre D.   (1982)   J. Opt. Soc. Am. **72**, 839.

Charlton, MDB and Roberts SW.   (2000)   Physics World

Comiskey B, Albert JD, Yoshizawa H and Jacobson J.   (1998)   Nature 394, 253 - 255

Dodabalapur A. Rothberg LJ, Jordan RH, Miller TM, Slusher RE and Phillips JM.	(1996)	J. Appl. Phys. **80**, 6954
Drexhage KH.	(1974)	Prog. Opt. **12**, 165
Ebbesen T. Lezec, H. Ghaemi H. Thio T and Wolff P.	(1998)	Nature, **391**. 667
Fano U.	(1941)	J. Opt. Soc. Am. **31**, 213.
Farchioni R and Grosso G. (Eds.)	(2001)	Organic Electronic Materials.
Fermi E.	(1932)	Rev. Mod. Phys., **4**, 87
Ford G. and Weber W.	(1984)	Phys. Rep. **113**.
Friend RH, Gymer RW, Holmes AB, Burroughes JH, Marks RN, Taliani C, Bradley DDC, Dos Santos DA, Brédas JL, Lögdlund M and Salaneck WR.	(1999)	Nature. **397**. 121
Gifford DK and Hall DG	(2002)	Appl. Phys. Lett. **80**, 3679-3681
Greenham NC, Friend RH and Bradley DDC	(1994)	Adv. Mater. **6**. 491
Gruhlke RW and Hall DG.	(1989)	Phys. Rev. B., **40**. 5367.
Gruhlke RW, Holland WR and Hall DG.	(1986)	Phys. Rev. Lett. **56**. 2838,
Harris JB.	(1996)	
Helfrich W and Schneider WG	(1965)	Phys. Rev. Lett. **14**, 229
Hobson PA (a), Wasey JAE, Sage I and Barnes WL.	(2002)	IEEE JSTQE, **8**, 378

Hobson PA (b). Wedge S. Wasey JAE, Sage I and Barnes WL.   (2002)   Accepted by J. Adv Mat

Houndré R, Weisbuch C, Stanley RP, Oesterle U, Pellandini Pand Ilegems M.   (1994)   Superlattices and microstructures. **15**, 263

Hung LS, Tang CW, Mason MG, Raychaudhuri P and Madathil J.   (2001)   App. Phys. Lett., **78**. 544

Hunt NEJ, Schubert EF, Logan RA and Zydzik GJ,   (1992)   Appl. Phys. Lett. **61**, 2287

Hutley MC   (1982)   Diffraction gratings (Academic Press, London)

Jabbour GE, Kawabe Y, Shaheen SE, Wang JF, Morrell MM, Kippelen B and Peyghambarain N.   (1997)   Appl. Phys. Lett. **71**, 1762

Jelley EE.   (1936)   Nature. **138,** 1009

Jory MJ, Bradberry GW, Cann PS and Sambles JR.   (1996)   Sensors and actuators B-Chemical **35**, 197-201

Kaminow IP, Mammel WL, and Weber HP.   (1974)   Appl. Opt. **13**, 396.

Kato T, Mori T and Mizutani T.   (2001)   Thin solid films. **393**. 109

Khitrova G, Gibbs HM, Jahnke F, Kira M and Koch S. W,   (1999)   Rev. Mod. Phys. **71**, 1591

Kittel C.   (1996)   Introduction to Solid state physics 7th Ed. Wiley

Kleppner D.   (1981)   Phys. Rev. Lett. **47**, 233

Knight JC. and Russell P. St. J.   (2002)   Science, **296,** 276-277

Kobayashi T. (editor)	(1996)	J Aggregates, (World Scientific, Singapore)
Kolosov D, English DS, Bulovic V, Barbara PF, Forrest SR, and Thompson ME,	(2001)	J. Appl. Phys. **90**, 3242.
Kretschmann E. and Raether H.	(1968)	Z. Naturf. A **23**, 2135
Lidzey DG (a), Bradley DDC, Skolnick MS, Virgili T, Walker S and Whittaker DM.	(1998)	Nature **395**, 53
Lidzey DG (b), Bradley DDC, Virgili T, Armitage A, Skolnick MS, and Walker S.	(1999)	Phys. Rev. Lett. **82,** 3316-3319.
Lidzey DG (c), Bradley DDC, Armitage A, Walker S, and	(2000)	Science **288,** 1620-1623
Liew Y, Aziz H, Hu N, Chan HS, Xu G, and Popovic Z.	(2000)	Appl. Phys. Lett.**77**, 2650
Lupton JM, Matterson BJ, Samuel IDW, Jory MJ and Barnes WL.	(2000)	App. Phys. Lett. **77**. 3340
Mitschke U and Bäuerle P.	(2000)	J. Mater. Chem. **10**, 1471-1507.
Moll M, Mahrt RF, Bauer C, Giessen H, Schnabel B, Kley EB and Scherf U.	(2002)	App. Phys. Lett. **81**, 734.
Nelson TR, Prineas JP, Khitrova G, Gibbs HM, Berger JD, Lindmark EK, Shin JH, Shin HE, Lee YH, Tayebati P and Javniskis L.	(1996)	Appl. Phys. Lett. **69**, 3031

Nylander C, Liedberg B. and Lind T.	(1982)	Sensors and Actuators **3**. 79.
Otto A.	(1968)	Z. Phys. **216**, 398.
Owyang GH,	(1981)	Foundations of Optical Waveguides (Edward Arnold, London)
Pain HJ.	(1993)	The Physics of Vibrations and Waves 4th Ed. Wiley
Parker G and Charlton M.	(2000)	Physics World
Paul KE, Breen TL, Aizenberg J, and Whitesides GM.	(1998)	App. Phys. Lett. **73**, 2893
Pedrotti FL, and Pedrotti LS,	(1993)	Introduction to Optics 2nd Ed. (Prentice Hall International editions)
Philpot MR and Swalen JD	(1978)	J. Chem. Phys. **69**, 2912.
Pockrand I, Swalen JD, Gordon II JD and Philpott MR.	(1979)	J. Chem. Phys. **70**, 3401.
Pockrand I.	(1974)	Phys. Lett. **49a**, 249.
Popovic ZD. and Aziz H.	(2002)	IEEE JSTQE. **8**, 1077
Priest TW, Cotter NPK and Sambles JR	(1995)	J. Opt. Soc. Am. A **12**, 1740.
Purcell EM.	(1946)	Phys. Rev., **69**, 681
Raether H.	(1988)	Surface Plasmons (Springer-Verlag, Berlin)
Rajagopal A, Wu CI and Kahn A.	(1998)	J. Appl. Phys. **83**, 2649

Rarity J. and Weisbuch C. (Ed's)	(1995)	Microcavities and photonic band gaps: Physics and applications, NATO ASI series E. **324**.
Rayleigh	(1907)	Phil. Mag. **14**, 213.
Salt MG (a) and Barnes WL	(1999)	Opt. Comm. **166,** 151.
Salt MG (b), Tan WC and Barnes WL.	(2000)	Appl. Phys. Lett. **77,** 193-195
Sarid D.	(1981)	Phys. Rev. Lett. **47**, 1927
Savvidis PG, Baumberg JJ, Stevenson RM, Skolnick MS, Whittaker DM, Roberts JS,	(2000)	Phys. Rev. Lett. **84**. 1547
Schubert EF, Wang YH, Cho AY, Tu LW and Zydzik GJ.	(1992)	Appl. Phys. Lett. **60**, 921
Skolnick MS, Fisher TA and Whittaker DM.	(1998)	Semicond. Sci Technol. **13**, 645
Sommerfield A.	(1949)	Partial Differential equations. (New York: Academic Press)
Sumi H,	(1998)	J. Phys. Chem. B. **103**. 252
Tang CW and VanSlyke SA.	(1987)	App. Phys. Lett. **51**. 913
Tang CW. VanSlyke SA and Chen CH.	(1989)	J. App. Phys. **65**. 3610.
Tsutsui T, Yahiro M, Yokogawa H, Kawano K and Yokoyama M.	(2001)	Adv. Mat., **15**. 1149.
Turnbull GA, Andrew P, Jory MJ, Barnes WL and Samuel IDW.	(2001)	Phys. Rev. B. **64**, 125122-1

Van Slyke SA, Chen CH and Tang CW.	(1996)	Appl. Phys. Lett. **69**, 2160
Wasey J and Barnes WL.	(2000)	J. Mod. Opt,. **47**. 725.
Weisbuch C, Nishioka M, Ishikawa A, and Arakawa Y.	(1992)	Phys. Rev. Lett. **69,** 3314-3317
Welford and Sambles	(1988)	J. Mod. Opt. **35** 1467
Windisch R, Heremans P, Knobloch A, Dohler KPGH, Dutta B and Borghs G.	(1999)	App. Phys. Lett,. **74**. 2256
Wood RW.	(1902)	Phil. Mag. **4**, 396.
Worthing PT and Barnes WL	(2001)	Appl. Phys. Lett. **79**, 3035-3037
Yablonovitch E. and Gmitter T.	(1989)	J. Phys. Rev. Lett., **63**. 1950
Yamamoto Y, Machida S and Björk G,	(1991)	Phys. Rev. A. **44**, 657
Zhu Y, Gauthier DJ, Morin SE, Wu Q, Carmichael HJ and Mossberg TW.	(1990)	Phys. Rev. Lett. **64**, 2499

Appendix A

The numerical modelling in chapter 5 is based on data concerning the optical properties of the materials used [*Hobson (a)* 2002]. Included here is relevant information not contained in chapter 5. Figure A1 shows the intrinsic emission spectrum of Alq_3 used to calculate the effect the spread of emission wavelengths on the coupling to the SPP modes.
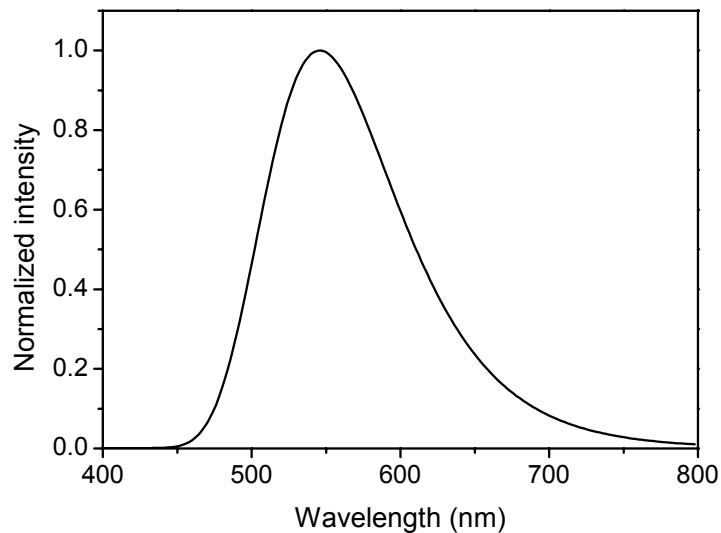
Figure A1. Intrinsic emission spectra of Alq_3 and used in the calculations presented in chapter 5. The spectrum was measured using photoluminescence normal to a thin (<50 nm) film on a planar silica substrate [Hobson (a) et al. (2002)].

Silica substrates were assumed to be dispersionless with a permittivity $\varepsilon = 2.12$. For other materials the effects of dispersion required the use of polynomials to represent the dielectric constants.

1) Alq_3:

$$n_{alq} = -1.33075 + 8069156x - 8.42617x^2 + 3.38293x^3 - 0.48725x^4 \tag{A.1}$$

here $x =$ wavelength (nm)/400

2) Aluminium:

$$n = 19.92812 - 84.7052x + 140.1731x^2 - 111.85238x^3$$
$$+ 43.467x^4 - 6.53696x^5$$

(A.2)

and

$$k = 319.47025 - 1347.04872x + 2350.75746x^2 - 2149.03408x^3$$
$$+ 1088.8157x^4 - 289.65148x^5 + 31.56516x^6$$

here $x = $ wavelength (nm)/400

3) ITO:

$$n_{ITO} = 1.67567 + 0.20122x$$

(A.3)

and

$$k = 0.005$$

here $x = $ 1000/wavelength (nm)